QUANTUM NOISE REDUCTION FOR GRAVITATIONAL WAVE DETECTORS: DEVELOPING REALISTIC INTERFEROMETER SCHEMES

by

Mengyao Wang

A thesis submitted to the

University of Birmingham

for the degree of

Doctor of Philosophy

Astrophysics and Space Research Group

School of Physics & Astronomy

College of Engineering and Physical Sciences

University of Birmingham

September 2013

Acknowledgements

I am deeply grateful to my supervisor Andreas Freise. He led me into the gravitational wave community and suggested this interesting project to me. I greatly appreciate his guidance into the unknown, his unfailing encouragement and sustained support without which it would not have been possible for me to complete this work. I would like to thank Andreas for sending me to the California Institute of Technology, introducing me the topic of quantum noise and opening a new chapter in my life.

The Birmingham Gravitational Wave group is amazing and I am so glad to be a part of it. I enjoyed lots of wonderful team work with my colleagues Charlotte Bond, Daniel Brown, Frank Brückner, Ludovico Carbone, Deepali Lodhia and Rebecca Palmer. Discussions with them were always insightful and lit me up. I am greatly thankful to Charlotte for her patient guidance in mirror map simulations using MATLAB and FINESSE. I must express my sincere gratitude to Frank for his help with writing this thesis — English, grammar, writing style, and lots more. A special mention also goes to Dee for proofreading this thesis.

I would like to thank Keiko Kokeyama and Paul Fulda for guidance and help in the lab. I express my thanks to the technical staff: David Hoyland and John Bryant, for their help in electronics throughout my experiment.

My sincere gratitude to Yanbei Chen for inviting me to Caltech, providing an excellent opportunity to learn the quantum noise theory. A special thanks to Haixing, who made the learning of 'obscure theory' lots of fun; thank you for the continuous encouragement and supporting me in so many ways.

I also extend my thanks to my very good friends Weixin Song, Hongting Zhao,

and Kan Hu for making me not feel that far away from home, and also Lu Shi, Ying Li, Shan Wang, and Murong Xu for listening to my troubles and relieving the pressure. A big thank you to Haobo Fu and Dongshen He for their company during my writing.

Above all, I owe a huge thanks to my parents and brother for their everlasting support over the years.

This thesis is dedicated to the memory of my maternal grandfather!

Statement of Originality

This thesis includes my research work carried out at the University of Birmingham between September 2009 and September 2013.

The comprehensive analysis of different intra-cavity filtering schemes presented in Chapter 3 can also be found in
M. Wang, H. Miao, A. Freise, and Y. Chen, *Sensitivity of intra-cavity filtering schemes for detecting gravitational waves*, Phy. Rev. D (2013) (to be published) [1]

The major results of an alternative GW detector topology, a polarising Sagnac interferometer with practical DC readout realisation, for the Einstein Telescope low frequency interferometers presented in Chapter 4 have been published in
M. Wang, C. Bond, D. Brown, F. Brückner, L. Carbone, R. Palmer and A. Freise, *Realistic polarising Saganc topology with DC readout for the Einstein Telescope*, Phys. Rev. D **87**, 096008 (2013) [2]

Abstract

Gravitational waves are a predication of Einstein's theory of general relativity. After nearly 50 years of effort by the scientific community to construct a detector capable of directly measuring gravitational waves, we expect a breakthrough, the first ever direct measurement of a gravitational wave within the next 5 years. The Advanced LIGO detectors currently under construction are predicted to achieve not only the first detection but to open the field of gravitational-wave astronomy: as an observational window on astrophysics and with an impart on other areas such as cosmology, strong-field gravity, general relativity, and nuclear physics.

The Advanced LIGO detectors are large-scale laser interferometers that have been designed for very low technical noise so that quantum noise will be limiting their sensitivity over a wide range of their spectrum. Planning for future gravitational wave observatories is already underway and reducing the fundamental quantum noise is considered to be one of the main experimental challenges. My work over the last 4 years has focused on possible new techniques to reduce or circumvent the quantum noise in laser interferometers. I have pursued three independent approaches: at first I present alternative filtering schemes as possible upgrades for advanced detectors, I further present a new interferometer design based on a Sagnac interferometer for future gravitational wave observatories, and at last I discuss the design and preliminary results of an experiment to investigate optical losses in cavities to support the technical design of quantum noise reduction schemes.

In the gravitational wave community, quantum noise is commonly divided into two categories, radiation pressure noise and shot noise. In order to reduce the radiation pressure noise for advanced gravitational wave detectors, different strategies have been proposed; some schemes including the use of optical filter cavities

are promising and an upgrade of Advanced LIGO using input-cavity filtering is a possible intermediate goal. However, the details of the implementation of filtering schemes for advanced gravitational wave detectors are still under discussion. In this thesis I present two practical intra-cavity filtering configurations, aimed at reducing radiation pressure noise. I investigate the feasibility of implementing intra-cavity filtering for advanced gravitational wave detectors and show that it has a similarly low quantum noise behaviour as the input cavity filtering.

Future gravitational wave detectors offer the possibility to employ completely different interferometer topologies and consequently the search for quantum noise reduction techniques must have a wider scope. As part of my work I have considered a new configuration for future gravitational wave detectors; I study the feasibility of using a polarising Sagnac topology as an alternative to the commonly used Michelson topology. I show that a Sagnac interferometer, using realistic optical parameters, could provide a competitive low radiation pressure noise at a greatly reduced complexity of the optical design. I further propose a new method to achieve an optical readout of a Sagnac interferometer.

Generally the reduction of radiation pressure noise is significantly influenced by the optical losses, in particular, by those in optical cavities. Optical loss investigations of a cavity are therefore of great interest for the gravitational wave community. I have designed, set-up, and commissioned a new experiment to estimate the cavity optical losses in a cavity in the presence of mirror surface distortions. The preliminary results of this experiment aim to support the filter cavity development for gravitational wave detectors in the future.

The reduction of quantum noise is critical for the future of gravitational wave astronomy. This thesis provides three approaches to enable new quantum noise reduction techniques supporting the design and realisation of future gravitational wave detectors.

Contents

List of Figures

List of Tables

Glossary

AOM	acousto-optic modulator
AR	anti-reflective
BS	beam splitter
ITM	input test mass
EOM	electro-optical modulator
ET	Einstein Telescope
ETM	end test mass
FSR	free spectral range
GW	gravitational wave
HR	high reflective
LIGO	laser interferometer gravitational wave observatory
LO	local oscillator
MC	mode cleaner
NSD	noise spectral density
PBS	polarising beam splitter
PDH	Pound-Drever-Hall
PRM	power recycling mirror
PZT	Piezoelectric transducer
QWP	quarter wave plate
SRM	signal recycling mirror
WP	wave plate

Chapter 1.

Introduction

The existence of gravitational waves (GWs) was first predicted in 1916 when they were described as radiation from large accelerated masses by Einstein [3]. After nearly a century, GWs are currently one of the most appealing and cutting-edge scientific research topics world wide. Over the last few decades, various experimental measurements have been proposed and carried out attempting to confirm this prediction by Einstein's General Theory of Relativity (GR). However, even with continued technical developments, GWs have yet to be directly observed. The reason is that the GW signals expected at Earth even from large astrophysical events are extremely small. The amplitudes of differential displacements in two perpendicular directions are usually below the order of 10^{-21} [4].

Currently, the ground-based interferometric GW detector LIGO [5], which has achieved its initial sensitivity goal [6] and is currently being upgraded to Advanced LIGO [7], is recognised as the most promising detector to achieve the first GW observation soon after it comes online in 2015. Constructive implementations of advanced techniques, such as higher optical laser power [7], auxiliary thermal compensation optics [8, 9], and improved suspension and seismic isolation [10,

11], in the second generation detectors lead us into a new GW detection era in which radiation pressure noise (low-frequency quantum noise) turns out to be a dominant limitation at frequencies from 10 Hz to 50 Hz.

1.1. Physics of Gravitational Waves

GWs are one form of radiations created by varying mass distributions [3, 12]. GWs are usually described as ripples in the fabric of space-time (in GR, they are described as 'local tides') travelling at the speed of light. According to the equivalence principle, a single freely falling test body may not be affected by passing GWs. Therefore, it is not quite possible to measure GWs by a single freely falling body [13]. However, GWs do cause a change in separation between two spatial freely falling bodies, which then provides a possibility to observe the gravitational waves due to the interaction of GWs with two or more test bodies [14].

Here, we would like to present some basic physical properties of GWs to make the concepts for the detector designs which we will focus on more understandable. Note that a number of the principles in this section review texts from several books [12, 13, 14]. While a detailed treatment is beyond the scope of this work, a reader advanced in GW physics and astronomy may find more details in these references.

1.1.1. Amplitude of Gravitational Waves

It is not possible to derive analytic solutions for Einstein's equations for GR in the general case [13]. In order to estimate the amplitude of GWs, an analytical approximation, the post-Newtonian expansion, is commonly used [15]. The

slow motion approximation expands the GW matrix, resulting in an expanded radiation equation. It gives the lowest-order post-Newtonian approximation as a quadrupole formula, which depends on the quadrupole moment tensor

$$q_{kn}(t) = \int \rho x^k x^n d^3\boldsymbol{x}, \tag{1.1}$$

where ρ is the mass density and $\boldsymbol{x} = \{x^1, x^2, x^3\}$ is a three-dimension vector with the superscripts k and n being the spatial indices, where $k, n \in \{1, 2, 3\}$. The amplitude of the gravitational radiation at a distance r to the source is described by

$$h_{kn} = \frac{2G}{c^4 r}\frac{\partial^2 q_{kn}(t)}{\partial t^2}, \tag{1.2}$$

with $c \simeq 299792458\,\mathrm{m/s}$ being the speed of light and $G \simeq 6.673\times10^{-11}\,\mathrm{m^3\,kg^{-1}s^{-2}}$ being Newton's gravitational constant. Here, the amplitude is given in a Lorentz gauge with an assumption that the GW field is weak; all following discussions are based on linearised gravity.

An order-of-magnitude Estimate

The amplitude of GWs can be estimated by Eq. (1.2). It has been found that strong GW sources are usually highly non-spherical and the quadrupole moment q_{kn} of the source will have a magnitude of ML^2, where M is the mass of the source and L is the size [16]. Correspondingly, we have the second order derivation of the moment

$$\ddot{q}_{kn} \approx 2Mv^2 \approx 4E_{kin}^{non}, \tag{1.3}$$

where $E_{kin}^{non} = 1/2Mv^2$ is the non-spherical part of the kinetic energy inside the source with v being the internal velocity. The above approximation is based on the largest sources, and an upper bound of Eq. (1.2) thus can be given as

$$h \lesssim \frac{2}{c^2}\frac{G2Mv^2/c^2}{r} = \frac{2}{c^2}\frac{4GE_{kin}^{non}/c^2}{r}. \tag{1.4}$$

From Eq. (1.4), we can see that a strong radiation h is generated by a very large, non-spherical, internal kinetic energy source and the most direct way known to achieve a huge internal kinetic energy is through gravity [16].

According to energy conservation, the gravitationally-induced kinetic energy has the same order as the source's gravitational potential energy [16]. A huge potential energy requires a very compact source, in fact, the strongest GWs must be generated by highly compact, dynamical concentrations of large mass. For highly compact sources, e.g., colliding and coalescing neutron stars and stellar-mass black holes, the internal, non-spherical kinetic energy E_{kin}^{non}/c^2 is of the same order of *solar mass* $M_\odot$. Following Eq. (1.4), it correspondingly gives $h \sim 10^{-22}$ at the Hubble distance 3000 Mpc[1], which is 10^{10} light years; and $h \sim 10^{-17}$ at the outer edge of our Milky Way galaxy (20 kpc) [16].

1.1.2. Polarisation of Gravitational Waves

According to the energy conservation principle, GWs have two independent states of polarisations: the plus polarisation ('+') and the cross polarisation ('×'). The angle between the two polarisations is $\pi/4$. Usually, we denote the plus polarised GWs as h_+, and the cross as $h_\times$. The effects of the two orthogonally polarised waves acting on a ring of freely falling particles are illustrated in Fig. 1.1[2].

[1] This is a simple estimation of the amplitude of the expected GW signal. To compute the signal-to-noise ratio of the signal against a particular noise power spectral (which is usually given as the noise spectral density [7]) will require the accurate waveform in the frequency domain [17].

[2] Note that the wavelength λ of the incoming GW must be far larger than the separation distances between the particles because we have assumed that $|h_{kn}| \ll 1$ [18].

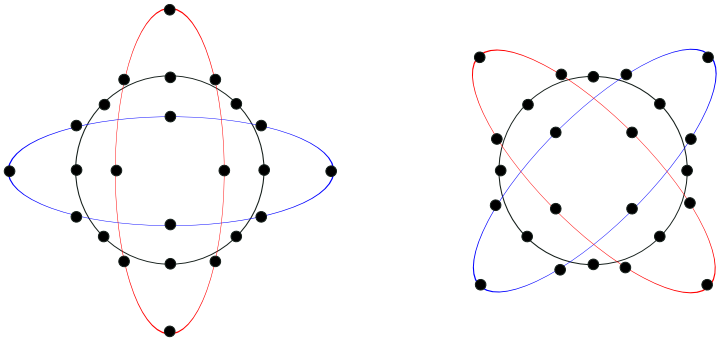

Figure 1.1.: Effects of the '+' and '×' polarisation when a GW interacts with a circular ring of particles. The ring of particles are arranged in the x-y plane, and the GW is travelling orthogonal to this plane in the z direction. The lefthand panel illustrates the effect of a '+' polarised GW and the righthand panel shows the '×' polarised GW influence. The circle repeatedly stretches into one of the ellipses and back in the first half period of a GW and gets squeezed into the other ellipse and back during the second half period.

1.1.3. Frequency of Gravitational Waves

There are many available frequency predictions of GWs either from an existing motion, e.g., the spin of a pulsar, or from the natural frequency of a self-gravitating body [13]. For most cases, the frequency will be associated to the natural frequency f_0 of the astro-body, which is usually given as

$$f_0 = \sqrt{G\bar{\rho}/4\pi} = \frac{1}{4\pi}\left(\frac{3MG}{R^3}\right)^{1/2}. \tag{1.5}$$

The mean density $\bar{\rho}$ is characterised by the source radius R and mass M, commonly taking $\bar{\rho} = 3M/4\pi R^3$. Although this equation is derived under a Newtonian formalism, the frequency estimation has the same order as the binary orbital frequency and the fundamental pulsation frequency of the body [13]. Therefore, it makes a good order-of-magnitude prediction of the frequency of a GW from the estimation of natural frequency. However, the frequency of GWs must not

necessarily match the natural frequency, even if it is basically an oscillation with that frequency. For instance, it has been found that for binary systems GWs are emitted at twice the natural frequency.

Using Eq. (1.5), we can roughly estimate the natural frequency of a binary system $f_0 \approx 400\,\mathrm{Hz}$, which consists of two neutron stars with reduced mass being 1.4 $M_\odot$ and separation distance being 20 km. The frequency of GWs is thus twice of the natural frequency $f_\mathrm{h} = 2f_0$. At the same time, we can calculate the amplitude of GWs which is $h \approx 10^{-21}$ assuming the binary system is located 10 Mpc away. The above results suggest that the GW signals emitted by such a binary system will be good sources for ground-based GW detectors.

1.2. Detection Concepts

Direct GW detection on Earth is an experimental challenge due to the small amplitude of GW signals (see Section 1.1.1). A Michelson laser interferometric GW detector is currently the most promising tool in the GW detection field as it naturally senses the displacement difference between two perpendicular directions as shown in Fig. 1.2. This is the simplest Michelson interferometer, in which an input laser beam is split by the central beam splitter (BS) into two beams and then travels in two perpendicular directions separately. These two separate optical paths are usually referred to as *interferometer arms*. The two beams are reflected by mirrors, also called, *end test masses* (ETMs), back to the BS and interfere with each other. At the ports where the laser and photodiode are placed, we can see different interference patterns depending on the arm length difference (ΔL in Fig. 1.2). It is known that when two arm lengths are identical, the port where the laser is sitting has constructive interference and the photodiode located port has destructive interference. Therefore, they are frequently called the *bright port* and

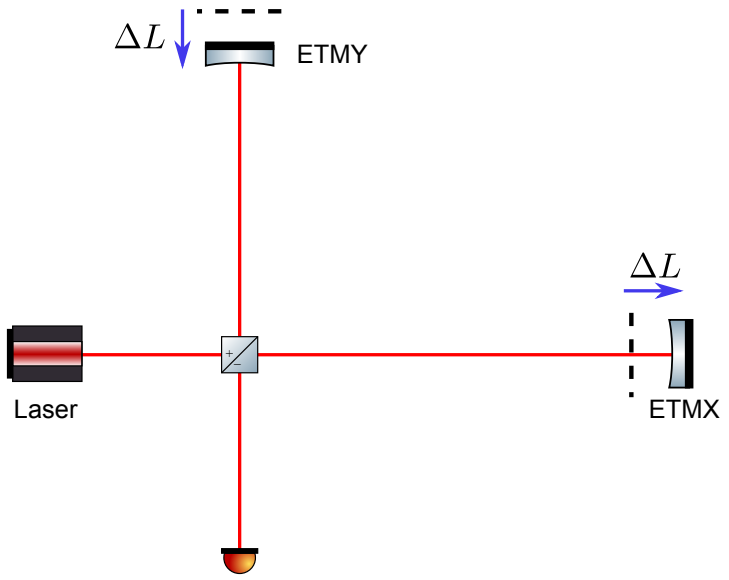

Figure 1.2.: Schematic showing a simple Michelson interferometer when the horizontal arm is stretched while the perpendicular arm is squashed by ΔL. Dashed lines mark the original mirror positions with initially equal arm length L for both arms. ETMX/Y are end mirrors which follow LIGO notation labelled as end test masses (ETMs).

the *dark port*, respectively. All the current ground-based GW detectors (LIGO, Virgo, and GEO600) are based on the Michelson topology. We will show more details of realistic laser interferometric GW detectors in the following sections and focus on the configuration of Advanced LIGO.

1.2.1. Laser Interferometric Gravitational-wave Detectors

First generation large-scale interferometric GW detectors such as LIGO are designed based on a Michelson topology and upgrades are therefore generally bound on their original infrastructure. A laser Michelson interferometer is highly suitable in measuring the length differences between two perpendicular directions by detecting the intensity at the dark port (see Fig. 1.2) as illustrated in Fig. 1.3.

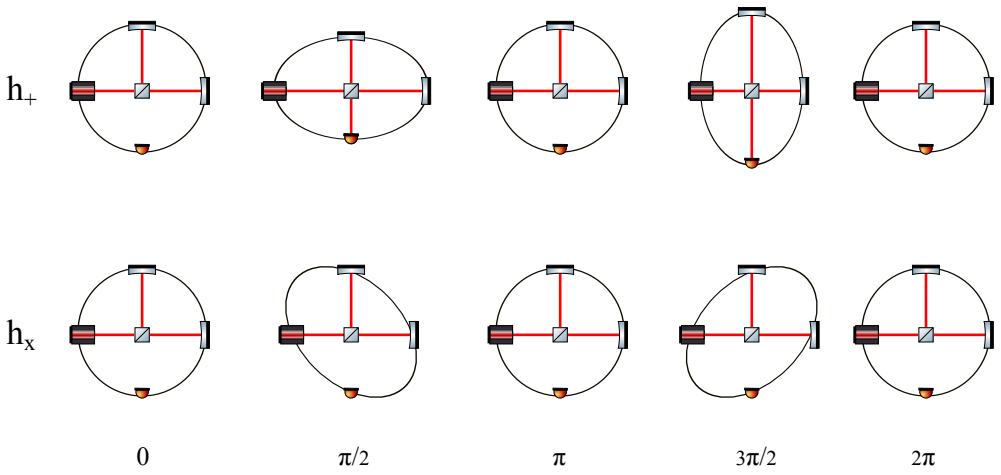

Figure 1.3.: Outputs of a Michelson interferometer when a GW signal with either '+' polarisation (upper) or '×' polarisation (lower) is passing through in one period time (also see Fig. 1.1). A Michelson interferometer is naturally sensitive to the '+' polarisation motion and has null-response to the '×' polarisation effect.

It converts the phase shift of an optical field into an intensity modulation at the output detected by photodetectors and is naturally suited for GW detection. The intensity modulation frequency is therefore determined by how fast the arm lengths change and in our case it is associated to the frequency of GW signals.

Relating the phase shift to length measurement, the GW signal strain is defined by the stretch and squash length difference in arms as (see Fig. 1.2):

$$h = \frac{2\Delta L}{L}, \tag{1.6}$$

or

$$h = \frac{\lambda}{2\pi}\frac{\Delta\phi}{2L}, \tag{1.7}$$

where ΔL is the change in arm length caused by a passing GW signal, $\Delta\phi = 2 \cdot k \cdot \Delta L$ is the arm length change induced phase shift with the wave number $k = 2\pi/\lambda$, λ is the input laser wavelength, and L is the original arm length.

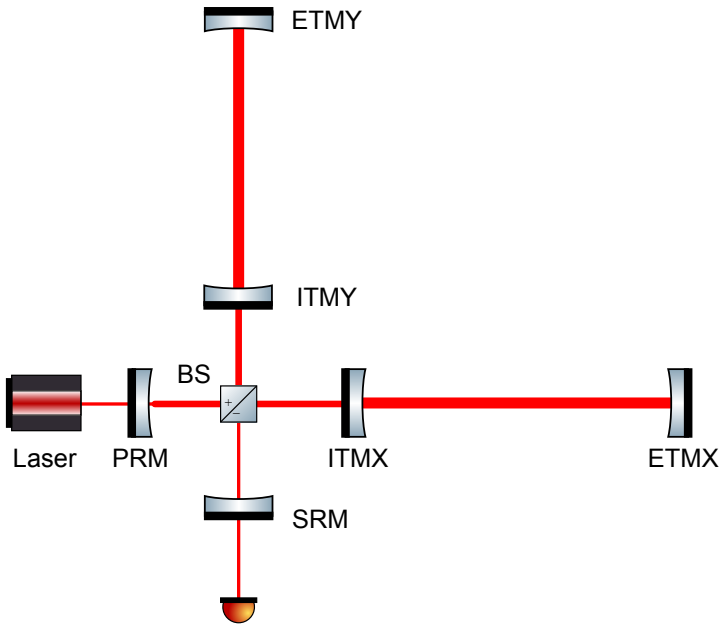

Figure 1.4.: Schematic showing a dual-recycled Michelson interferometer with resonant arm cavities. The differential motion of two arms (with arm cavities consisting of the input test mass (ITM) and the end test mass (ETM)) may create similar displacement as the simple Michelson interferometer as shown in Fig 1.2. The power recycling mirror (PRM) and the signal recycling mirror (SRM) with ITMs form the *power-recycling cavity*, and *signal-recycling cavity*, respectively. It is therefore referred to as a *dual-recycling configuration*.

An optimum sensitivity could be achieved if the travelling time of the laser light in the arm of a Michelson interferometer is one half period of a GW. For a GW signal with a frequency of about 100 Hz, the travelling time is about 5 ms, which corresponds to an optical path (round-trip) of 1500 km and requires one arm with a length of 750 km. An interferometer with such long arms is impractical because of high costs and other installation issues. In order to increase the signal storage time, optical delay lines have been proposed [19], but Fabry-Pérot cavities have eventually been chosen [20].

Using Fabry-Pérot cavities in the arms is an alternative way to increase the optical path length [21]. It only requires mirrors to be slightly larger than a diffraction-limited beam [22]. Fabry-Pérot arm cavities have a number of advantages over delay lines in terms of rigid requirements for mirror manufacturing and reduced unwanted light fields. In this thesis, only interferometers with linear Fabry-Pérot arm cavities will be considered.

Figure 1.4 shows a Michelson interferometer with the Fabry-Pérot arm cavities, each being formed by two mirrors: the input test mass (ITM) and the end test mass (ETM). It senses the arm length difference in a similar way as a simple Michelson (see Fig. 1.2). In this figure, both the power recycling mirror (PRM) and the signal recycling mirror (SRM) are included and form a *dual-recycling* Michelson configuration [23]. The PRM amplifies the optical power entering the arm cavities. The SRM is used for GW signal amplification [24, 25, 26]. This configuration illustrates a Michelson topology similar to Advanced LIGO (with folded recycling cavities) [7]. Since our investigations are not concerned with the detailed design of the recycling cavities, we will represent the Advanced LIGO configuration in this thesis using the simplified schematic as shown in Fig. 1.4.

1.3. Noises Sources for advanced GW Detectors

Although a Michelson interferometer is well suited to observe GWs, in particular with arm cavities and dual-recycling configuration (see Fig. 1.4), a successful direct detection is still challenging. This is due to different noise sources produce a same level of displacement to the test masses at the frequency range as potential GWs do (see Eq. (1.6)); and thus mask the GW signals. For advanced GW detectors, the major noises limiting detection sensitivity are *seismic noise*, *Newtonian noise* (also referred to as *gravity gradient noise*), *suspension thermal*

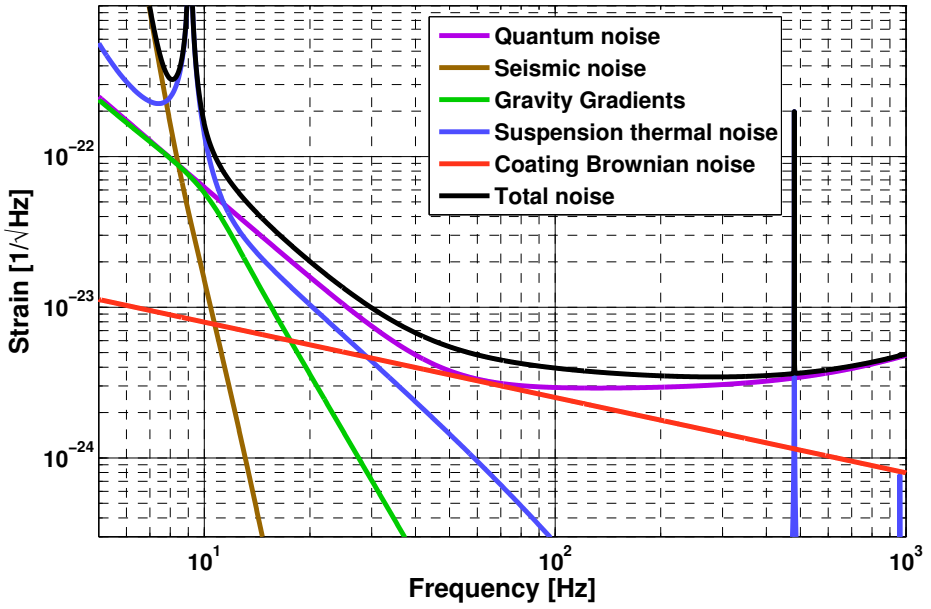

Figure 1.5.: Plot showing the strain noise spectral density of Advanced LIGO with 125 W input power. The dominant noise sources are seismic noise, gravity gradient noise, mirror and suspension thermal noise, and quantum noise. This plot is generated by GWINC [27].

noise, *mirror coating thermal noise*, and *quantum noise*. For instance, Fig. 1.5 shows the noise budget of Advanced LIGO, limited by the above noises. Various advanced techniques have been explored and developed to reduce these noises, i.e., better mirror coating, better suspension system, or cryogenic mirrors [7].

1.3.1. Other Noises

Seismic and Newtonian noise

On Earth, the ground is never quiet but in continuous motion caused by human activities, winds, ocean waves and so on [28]. The ground motion produces two noises: vibrational seismic noise and Newtonian noise [29]. Seismic noise induces

direct displacements of the test masses, while Newtonian noise is due to mass density fluctuations produced by seismic motion and results in fluctuating Newtonian gravitational forces that induce motions in the test masses. Seismic Newtonian noise thus is also referred to as gravity gradient noise. Both seismic noise and Newtonian noise are important in the low frequency range, $f < 10\,\mathrm{Hz}$.

With the super *attenuator* [30] in future generation GW detectors, it will be possible to practically isolate the test masses from seismic vibrations down to the gravity gradient noise limit as low as 1 Hz [29, 31]. This can be seen from the conceptual design of the Einstein Telescope [32]. This third generation GW detector shows a design cut-off frequency of seismic noise at around 1 Hz [32](page 18). However, seismic isolation is not practical to reduce the fluctuating gravity gradients, which means Newtonian noise cannot be isolated with advanced isolation techniques. The location of a GW detector is rather important as quiet places with lower seismic vibrations will be naturally suitable choices with low Newtonian noise. Placing detectors underground presents a further improvement in having lower Newtonian noise as the contribution to Newtonian noise from surface waves significantly reduces with depth [33]. Newtonian noise may also be suppressed by using accelerometers around the test masses and applying active noise cancellation [34, 35].

Thermal noise

GW detector thermal noise arises mainly from two origins: material Brownian motion of atoms and molecules at non-zero temperature (Brownian noise), and temperature fluctuations in a finite volume of material (thermo-elastic noise) [36, 37].

Due to a continuous thermal energy exchange of the suspension wires (usually,

last stage) and test masses (mirror substrates and coatings) with the environment at thermal equilibrium [38] via dissipation mechanisms [22], the Brownian motion induces random thermal motion of the suspended test masses and affects the arm lengths of the detectors. Meanwhile, the internal temperature fluctuations can also couple with GW strain via the thermal expansion ultimately producing random motion of the mirror surfaces. Hence, thermal noise is governed by material mechanical losses and temperature.

For advanced and 3rd generation GW detectors, it has been recognised that the dominating sources of thermal noise are suspension thermal noise and Brownian noise of the mirror coating [37, 39, 40, 41]. Figure 1.5 shows the noise levels of respective noises for Advanced LIGO.

Different approaches have been proposed that could reduce thermal noise.

- **Low dissipation materials**

  According to the fluctuation-dissipation theorem, a straightforward solution is to have low mechanical loss materials. Henceforth, GW detector test masses and suspension wires are preferably fabricated from low mechanical loss materials and usually with suspension designs having resonant modes outside the detection frequency band [22]. Coatings of the test masses have been identified as a significant contribution to Brownian thermal noise. Therefore, coating materials with low dissipation are required to reduce mirror coating thermal noise [42].

- **Low temperature**

  Cryogenic test masses and suspensions will result in lower thermal noise for GW detectors [43]. Future GW detectors, such as KAGRA [44] and ET [32], will be operated cryogenically to reduce further thermal noise. Cooled materials such as sapphire and silicon have been investigated [45]. However,

due to open questions related to the technologies of cryogenic coatings & substrates, as well as coating material properties at cryogenic temperature, realistic implementation is still under investigation.

- **Alternative beam shapes**

  Using beams with a more even intensity distribution could reduce the mirror thermal noise [46, 47]. This is because they are more effectively averaged over mirror surface distortions caused by thermal noise [47]. There are several options of beams whose intensity averages over the mirror surface, such as Mesa beams [48], conical beams [49] and higher-order Laguerre-Gauss (LG) beams, i.e., LG_{33} [50].

1.3.2. Quantum Noise

The modern ground-based GW detectors are laser interferometers. It is known that even an ideal laser has amplitude and phase fluctuations. The *coherent state* has been recognised as the best quantum mechanical approximation to the laser field since its major properties are similar to those of classical fields. Figure 1.6 graphically represents a typical coherent state in two forms: phasor diagram and time evolution series. The phasor diagram of the coherent state shows that it can be understood as a displaced *vacuum state* and the fluctuations are equal to those of a vacuum state. The displacement amount $\bar{E}$ is associated with the complex amplitude of a classical wave as illustrated in Fig. 1.6 (ii).

Quantum noise resulting from these fluctuations will ultimately limit the detection sensitivity. In the GW community, the low-frequency quantum noise is called *radiation pressure noise* (or *back-action noise*) and the high-frequency quantum noise is referred to as *shot noise*.

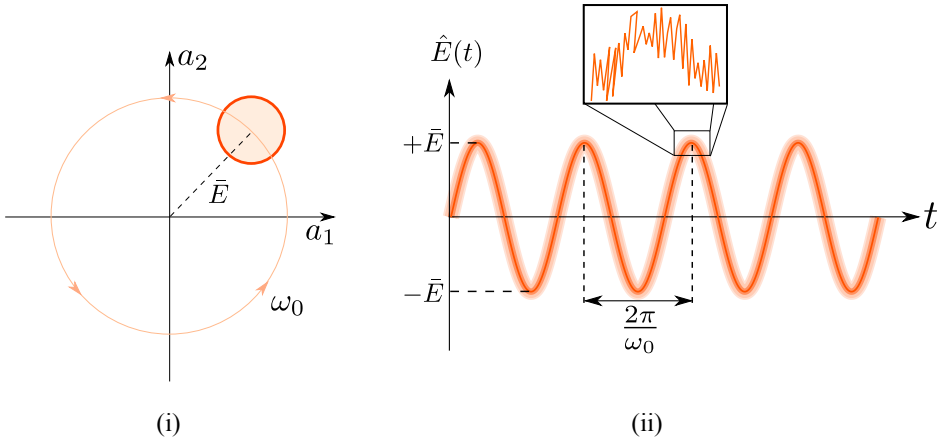

Figure 1.6.: Two representations of a coherent state: (i) phasor diagram and (ii) time evolution of the electric field. Image courtesy H. Miao.

Shot noise

The detection of GWs is based on measurements of the optical power at the output (dark port) of an interferometer, which means the length difference between the two arms is deduced from the number of photons arriving at the photodetector during a measurement interval. Shot noise is the counting noise of the discrete number of photons, which follow a probability distribution - a *Poisson distribution*. The mean number of photons during a measurement interval τ is given as $\bar{N} = I\tau/(\hbar\omega_0)$ with I the power and ω_0 the laser frequency. The power fluctuation $\sigma_{\bar{N}}$ therefore is $\sqrt{\bar{N}}$. A fractional photon number fluctuation thus is expected as $\sigma_{\bar{N}}/\bar{N} = 1/\sqrt{\bar{N}}$. Converting the power fluctuation into position fluctuation, we have

$$\sigma_{\delta_L}^{\mathrm{sh}} = \frac{1}{k\sqrt{\bar{N}}}, \tag{1.8}$$

where $k \equiv 2\pi/\lambda \equiv \omega_0/c$ and the superscript 'sh' stands for shot noise. The displacement noise spectral density therefore is

$$S_{\mathrm{sh}}^{x} = \sigma_{\delta_L}^2 \tau = \frac{\hbar c^2}{I\omega_0}. \tag{1.9}$$

Recalling Eq. (1.6), we describe the shot noise in terms of the gravitational wave strain h as

$$h_{\rm sh}(\Omega) = \frac{1}{L}\sqrt{S^x_{\rm sh}(\Omega)} = \frac{1}{L}\sqrt{\frac{\hbar c^2}{I\omega_0}}. \tag{1.10}$$

The above equation shows that the shot noise can be reduced by increasing the laser power.

Radiation pressure noise

Radiation pressure forces are caused by the pressure exerted on mirror surfaces which are exposed to electromagnetic radiation. For an ideal mirror at the end of an interferometer arm, the power I in one arm will be totally reflected and will exert a force on the mirror as

$$F_{\rm rp} = \frac{2I}{c}. \tag{1.11}$$

Radiation pressure noise is raised by the power fluctuations interacting with mirrors as force fluctuation

$$\sigma_F = \frac{2\sigma_I}{c} = \frac{2\sigma_{\bar{N}}\hbar\omega_0}{c\tau} = \frac{2\sqrt{\bar{N}}\hbar\omega_0}{c\tau}. \tag{1.12}$$

If mirrors are considered to be free masses and with mass m, the fluctuating force causes a displacement fluctuation of

$$\sigma^{rp}_{\delta L} = \frac{1}{m\Omega^2}\sigma_F, \tag{1.13}$$

where $1/m\Omega^2$ is the transfer function of a free mass and Ω is the frequency of the induced displacement. The displacement noise spectrum due to these radiation pressure fluctuations in turn is

$$S^x_{\rm rp} = \sigma^2_{\delta_L}\tau = \frac{1}{m^2\Omega^4}\frac{2I\hbar\omega_0}{c^2}, \tag{1.14}$$

and the radiation pressure noise in h is

$$h_{\mathrm{rp}}(\Omega) = \frac{1}{L}\frac{\sqrt{2I\hbar\omega_0}}{m\Omega^2 c}, \tag{1.15}$$

which tells us that the radiation pressure noise is proportional to optical power.

Standard quantum limit

Quantum noise, namely the sum of shot noise and radiation pressure noise, can therefore be expressed as

$$h_{\mathrm{total}}(\Omega) = \sqrt{h_{\mathrm{sh}}^2(\Omega) + h_{\mathrm{rp}}^2(\Omega)} = \frac{1}{L}\sqrt{\frac{\hbar c^2}{I\omega_0} + \frac{2I\hbar\omega_0}{m^2\Omega^4 c^2}} \geq \underbrace{\frac{1}{L}\sqrt{\frac{8\hbar}{m\Omega^2}}}_{\mathrm{SQL}}. \tag{1.16}$$

It is true that shot noise can be reduced by utilising a sufficiently high power input laser, however, at low frequencies radiation pressure noise simultaneously increases (see Fig. 1.7). There is a boundary known as the Standard Quantum Limit (SQL), defined in Eq. (1.16), that imposes a restriction on the quantum noise reduction [51, 52] as a trade-off between the two noises.

Quantum noise reduction

At first glance, it does not seem possible to directly reduce quantum noise over a broad frequency band by purely increasing input laser power (see Eq. (1.7)). However, a number of techniques have been proposed that allow us to reduce low-frequency quantum noise simultaneously or even surpass the SQL, by means of creating a correlation between the shot noise and the radiation pressure noise via: (i) a signal-recycled Michelson [53], (ii) frequency-dependent squeezing [54, 55], (iii) frequency-dependent readout [54], and (iv) a speed meter [56, 57, 58], *etc.* Since quantum noise of a GW detector not only relies on the laser source but also is closely related to its optical configuration and auxiliary optics, in Chapter 3 and

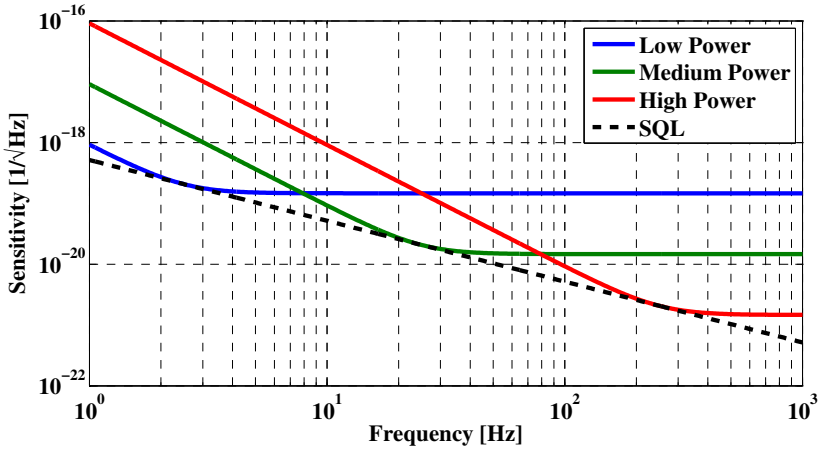

Figure 1.7.: Plots showing the quantum noise levels for different levels of input power. The shot noise at high frequencies decreases with higher power, however, the radiation pressure noise increases. The black line shows quantum noise, a sum of shot noise and radiation pressure noise, over different laser powers, which forms a boundary of quantum noise called the Standard Quantum Limit (SQL).

4 further discussions on various interferometer schemes to reduce the radiation pressure noise will be carried out in greater detail.

1.4. Thesis Structure

My thesis is focusing on quantum noise reduction techniques accounting for some realistic factors, e.g., imperfect optics, for the next generation GW detectors. This thesis aims to demonstrate various methods which can be practically implemented in reducing the low-frequency quantum noise for future GW detectors.

Chapter 1 gives a brief introduction to the physics of gravitational waves, the interferometric detection concept, and the limiting noises for the advanced gravitational wave detectors. A qualitative and quantitative description of quantum

noise (namely the radiation pressure noise and the shot noise) analysis is given in this chapter.

Chapter 2 describes the quantised electromagnetic field using the two-photon formalism. The quantum noise of typical optical systems are deduced using this formalism, and these models are expanded for a generic interpretation by using block diagrams. The quantum noise of Advanced LIGO is represented using this method.

Chapter 3 presents three types of filtering schemes. Section 3.1 compares the input and output filtering schemes in terms of a broadband quantum noise reduction. The effects of optical losses from filter cavities and other optics have been investigated. Section 3.2 gives a comprehensive analysis of different intra-cavity filtering schemes.

Chapter 4 reports an alternative GW detector topology, a polarising Sagnac interferometer, for the Einstein Telescope low frequency interferometers. A polarising Sagnac interferometer with greatly reduced complexity has been investigated with emphasis on the implementation of a DC readout scheme.

Chapter 5 presents the design and setup of a table-top experiment, a linear Fabry-Pérot cavity with a length varying from 2 cm to 2 m, to measure the cavity optical losses as a function of the cavity length. The experiment is under construction. We provide two analytical models to estimate the cavity finesse, which could be directly used once the setup is ready.

Chapter 6 provides a conclusion and discussion of the work carried out in this thesis.

Appendix A gives a full description of a generic two-mirror Fabry-Pérot cavity, including the light fields responses in different conditions. The characteristic parameters, such as the cavity finesse, the cavity bandwidth, and the free spectral

range are explicitly defined.

Appendix B shows the detailed input-output relation and definition for the three-port-junction in the intra-cavity scheme as shown in Section. 3.2.

Appendix C presents the complete output equations of the imperfect polarising Sagnac interferometer as shown in Section. 4.3.2.

Chapter 2.

Quantum Noise of Gravitational Wave Detectors

Quantum noise will limit the sensitivity of advanced GW detectors, such as Advanced LIGO, Advanced VIRGO and future GW observatories, such as ET. How to reduce the quantum noise is now one of the most important challenges in GW instrumentation. Throughout this chapter, we will discuss the quantum nature of the light field. We investigate how the quantised light field interacts with mirrors and couples into the motion of mirrors in GW detectors. It is known that the quantum noise of a detector differs with its diverse topologies and configurations. First, we introduce the quantised light field using the two-photon formalism and derive the quantum noise of several basic optical setups. We express the quantum mechanics involved in this framework and compile models for a generic interpretation towards a comprehensive quantum noise analysis for more realistic GW detectors.

2.1. Quantised Electromagnetic Field

Following the common convention, all the electromagnetic fields stated in this thesis are expressed only by their electric field components. A quantised electromagnetic field or rather a quantised electric field can be expressed as a linear superposition of the annihilation operator $\hat{a}(\omega)$ and creation operator $\hat{a}^\dagger(\omega)$ as (propagating in one direction):

$$\hat{E}(z,t) = \sqrt{\frac{2\pi}{\mathcal{A}c}} \int_0^\infty \frac{d\omega}{2\pi} \sqrt{\hbar\omega} \left[\hat{a}(\omega) e^{-i\omega(t-z/c)} + \hat{a}^\dagger(\omega) e^{i\omega(t-z/c)}\right], \tag{2.1}$$

with the commutation relation

$$[\hat{a}(\omega), \hat{a}^\dagger(\omega')] = 2\pi\delta(\omega - \omega'), \tag{2.2}$$

where $\mathcal{A}$ is the transverse area of the optical beam. This formalism is a quite natural choice for the description of quantised electric fields. However, this description is not convenient to investigate an optical system which involves a pair of photos simultaneously at frequencies $\omega_0 \pm \Omega$, such as laser interferometers for GW detection. Thus, an alternative formalism which is more suitable to treat these sidebands is the two-photon formalism invented by Caves [59]. While comprehensive descriptions of the quantised field are beyond the scope of our work, a reader advanced in quantum mechanics and quantum optics may find more details in these books [60, 61]. We will only focus our investigation on the electric fields represented by these sidebands. More details are presented in the following sections.

2.1.1. Two-photon Formalism

In 1985, Caves [59] introduced a so-called two-photon formalism which uses a new pair of operators to describe the amplitude quadrature and phase quadrature of

the electric field. The corresponding operators involve creation of a photon at $\omega_0 \pm \Omega$ and annihilation of one at $\omega_0 \mp \Omega$ simultaneously.

Before introducing these quadrature operators, we first introduce the annihilation operator for the sidebands that later will be used for defining quadrature operators:

$$\hat{a}_+ = \hat{a}(\omega_0+\Omega)\sqrt{1+\frac{\Omega}{\omega_0}}, \qquad \hat{a}_- = \hat{a}(\omega_0-\Omega)\sqrt{1-\frac{\Omega}{\omega_0}}. \tag{2.3}$$

With these, the electric field at a certain position[1] can be re-written into

$$\begin{aligned} E(t) &= \sqrt{\frac{2\pi\hbar\omega_0}{\mathcal{A}c}}\int_0^\infty \frac{d\Omega}{2\pi}\sqrt{\frac{\omega_0+\Omega}{\omega_0}}\left[\hat{a}(\omega_0+\Omega)e^{-i(\omega_0+\Omega)t}+\hat{a}^\dagger(\omega_0+\Omega)e^{i(\omega_0+\Omega)t}\right] \\ &+ \sqrt{\frac{2\pi\hbar\omega_0}{\mathcal{A}c}}\int_0^{\omega_0} \frac{d\Omega}{2\pi}\sqrt{\frac{\omega_0-\Omega}{\omega_0}}\left[\hat{a}(\omega_0-\Omega)e^{-i(\omega_0-\Omega)t}+\hat{a}^\dagger(\omega_0-\Omega)e^{i(\omega_0-\Omega)t}\right] \\ &= \sqrt{\frac{2\pi\hbar\omega_0}{\mathcal{A}c}}e^{-i\omega_0 t}\left(\int_0^\infty \frac{d\Omega}{2\pi}\hat{a}_+e^{-i\Omega t}+\int_0^{\omega_0}\frac{d\Omega}{2\pi}\hat{a}_-e^{i\Omega t}\right)+H.C., \end{aligned} \tag{2.4}$$

where $H.C.$ is the *Hermitian conjugate*, ω_0 is the carrier angular frequency ($\sim 10^{15}$ Hz) and Ω is the sideband frequency (usually from 1 to 1000 Hz). Similar commutation relations can be derived by using the same definition as in Eq. (2.2)

$$[\hat{a}_+,\hat{a}^\dagger_{+'}] = 2\pi\delta(\Omega-\Omega')\left(1+\frac{\Omega}{\omega_0}\right), \qquad [\hat{a}_-,\hat{a}^\dagger_{-'}] = 2\pi\delta(\Omega-\Omega')\left(1-\frac{\Omega}{\omega_0}\right), \tag{2.5}$$

where $\hat{a}_{\pm'}$ represents $\hat{a}(\omega_0\pm\Omega')\sqrt{1\pm\Omega'/\omega_0}$.

For ground based GW detectors, the sideband frequency Ω is roughly between 1 Hz and 1000 Hz. Therefore, we have $\Omega/\omega_0 \ll 1$. The integration limit for the second term of Eq. (2.4) can thus be extended to infinity and finally we obtain

$$E(t) = \sqrt{\frac{2\pi\hbar\omega_0}{\mathcal{A}c}}e^{-i\omega_0 t}\int_0^\infty \frac{d\Omega}{2\pi}\left[\hat{a}_+e^{-i\Omega t}+\hat{a}_-e^{i\Omega t}\right]+H.C., \tag{2.6}$$

with the commutation relations

$$[\hat{a}_+,\hat{a}^\dagger_{+'}] = 2\pi\delta(\Omega-\Omega'), \qquad [\hat{a}_-,\hat{a}^\dagger_{-'}] = 2\pi\delta(\Omega-\Omega'). \tag{2.7}$$

[1] We neglect the variable z in our description.

The commutation relations in Eqs. (2.2) and (2.5) tell us that none of the normal creation and annihilation operators $\hat{a}(\omega)$, $\hat{a}^\dagger(\omega)$ and the new plus and minus creation and annihilation operators $\hat{a}_+$, $\hat{a}_-$ are hermitian operators; they cannot be detected directly.

The Hermitian quadrature operators are defined as:

$$\hat{a}_1 = \frac{\hat{a}_+ + \hat{a}_-^\dagger}{\sqrt{2}}, \qquad \hat{a}_2 = \frac{\hat{a}_+ - \hat{a}_-^\dagger}{\sqrt{2}i}. \tag{2.8}$$

We notice the commutation relations

$$[\hat{a}_1, \hat{a}_{2'}^\dagger] = 2\pi i\delta(\Omega - \Omega'), \qquad [\hat{a}_2, \hat{a}_{1'}^\dagger] = -2\pi i\delta(\Omega - \Omega'),$$

and

$$\underline{[\hat{a}_1, \hat{a}_{1'}^\dagger]} = [\hat{a}_1, \hat{a}_{1'}] = \underline{[\hat{a}_2, \hat{a}_{2'}^\dagger]} = [\hat{a}_2, \hat{a}_{2'}] = 0. \tag{2.9}$$

Recalling Eq. (2.6), we can express the electric field in terms of these quadrature operators $\hat{a}_1$ and $\hat{a}_2$ as

$$\hat{E}(t) = \cos(\omega_0 t)\hat{a}_1(t) + \sin(\omega_0 t)\hat{a}_2(t), \tag{2.10}$$

where the time-domain $\hat{a}_{1,2}(t)$, more explicitly, are given by:

$$\hat{a}_{1,2}(t) = \sqrt{\frac{4\pi\hbar\omega_0}{\mathcal{A}c}} \int_0^\infty \frac{d\Omega}{2\pi} \left[\hat{a}_{1,2}e^{-i\Omega t} + \hat{a}_{1,2}^\dagger e^{i\Omega t}\right] \equiv \sqrt{\frac{4\pi\hbar\omega_0}{\mathcal{A}c}} \int_{-\infty}^\infty \frac{d\Omega}{2\pi} \hat{a}_{1,2}e^{-i\Omega t}. \tag{2.11}$$

Note that $\hat{a}_{1,2}(t)$ both commute with themselves at different times. They are thus quantum non-demolition variables and can be measured precisely and continuously in time. Corresponding to a classical field description, $\hat{a}_1$ and $\hat{a}_2$ are simply the *amplitude quadrature* and *phase quadrature*, which can be linearly combined and measured by homodyne detection.

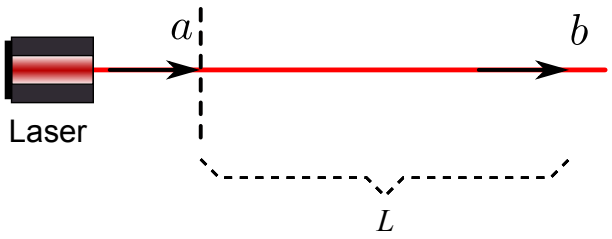

Figure 2.1.: Schematic of a laser beam propagating a distance of L from a to b. The vertical dashed line shows the reference position.

2.2. Quantum Noise of Simple Lossless Optical Systems

We will first establish the basics for analysing quantum noise before considering sophisticated interferometric configurations. Because the complete analysis of the quantum noise of a realistic GW detector, for example, an advanced GW detector with a dual-recycled configuration and arm cavities can be quite complicated and not very intuitive. We can take advantage of the linearity of the system, and decompose the highly complicated interferometric GW detectors into simple systems, for each of which the quantum dynamics is transparent. In the following sections, the quantum dynamics of four most intuitive and essential systems are illustrated in detail, following the same definitions used by [54, 59, 62, 63]. We will compile these simple setups into modules, and each can be directly applied to an analysis of more complex configuration consisting of them. We first assume lossless optics, and later generalize to the lossy cases.

2.2.1. Free Space Propagation

We first consider the transformation of the quadrature field amplitudes of the simplest case where the light field propagates a distance of L. By comparing the

electric field at $z = 0$ ($t = t$) and $z = L$ ($t = t + L/c$), the input-output relation can be attained. Shown in Fig. 2.1, a laser pumped optical field can be simply treated as an electric field consisting of a carrier and vacuum fluctuations (see Section 1.3.2):

$$\hat{E}_a(t) = [\hat{a}_1(t) + \Lambda \cos\theta_0]\cos(\omega_0 t) + [\hat{a}_2(t) + \Lambda \sin\theta_0]\sin(\omega_0 t), \tag{2.12}$$

where $\Lambda = \sqrt{2I_0/(\hbar\omega_0)}$. For convenience, we set $\theta_0 = 0$. Rearranging the above equation, we obtain

$$\hat{E}_a(t) = [\hat{a}_1(t) + \Lambda]\cos(\omega_0 t) + \hat{a}_2(t)\sin(\omega_0 t). \tag{2.13}$$

When a laser beam propagates a distance L from position a, the electric field at b can be written directly from a as:

$$\begin{aligned}
\hat{E}_b(t) =& \hat{E}_a\left(t - \frac{L}{c}\right) \\
=& \left[\hat{a}_1\left(t - \frac{L}{c}\right) + \Lambda\right]\cos\left(\omega_0 t - \frac{\omega_0 L}{c}\right) + \hat{a}_2\left(t - \frac{L}{c}\right)\sin\left(\omega_0 t - \frac{\omega_0 L}{c}\right), \\
=& \left[\hat{a}_1\left(t - \frac{L}{c}\right) + \Lambda\right]\left[\cos(\omega_0 t)\cos\left(\frac{\omega_0 L}{c}\right) + \sin(\omega_0 t)\sin\left(\frac{\omega_0 L}{c}\right)\right] \\
&+ \hat{a}_2\left(t - \frac{L}{c}\right)\left[\sin(\omega_0 t)\cos\left(\frac{\omega_0 L}{c}\right) - \cos(\omega_0 t)\sin\left(\frac{\omega_0 L}{c}\right)\right].
\end{aligned} \tag{2.14}$$

Rewriting the electric field $\hat{E}_b(t)$ in the same format:

$$\hat{E}_b(t) = \left[\hat{b}_1(t) + \Lambda\right]\cos(\omega_0 t) + \hat{b}_2(t)\sin(\omega_0 t), \tag{2.15}$$

and comparing with Eq. (2.14), we obtain the frequency domain free space propagation input-output quadrature transformation:

$$\begin{bmatrix} \hat{b}_1(\Omega) \\ \hat{b}_2(\Omega) \end{bmatrix} = e^{i\varphi}\mathbf{R}[\phi]\begin{bmatrix} \hat{a}_1(\Omega) \\ \hat{a}_2(\Omega) \end{bmatrix}, \qquad \mathbf{R}[\phi] = \begin{bmatrix} \cos\phi & -\sin\phi \\ \sin\phi & \cos\phi \end{bmatrix}, \tag{2.16}$$

with

$$\phi = \frac{\omega_0 L}{c}, \qquad \varphi = \frac{\Omega L}{c}.$$

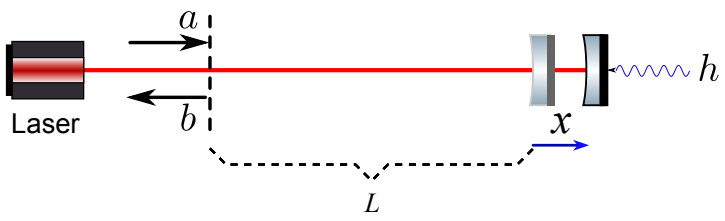

Figure 2.2.: Schematic showing a monochromatic laser beam illuminating a free hanging perfectly reflecting mirror. a and b represent the incident and reflected light field respectively. The mirror has a mechanical displacement x due to the radiation pressure force and the GW tidal force. h is the GW signal. The vertical dashed line shows the reference position and the mirror is a distance L away.

$\mathbf{R}[\phi]$ is a 2×2 rotation matrix and ϕ is known as a rotation angle which corresponds to the phase shift of the carrier field with frequency ω_0 and φ is the phase shift of the modulation sidebands with frequency Ω. When L is set to satisfy $\omega_0 L/c = N\pi$ (N is an integer), the propagation input-output relation can be simplified into:

$$\begin{bmatrix} \hat{b}_1(\Omega) \\ \hat{b}_2(\Omega) \end{bmatrix} = e^{i\varphi} \begin{bmatrix} \hat{a}_1(\Omega) \\ \hat{a}_2(\Omega) \end{bmatrix}. \tag{2.17}$$

Equation (2.17) will be frequently used in the following optical systems for a light field propagation.

2.2.2. Single Mirror

For a free hanging mirror, we have the same expression of the input laser (see Eq. (2.13)):

$$\hat{E}_a(t) = [\hat{a}_1(t) + \Lambda]\cos(\omega_0 t) + \hat{a}_2(t)\sin(\omega_0 t). \tag{2.18}$$

If the laser beam illuminates a mirror (free mass) as shown in Fig. (2.2), the

reflected field can be expressed directly in terms of the incident field as[2]:

$$\hat{E}_b(t) = \hat{E}_a\left(t - 2\tau - 2\frac{\hat{x}(t-\tau)}{c}\right), \tag{2.19}$$

with propagation time $\tau = L/c$ and $\hat{x}$ the displacement of the mirror due to the radiation pressure force and GW tidal force. Again we use $\hat{b}_1(t)$ and $\hat{b}_2(t)$ to define the amplitude and phase quadrature of the reflected field and keep the same format as for the incident field:

$$\hat{E}_b(t) = \left[\hat{b}_1(t) + \Lambda\right]\cos(\omega_0 t) + \hat{b}_2(t)\sin(\omega_0 t). \tag{2.20}$$

Since the displacement of the mirror is much smaller than the wavelength of the light, we can expand Eq. (2.19) in a series of $\omega_0\hat{x}/c$. By ignoring the second and higher orders of the quantum fluctuations in the equation, given $\omega_0 L/c = N\pi$, we obtain $\hat{b}_1(t)$ and $\hat{b}_2(t)$ written in terms of $\hat{a}_1(t)$ and $\hat{a}_2(t)$ as:

$$\hat{b}_1(t) = \hat{a}_1(t - 2\tau), \tag{2.21}$$

$$\hat{b}_2(t) = \hat{a}_2(t - 2\tau) - 2\sqrt{\frac{2I_0}{\hbar\omega_0}}\frac{\omega_0}{c}\hat{x}(t-\tau). \tag{2.22}$$

The equation of motion for the mirror, which is considered as a free mass m, can be written as:

$$m\ddot{\hat{x}}(t) = \hat{F}_{rp}(t) + \frac{1}{2}mL\ddot{h}(t), \tag{2.23}$$

where the radiation pressure force $\hat{F}_{rp}(t)$ depends on the laser power hitting the mirror as (up to the leading order of the fluctuation):

$$\hat{F}_{rp}(t) = \frac{2I_0}{c} + \frac{2I_0}{c}\sqrt{\frac{2\hbar\omega_0}{I_0}}\hat{a}_1(t-\tau). \tag{2.24}$$

Transforming Eqs. (2.22), (2.23)), and (2.24) into the frequency domain, we find:

$$\begin{bmatrix}\hat{b}_1(\Omega)\\ \hat{b}_2(\Omega)\end{bmatrix} = e^{2i\Omega\tau}\begin{bmatrix}1 & 0\\ -\kappa & 1\end{bmatrix}\begin{bmatrix}\hat{a}_1(\Omega)\\ \hat{a}_2(\Omega)\end{bmatrix} + \begin{bmatrix}0\\ e^{i\Omega\tau}\sqrt{2\kappa}\end{bmatrix}\frac{h(\Omega)}{h_{SQL}}, \tag{2.25}$$

[2]We assume the mirror perfectly reflects the input light here. One can also add the reflection coefficient $-\sqrt{R}$, which is not hard to understand in the final result.

with

$$\kappa = \frac{8I_0\omega_0}{mc^2\Omega^2}, \qquad h_{SQL} = \sqrt{\frac{8\hbar}{m\Omega^2L^2}}. \tag{2.26}$$

h_{SQL} is the so-called *Standard Quantum Limit* (SQL) as introduced in Section 1.3.2. The second term in Eq. (2.25) indicates that the GW signal is only present in the phase quadrature $\hat{b}_2(\Omega)$. A homodyne detection with an adjustable detection angle allows us to detect $\hat{b}_2(\Omega)$ only. Given the output $\hat{b}_2(\Omega)$, we usually use the following expression where signal and noise are written separately as:

$$\hat{b}_2(\Omega) = \underbrace{\langle\hat{b}_2(\Omega)\rangle}_{\text{signal}} + \underbrace{\Delta\hat{b}_2(\Omega)}_{\text{noise}}. \tag{2.27}$$

Applying this to Eq. (2.25), we obtain the signal and quantum noise of the single mirror reflection model as:

$$\langle\hat{b}_2(\Omega)\rangle = e^{i\Omega\tau}\sqrt{2\kappa}\frac{h(\Omega)}{h_{SQL}}, \tag{2.28}$$

$$\Delta\hat{b}_2(\Omega) = e^{2i\Omega\tau}\hat{a}_2(\Omega) - e^{2i\Omega\tau}\kappa\hat{a}_1(\Omega), \tag{2.29}$$

where the quantum noise arises from the fluctuations of the input field. Normalising the noise $\Delta\hat{b}_2(\Omega)$ with the GW signal strain $h(\Omega)$, the noise spectral density (NSD) yields:

$$S^h(\Omega) = [\frac{1}{\kappa} + \kappa]\frac{h_{SQL}^2}{2} \geq h_{SQL}^2. \tag{2.30}$$

Figure. 2.3 shows the magnitude of the quantum noise spectrum for a 1 kg mirror with a 1064 nm laser incident. The black dashed line gives the SQL, while the blue and red curves show the quantum NSD of a single mirror reflection with different powers. Figure. 2.3 shows that this model is similar to a simple Michelson interferometer as shown in Section 1.3.2. By changing the input laser power, we achieve different quantum noise behaviours. However, it is not possible to surpass the SQL by only increasing the power.

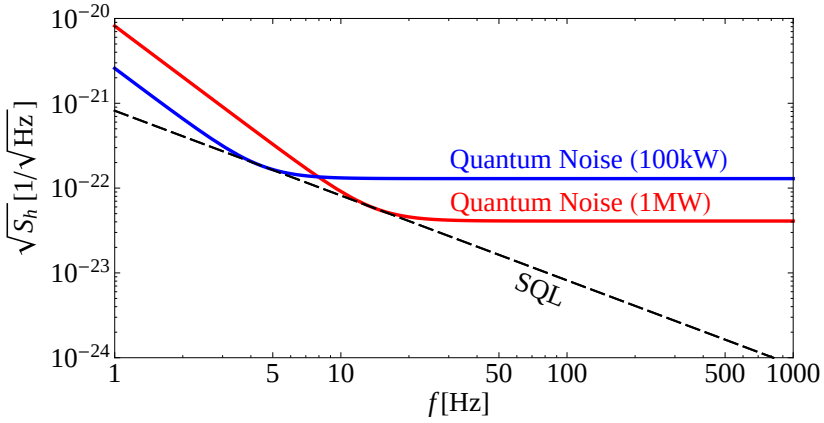

Figure 2.3.: Plot showing the quantum NSD of a single mirror example when a monochromatic laser is injected. The laser wavelength λ is 1064 nm. Two input powers $I_0 = 1\,\text{MW}$ and $I_0 = 100\,\text{kW}$ are considered and labelled in the two curves. The mirror has mass $m = 1\,\text{kg}$ and is displaced $L = 4\,\text{km}$ away from the laser.

2.2.3. Resonant Fabry-Pérot Cavity

A linear Fabry-Pérot cavity consists of two mirrors, inside which the light field is circulating between the two reflection surfaces. We first consider a resonant Fabry-Pérot cavity which is relatively simple as the calculation is simplified by having the propagation distance satisfying $\omega_0 \cdot L/c = N \cdot \pi$. After knowing the quantum noise calculations of a resonant cavity, we can then extend our model into a more common cavity with detuning without too much effort.

Figure. 2.4 shows the schematic of a resonant Fabry-Pérot cavity with a monochromatic laser injection. Compared with Fig. 2.2, an obvious difference is the input mirror (IM) between laser and end mirror (EM). For a lossless model, the IM reflects and transmits light and its reflectivity R and transmissivity T satisfy the equation $R + T + \mathcal{E} = 1$, where $\mathcal{E} = 0$ (see Appendix A). Prior to any consideration of the IM, the expressions of d in terms of c according to Eq. (2.25) yield,

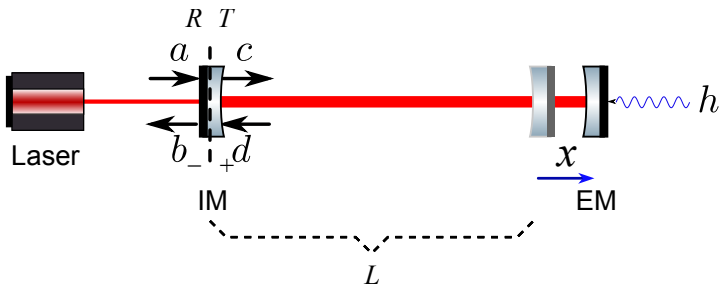

Figure 2.4.: Schematic showing a laser beam injected to a resonant cavity with length L, where $\omega_0 L/c = N \cdot \pi$. a and b represent the incident and reflected light fields respectively; c and d are the inner cavity fields at the input mirror (IM), a partially transmitting mirror with $\sqrt{R} + \sqrt{T} = 1$. In this example, a mechanical displacement x due to the radiation pressure force only happens at the end mirror (EM). The vertical dashed line shows the reference position. Figure adapted from [2].

recalling what we have obtained in Section 2.2.2:

$$\begin{bmatrix} \hat{d}_1(\Omega) \\ \hat{d}_2(\Omega) \end{bmatrix} = e^{2i\Omega\tau} \begin{bmatrix} 1 & 0 \\ -\kappa & 1 \end{bmatrix} \begin{bmatrix} \hat{c}_1(\Omega) \\ \hat{c}_2(\Omega) \end{bmatrix} + \begin{bmatrix} 0 \\ e^{i\Omega\tau}\sqrt{2\kappa} \end{bmatrix} \frac{h(\Omega)}{h_{SQL}}, \tag{2.31}$$

with

$$\kappa = \frac{8 I_c \omega_0}{m c^2 \Omega^2}, \qquad h_{SQL} = \sqrt{\frac{8\hbar}{m\Omega^2 L^2}}. \tag{2.32}$$

We shall note the difference of laser power I_c in κ here. As we have shown in Fig. A.3, the light field builds up inside the cavity when it is on resonance and the magnitude can be approximately valued by $I_c = 4I_0/T$. We rewrite Eq. (2.31) into:

$$\begin{bmatrix} \hat{d}_1(\Omega) \\ \hat{d}_2(\Omega) \end{bmatrix} = \mathbf{M} \cdot \begin{bmatrix} \hat{c}_1(\Omega) \\ \hat{c}_2(\Omega) \end{bmatrix} + \mathbf{D} h(\Omega) \tag{2.33}$$

by using the definitions

$$\mathbf{M} = e^{2i\Omega\tau}\begin{bmatrix} 1 & 0 \\ -\kappa & 1 \end{bmatrix}, \qquad \mathbf{D} = \frac{1}{h_{SQL}}\begin{bmatrix} 0 \\ e^{i\Omega\tau}\sqrt{2\kappa} \end{bmatrix}. \tag{2.34}$$

With obvious conjunction relations between b, c and a, d as shown in the schematic in Fig. 2.4[3], we can directly achieve

$$\begin{bmatrix} \hat{c}_1(\Omega) \\ \hat{c}_2(\Omega) \end{bmatrix} = \sqrt{T}\begin{bmatrix} \hat{a}_1(\Omega) \\ \hat{a}_2(\Omega) \end{bmatrix} + \sqrt{R}\begin{bmatrix} \hat{d}_1(\Omega) \\ \hat{d}_2(\Omega) \end{bmatrix}, \tag{2.35}$$

$$\begin{bmatrix} \hat{b}_1(\Omega) \\ \hat{b}_2(\Omega) \end{bmatrix} = -\sqrt{R}\begin{bmatrix} \hat{a}_1(\Omega) \\ \hat{a}_2(\Omega) \end{bmatrix} + \sqrt{T}\begin{bmatrix} \hat{d}_1(\Omega) \\ \hat{d}_2(\Omega) \end{bmatrix}. \tag{2.36}$$

Combining Eqs. (2.33), (2.35), and (2.36), we obtain the output field $\hat{b}(\Omega)$ in terms of $\hat{a}(\Omega)$ as:

$$\begin{bmatrix} \hat{b}_1(\Omega) \\ \hat{b}_2(\Omega) \end{bmatrix} = \left[-\sqrt{R}\cdot\mathbf{I} + \frac{T\cdot\mathbf{M}}{\mathbf{I}-\sqrt{R}\cdot\mathbf{M}}\right]\cdot\begin{bmatrix} \hat{a}_1(\Omega) \\ \hat{a}_2(\Omega) \end{bmatrix} + \left[\frac{\sqrt{T}\cdot\mathbf{D}}{\mathbf{I}-\sqrt{R}\cdot\mathbf{M}}\right]h(\Omega), \tag{2.37}$$

where $\mathbf{I}$ is a 2×2 *identity matrix*. By substituting $\mathbf{M}$, $\mathbf{D}$, κ and h_{SQL}, above equation is very lengthy and intricate. In order to gain more insight, we shall use reasonable approximations. We assume for a high *finesse* cavity the transmissivity $T \to 0$ and the GW single induced phase value $\Omega\tau = \Omega L/c \to 0$. By making Taylor expansion with respect to these small dimensionless values and only keeping the result with the leading order of the expansion, the simplified equation is:

$$\begin{bmatrix} \hat{b}_1(\Omega) \\ \hat{b}_2(\Omega) \end{bmatrix} = e^{2i\phi}\begin{bmatrix} 1 & 0 \\ -\mathcal{K} & 1 \end{bmatrix}\begin{bmatrix} \hat{a}_1(\Omega) \\ \hat{a}_2(\Omega) \end{bmatrix} + \begin{bmatrix} 0 \\ e^{i\phi}\sqrt{2\mathcal{K}} \end{bmatrix}\frac{h(\Omega)}{h_{SQL}}, \tag{2.38}$$

[3]Note that the '±' signs on all optics indicate the phase changes of the reflection beams: '+' means no phase change while '−' means a 180° phase shift after reflection.

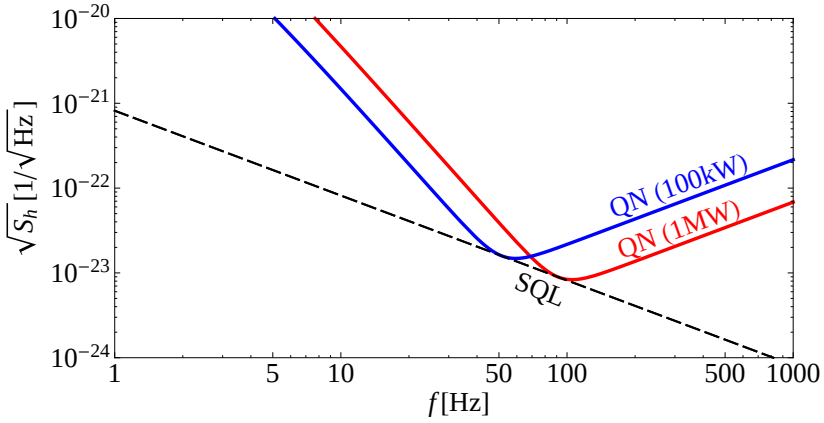

Figure 2.5.: Plot showing the quantum NSD of a resonant cavity when a laser with wavelength $\lambda = 1064\,\text{nm}$ is incident. The IM has transmissivity $T = 0.001$. The EM mass m is 1 kg and the cavity length L is 4 km. The blue curve shows an incident power of 25 W ($I_c = 100\,\text{kW}$) while the red curve gives the result for a 250 W input power ($I_c = 1$ MW).

where

$$\phi = \arctan\left(\frac{\Omega}{\gamma}\right), \qquad \mathcal{K} = \frac{2\gamma\xi_c}{\Omega^2(\Omega^2+\gamma^2)}, \qquad \gamma = \frac{Tc}{4L}, \qquad \xi_c = \frac{4\omega_0 I_c}{mLc}. \tag{2.39}$$

The above equation shows a similar result as the single mirror model (see Eq. (2.25)), the GW signal is only in the phase quadrature $\hat{b}_2(\Omega)$. Following the same analysis of the quantum noise mentioned in Section 2.2.2, the h -normalised quantum NSD of a resonant cavity can be written directly by replacing κ in Eq. (2.30) with $\mathcal{K}$ as:

$$S^h(\Omega) = [\frac{1}{\mathcal{K}} + \mathcal{K}]\frac{h_{SQL}^2}{2} \geq h_{SQL}^2. \tag{2.40}$$

The quantum NSD of a resonant Fabry-Pérot cavity is shown in Fig.2.5. We again consider two values of input power to understand the quantum noise of a resonant cavity. Light powers hitting the EM are kept the same as for the

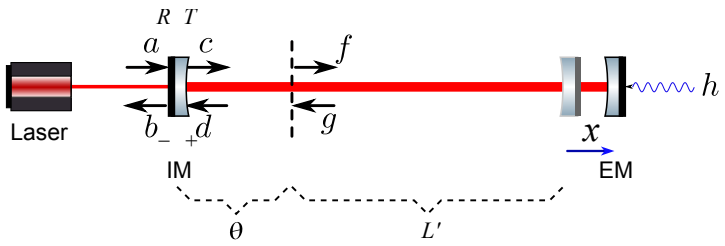

Figure 2.6.: Schematic showing a monochromatic laser beam injected to a detuned cavity, where $\omega_0 \cdot L/c \neq N \cdot \pi$ but $L' = L - \frac{\theta}{\pi}\lambda = N \cdot \pi$. a, b are the incident and reflected light field, c, d are the inner cavity fields at the input mirror (IM), and f, g are the light fields at the reference position. Again the IM is a partial transmitted mirror with $R+T = 1$, and a mechanical displacement x due to the radiation pressure force only happens at the end mirror (EM). The vertical dashed line shows the reference position.

single mirror model: 100 kW and 1 MW. For the same light power on the EM, the input laser power is 4000 times lower with $T = 0.001$. We know that the high-frequency noise, namely shot noise, can be reduced by using high power. Cavities thus offer an effective way to reduce the shot noise. However, without more intelligent correlations between radiation pressure noise and shot noise, the reduction is only a sacrifice of the sensitivity at lower frequencies by increasing the radiation pressure noise, which is clearly shown in Figs. 2.3 and 2.5.

Another important result we can extract from Fig. 2.5 is the narrowed bandwidth of detection, which is determined by $\gamma = Tc/4L$, which does not exist in a non-cavity model (see Fig. 2.3).

2.2.4. Detuned Fabry-Pérot Cavity

After finding the expressions for free space propagation, single mirror reflection and resonant cavity response, an analysis of a detuned cavity as schematically shown in Fig.2.6 becomes straightforward. From the single mirror example (see Eq. (2.25)), the relation between g and f is obvious:

$$\begin{bmatrix} \hat{g}_1(\Omega) \\ \hat{g}_2(\Omega) \end{bmatrix} = \mathbf{M} \cdot \begin{bmatrix} \hat{f}_1(\Omega) \\ \hat{f}_2(\Omega) \end{bmatrix} + \mathbf{D} \cdot h(\Omega), \tag{2.41}$$

where $\mathbf{M}$ and $\mathbf{D}$ are defined in Eq. (2.34). It is easy to see that from c to f and g to d, only a free space propagation *input-output relation* is needed. The input-output relation or *transfer function* (TF), has already been analysed in Section 2.2.1 and can be directly recalled here by defining a rotation angle θ. Since the detuning phase θ is very small, we neglect the phase shift of the free space propagation to obtain the relations:

$$\begin{bmatrix} \hat{d}_1(\Omega) \\ \hat{d}_2(\Omega) \end{bmatrix} = \mathbf{R}[\theta] \begin{bmatrix} \hat{g}_1(\Omega) \\ \hat{g}_2(\Omega) \end{bmatrix}, \qquad \begin{bmatrix} \hat{f}_1(\Omega) \\ \hat{f}_2(\Omega) \end{bmatrix} = \mathbf{R}[\theta] \begin{bmatrix} \hat{c}_1(\Omega) \\ \hat{c}_2(\Omega) \end{bmatrix}. \tag{2.42}$$

Substituting the above equations into Eq. (2.41), we find a relation between d and c as:

$$\begin{bmatrix} \hat{d}_1(\Omega) \\ \hat{d}_2(\Omega) \end{bmatrix} = \mathbf{R}[\theta] \cdot \mathbf{M} \cdot \mathbf{R}[\theta] \cdot \begin{bmatrix} \hat{c}_1(\Omega) \\ \hat{c}_2(\Omega) \end{bmatrix} + \mathbf{R}[\theta] \cdot \mathbf{D} \cdot h(\Omega). \tag{2.43}$$

Defining two new matrices

$$\mathbf{M_d} = \mathbf{R}[\theta] \cdot \mathbf{M} \cdot \mathbf{R}[\theta], \qquad \mathbf{D_d} = \mathbf{R}[\theta] \cdot \mathbf{D}, \tag{2.44}$$

we can then express the field d in terms of c with the same format as in Eq. (2.33)). Following the same procedure, the input-output relation between a and b can be obtained (see Eq. (2.36)):

$$\begin{bmatrix} \hat{b}_1(\Omega) \\ \hat{b}_2(\Omega) \end{bmatrix} = \left[-\sqrt{R}\mathbf{I} + \frac{T \cdot \mathbf{M_d}}{\mathbf{I} - \sqrt{R} \cdot \mathbf{M_d}} \right] \cdot \begin{bmatrix} \hat{a}_1(\Omega) \\ \hat{a}_2(\Omega) \end{bmatrix} + \left[\frac{\sqrt{T} \cdot \mathbf{D_d}}{\mathbf{I} - \sqrt{R} \cdot \mathbf{M_d}} \right] h(\Omega).$$

(2.45)

Once again, after substituting $\mathbf{M_d}$, $\mathbf{D_d}$, κ and h_{SQL}, we use practical approximations of small dimensionless values, including T, θ, and $\Omega \cdot L/c$, and only keep the leading order of the Taylor expansion for this equation. Finally, we reach the simplified equation as:

$$\begin{bmatrix} \hat{b}_1(\Omega) \\ \hat{b}_2(\Omega) \end{bmatrix} = \frac{1}{\mathcal{C}} \left[\mathbf{M}' \cdot \begin{bmatrix} \hat{a}_1(\Omega) \\ \hat{a}_2(\Omega) \end{bmatrix} + \mathbf{D}' \cdot h(\Omega) \right], \tag{2.46}$$

where

$$\mathcal{C} = \Omega^2 \left[(\Omega + i\gamma)^2 - \Delta^2 \right] + \Delta\xi_c, \tag{2.47}$$

$$\mathbf{M}' = \begin{bmatrix} -\Omega^2(\Omega^2 + \gamma^2 - \Delta^2) - \Delta\xi_c & 2\gamma\Delta\Omega^2 \\ -2\gamma\Delta\Omega^2 + 2\gamma\xi_c & -\Omega^2(\Omega^2 + \gamma^2 - \Delta^2) - \Delta\xi_c \end{bmatrix}, \tag{2.48}$$

$$\mathbf{D}' = \begin{bmatrix} \Delta\Omega \\ (-\gamma + i\Omega)\Omega \end{bmatrix} \frac{2\sqrt{\gamma\xi_c}}{h_{SQL}}, \tag{2.49}$$

with detuning frequency $\Delta = \theta/\tau$. γ and ξ_c are as defined for a resonant cavity model, which have been defined in Eq. (2.39).

Unlike the resonant cavity case, Eq. (2.49) tells us that the GW signal does not possess one unique quadrature anymore. In this case, we can perform a homodyne detection which allows a detection of a linear combination of both output quadratures. The output then can be described by

$$\hat{b}_\zeta(\Omega) = \hat{b}_1(\Omega)\cos\zeta + \hat{b}_2(\Omega)\sin\zeta, \tag{2.50}$$

where ζ is the homodyne detection angle. For such an output, the quantum NSD is

$$S_h(\Omega) = \frac{(\cos\zeta, \sin\zeta)\mathbf{M}'\mathbf{M}'^{\dagger}(\cos\zeta, \sin\zeta)^T}{|D'_1\cos\zeta + D'_2\sin\zeta|^2}, \tag{2.51}$$

where D'_1 and D'_2 are the elements of the matrix $\mathbf{D}'$.

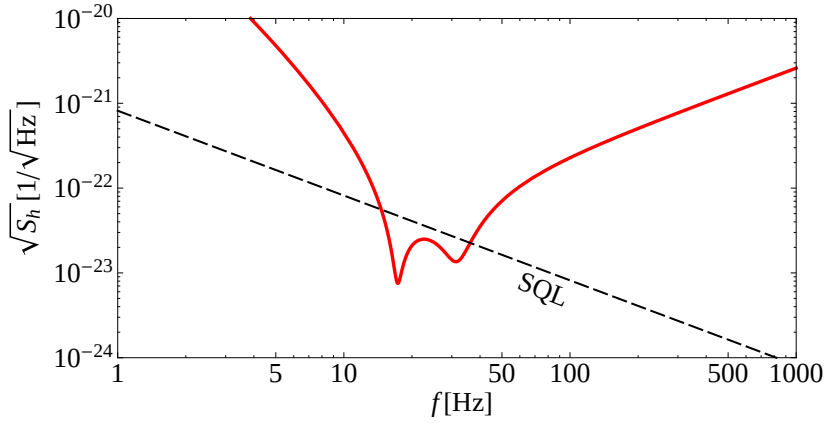

Figure 2.7.: Plot showing the quantum NSD of a detuned cavity when a laser with wavelength $\lambda = 1064\,\text{nm}$ and $I_0 = 25\,\text{W}$ is incident. The IM has transmissivity $T = 0.001$. The EM mass m is 1 kg and the cavity length L is 4 km. The detuning phase θ is 0.003 and the homodyne detection angle $\zeta = \pi/2$.

Not surprisingly, when ζ is chosen as $\pi/2$ and detuning frequency $\Delta = 0$, the detuned cavity recovers the resonant cavity model, which has been investigated in Section 2.2.3.

The NSD of a detuned cavity with the detuning phase $\theta = 0.003$ creates two dips as shown in Fig. 2.7, which beats the SQL for a certain frequency range. The frequencies of the two sensitivity dips are determined by the resonances induced by the mechanical mode and optical mode [53], which can also be seen from Eqs. (2.46)-(2.49),

2.3. A General Interpretation—Block Diagrams

When a system consists of several principal parts and each of them has a well defined input-output relation (or *transfer function* (TF)), it can be conveniently

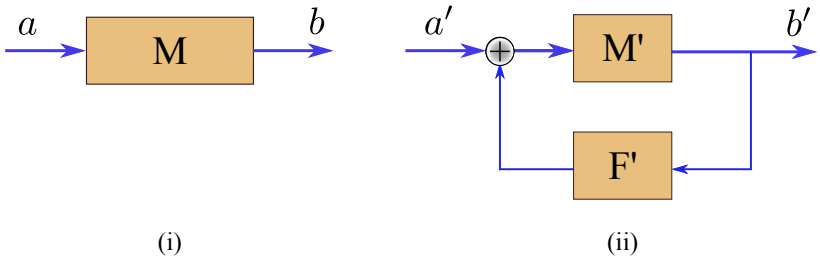

Figure 2.8.: Block diagrams showing a simple system with (i) open loop and (ii) closed loop. (i) shows a linear system with a and b the input and output variables. $\mathbf{M}$ is the transfer function (TF) of the block. (ii) is a close system including a feedback function $\mathbf{F}'$ which together with the major system $\mathbf{M}'$ forms a close loop. Each block represents a linear subsystem with specified TF, here denoted as $\mathbf{M}$, $\mathbf{M}'$, and $\mathbf{F}'$.

described by using block diagrams, particularly when there is a closed loop. In such a diagram, each block represents one principal subsystem and these blocks are connected by arrows (specifying the direction of signal flow). In order to achieve the quantum NSD, the input-output relation of an optical setup needs to be specified [54]. Therefore, the implementation of block diagrams promises to simplify many complicated calculations. The idea of using block diagram has already been demonstrated in [2]. Here we will complement the details of the principle.

The block diagrams in Fig. 2.8 illustrate a general open loop system and a closed loop system, respectively. The left-hand diagram shows an open system with only one block $\mathbf{M}$ which converts any input variable or function, such as a into an output variable or function b. The only difference in the righthand diagram is a feedback block $\mathbf{F}'$, which feeds the output signal back into the input port and forms a closed loop.

It is useful to introduce two important parameters for a system which is either

open or closed. For an open one, it is called *open loop transfer function* and defined as $\mathbf{M}_{\mathrm{olt}} = \mathbf{M}$ while for a closed system it is called *closed loop transfer function* and is defined as $\mathbf{M}'_{\mathrm{clt}} = [\mathbf{I} - \mathbf{M}'\mathbf{F}']^{-1}$, with $\mathbf{I}$ being an identity matrix of size N same as that of $\mathbf{M}'\mathbf{F}'$.

Depending on the input signal added to an open or closed loop, any input-output relation can be directly written down if $\mathbf{M}_{\mathrm{olt}}$ and $\mathbf{M}_{\mathrm{clt}}$ are known. For the two simple systems in Fig. 2.8, their input-output relations are:

$$\frac{b}{a} = \mathbf{M}_{\mathrm{olt}} = \mathbf{M}, \qquad \frac{b'}{a'} = \mathbf{M}' \cdot \mathbf{M}'_{\mathrm{clt}} = \frac{\mathbf{M}'}{\mathbf{I} - \mathbf{M}'\mathbf{F}'}, \tag{2.52}$$

where $\mathbf{M}$, $\mathbf{M}'$, and $\mathbf{F}'$ can be any transfer function of any system, e.g., for our purpose, being a free propagating space, a single mirror or even a combined function of several sub-principal components such as spaces plus mirrors.

Basically, $\mathbf{M}_{\mathrm{olt}} = \mathbf{M}$ and $\mathbf{M}_{\mathrm{clt}} = [\mathbf{I} - \mathbf{F} \cdot \mathbf{M}]^{-1}$ are always true for a linear and stationary system which contains a principal transfer function $\mathbf{M}$ and a feedback transfer function $\mathbf{F}$. In the following section, we will illustrate optical systems using block diagrams. In order to have a more intuitive understanding, we will first present and compare the diagrams of the four examples we have discussed in Section 2.2 and then come back to summarise a generic interpretation which can be easily recalled in the remainder of this work.

In fact, all results we have presented in Section 2.2 are based on the input-output relation calculations. Therefore, it should be no surprise that all the examples in the above section can be schematically illustrated by block diagrams. We start our considerations with the free space propagation and the single mirror reflection, which are simpler compared to cavity models, as they do not involve a feedback loop. Based on the schematics, their corresponding block diagrams are shown in Fig. 2.9.

With the symbols indicated in Fig. 2.9, according to Eq. (2.52), the outputs can

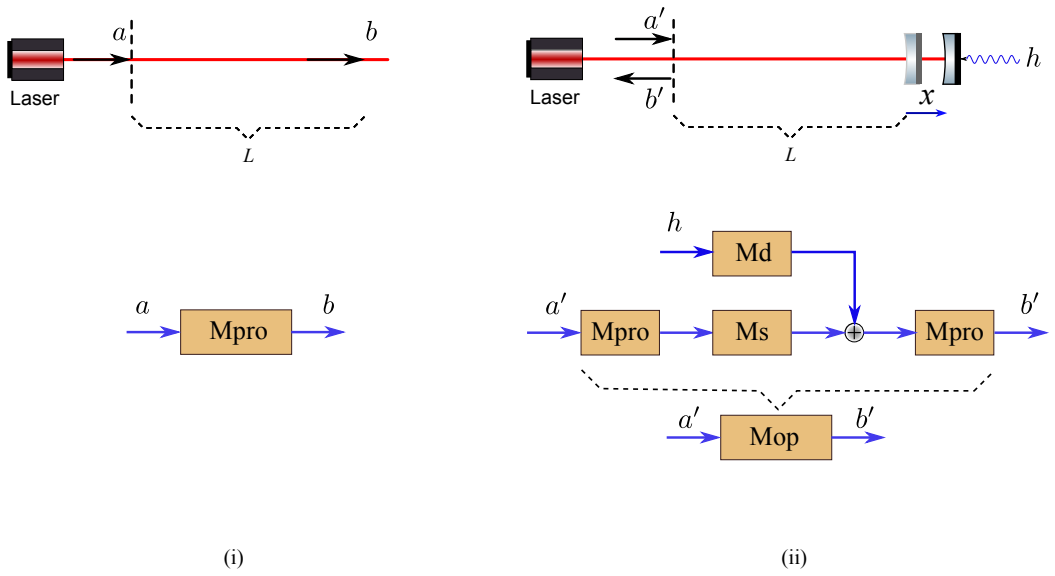

Figure 2.9.: Diagram showing the schematics and corresponding block diagrams of a laser beam (i) propagating in a free space and (ii) reflected by a single free hanging perfect mirror. $\mathbf{M_{pro}}$ is the propagating TF, **Ms** is the TF of a perfectly reflecting mirror, which includes an EM mechanical response and $\mathbf{M_{op}}$ is the combining TF, which includes the light field propagations $\mathbf{M_{pro}}$, and reflection **Ms**. Figure adapted from [2].

be written as:

$$\begin{bmatrix} b_1 \\ b_2 \end{bmatrix} = \mathbf{M_{pro}} \cdot \begin{bmatrix} a_1 \\ a_2 \end{bmatrix}, \tag{2.53}$$

$$\begin{bmatrix} b_1' \\ b_2' \end{bmatrix} = [\mathbf{M_{pro}} \cdot \mathbf{M_s} \cdot \mathbf{M_{pro}}] \cdot \begin{bmatrix} a_1' \\ a_2' \end{bmatrix} + \mathbf{M_d} \cdot \mathbf{M_{pro}} \cdot h \tag{2.54}$$

Matching the above equations with the precise output fields of a free space propagation and a single mirror reflection shown in Eqs. (2.16) and (2.25), we then obtain the transfer functions of blocks as:

$$\mathbf{M_{pro}} = e^{i\varphi}\mathbf{R}[\phi], \qquad \mathbf{M_s} = \begin{bmatrix} 1 & 0 \\ -\kappa & 1 \end{bmatrix}, \qquad \mathbf{M_d} = \begin{bmatrix} 0 \\ \frac{\sqrt{2\kappa}}{h_{SQL}} \end{bmatrix}. \tag{2.55}$$

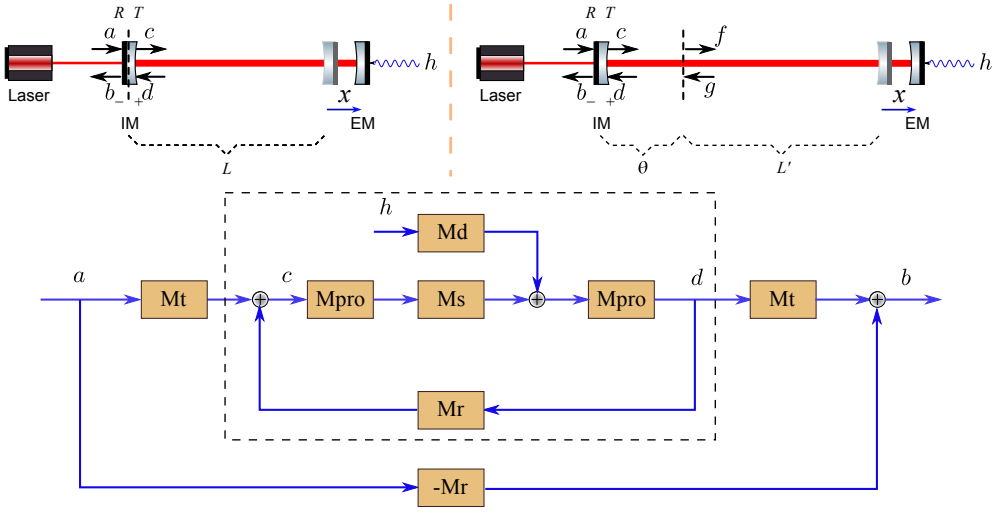

Figure 2.10.: Diagram showing the schematics of a resonant and detuned cavity and their uniform block diagram. a and b are the input and output variables, respectively. c and d are the light fields at the inner side of the input mirror. $\mathbf{M_r}$ and $\mathbf{M_t}$ are the reflection and transmission TF of the IM. A closed loop is shown in the dashed box which includes the TF of the EM reflection $\mathbf{M_r}$, the TF of the EM mechanical response $\mathbf{M_s}$, and the TF of the propagations $\mathbf{M_{pro}}$.

If L also satisfies $\omega_0 L/c = N\pi$, we have $\mathbf{M_{pro}}$ equal to $\exp(i\Omega L/c)$. Substituting each block TF into Eqs. (2.53) and (2.54), we achieve the input-output relations of a light field propagating a distance L and a light field reflected by a free hanging perfect mirror at a distance of L as:

$$\begin{bmatrix} b_1 \\ b_2 \end{bmatrix} = e^{i\Omega\tau} \begin{bmatrix} a_1 \\ a_2 \end{bmatrix}, \tag{2.56}$$

$$\begin{bmatrix} b_1' \\ b_2' \end{bmatrix} = e^{2i\Omega\tau} \begin{bmatrix} 1 & 0 \\ -\kappa & 1 \end{bmatrix} \begin{bmatrix} a_1' \\ a_2' \end{bmatrix} + e^{i\Omega\tau} \begin{bmatrix} 0 \\ \frac{\sqrt{2\kappa}}{h_{SQL}} \end{bmatrix} h, \tag{2.57}$$

with $\tau = L/c$. These input-output relations are reproduced (see Eqs. (2.16) and (2.25)). Based on the above TFs, we continue the analysis of a Fabry-Pérot cavity.

A cavity consists of two mirrors with the EM having the same physical behaviour of the single mirror example. Hence, a new definition of the block $\mathbf{M_{op}} = \mathbf{M_{pro}} \cdot \mathbf{M_s} \cdot \mathbf{M_{pro}}$ as shown in Fig.2.9(ii) will facilitate the calculations. Following a similar process, we have a general block diagram of an arbitrary cavity, either resonant or detuned, as shown in Fig.2.10. Note that a cavity (either resonant or detuned) can be schematically described by the same diagram and the only difference is the propagating matrix $\mathbf{M_{pro}}$ due to the different propagating lengths, which will be discussed in detail later.

According to previous calculations, we immediately obtain the reflection and transmission TFs:

$$\mathbf{M_r} = \sqrt{R}\mathbf{I}, \qquad \mathbf{M_t} = \sqrt{T}\mathbf{I}. \tag{2.58}$$

Due to the reflection of the IM, field d gets fed back to c and forms a closed loop for the signal flow as shown in Fig. 2.10 (framed by a dashed box). Following the definition in Eq. (2.52), the closed loop TF of a cavity can be achieved as:

$$\mathbf{M_{cav}} = \frac{1}{\mathbf{I} - \mathbf{M_r}\mathbf{M_{op}}} = \frac{1}{\mathbf{I} - \sqrt{R}\mathbf{M_{op}}}. \tag{2.59}$$

With all of the independent TFs and the closed loop TF, the output b can be written down directly following the signal flow as[4]:

$$b = -\mathbf{M_r}a + \mathbf{M_{cav}}\mathbf{M_t}\mathbf{M_{op}}\mathbf{M_t}a + \mathbf{M_{cav}}\mathbf{M_t}\mathbf{M_{pro}}\mathbf{M_d}h. \tag{2.60}$$

Substituting Eq. (2.58) into the above equation, the output quadratures, in the quadrature format, become:

$$\begin{bmatrix} \hat{b}_1(\Omega) \\ \hat{b}_2(\Omega) \end{bmatrix} = \left[-\sqrt{R}\mathbf{I} + \frac{T\mathbf{M_{op}}}{\mathbf{I} - \sqrt{R}\mathbf{M_{op}}}\right] \begin{bmatrix} \hat{a}_1(\Omega) \\ \hat{a}_2(\Omega) \end{bmatrix} + \left[\frac{\sqrt{T}\mathbf{M_{pro}}\mathbf{M_d}}{\mathbf{I} - \sqrt{R}\mathbf{M_{op}}}\right] h(\Omega), \tag{2.61}$$

which is the general expression of the quadrature input-output relation of a cavity. By inserting distinctive propagation matrices of a resonant cavity and a detuned

[4]Be aware of the order of the matrices; they should follow the flow direction of the signals.

cavity, the input-output relations can be obtained with

$$\mathbf{M}^{\mathbf{re}}_{\mathbf{pro}} = e^{i\Omega\tau}, \qquad \mathbf{M}^{\mathbf{de}}_{\mathbf{pro}} = e^{i\Omega\tau}\mathbf{R}[\theta]. \tag{2.62}$$

We have found that the outputs calculated using the block diagrams match those in the previous calculations as presented in Eqs. (2.37) and (2.46).

Since the case of a resonant cavity will be vastly used in the following, we want to specify the exact analytical expression of Eq. (2.37) or Eq. (2.38):

$$\begin{aligned}
\begin{bmatrix} \hat{b}_1(\Omega) \\ \hat{b}_2(\Omega) \end{bmatrix} =& \begin{bmatrix} \frac{e^{i\Omega\tau}-e^{-i\Omega\tau}\sqrt{R_i}}{e^{-i\Omega\tau}-e^{i\Omega\tau}\sqrt{R_i}} & 0 \\ \frac{T_i\kappa}{(e^{-i\Omega\tau}-e^{i\Omega\tau}\sqrt{R_i})^2} & \frac{e^{i\Omega\tau}-e^{-i\Omega\tau}\sqrt{R_i}}{e^{-i\Omega\tau}-e^{i\Omega\tau}\sqrt{R_i}} \end{bmatrix} \begin{bmatrix} \hat{a}_1(\Omega) \\ \hat{a}_2(\Omega) \end{bmatrix} \\
&+ \begin{bmatrix} 0 \\ \frac{\sqrt{T_i}}{e^{-i\Omega\tau}-e^{i\Omega\tau}\sqrt{R_i}}\frac{\sqrt{2\kappa}}{h_{SQL}} \end{bmatrix} h(\Omega) \\
=& e^{2i\phi_{cav}} \begin{bmatrix} 1 & 0 \\ -\kappa_{cav} & 1 \end{bmatrix} \begin{bmatrix} \hat{a}_1(\Omega) \\ \hat{a}_2(\Omega) \end{bmatrix} + e^{i\phi_{cav}}\frac{\sqrt{2\kappa_{cav}}}{h_{SQL}} \begin{bmatrix} 0 \\ 1 \end{bmatrix} h(\Omega),
\end{aligned} \tag{2.63}$$

with

$$\phi_{\text{cav}} = \arctan\left(\frac{1+\sqrt{R_i}}{1-\sqrt{R_i}}\tan\Omega\tau\right), \tag{2.64}$$

$$\kappa_{\text{cav}} = \frac{T_i\kappa}{1-2\sqrt{R_i}\cos(2\Omega\tau)+R_i}. \tag{2.65}$$

Note that κ_{cav} can be approximated by $\mathcal{K}$ (see Eq. (2.38)), given that the cavity IM transmissivity is small, which is true for the GW detector. We thus will make no distinction between them in the rest of this thesis.

So far, we have not considered any optical losses. Previous work [54, 58, 64] taught us that additional vacuum fluctuations can simultaneously enter the optical system at any open port where light fields are escaping from the system; this is known as optical loss. We will further consider our models with optical losses taken into account. Using the resonant cavity as an example, we will develop a generic block diagram which is suitable for the loss analysis.

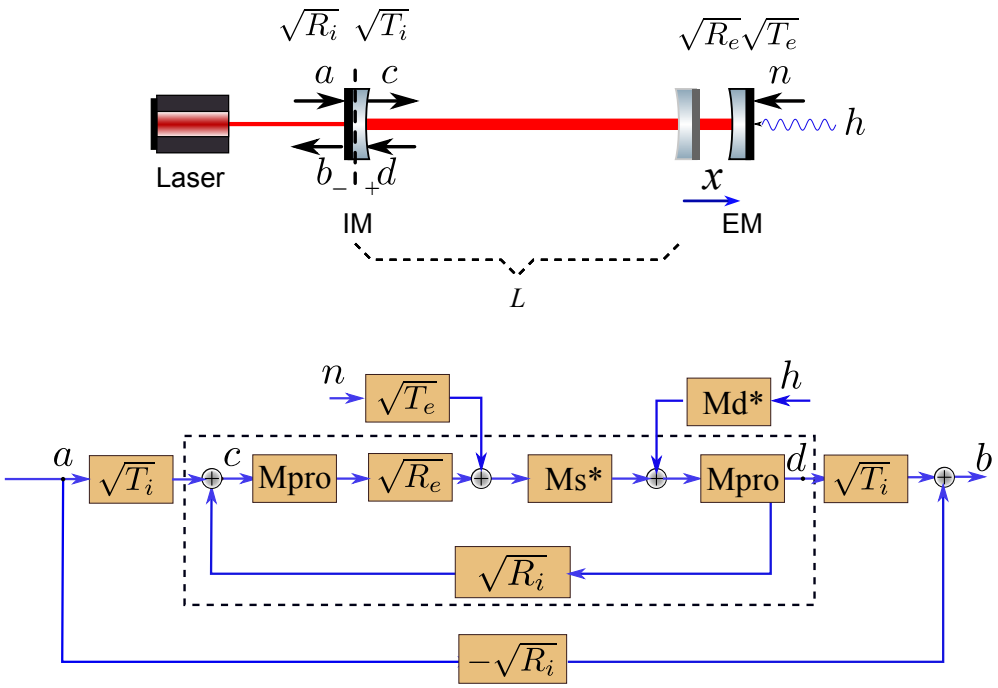

Figure 2.11.: Diagram showing the schematic of a lossy resonant cavity or detuned cavity and their uniform block diagram. All notations are similar to those shown in Fig. 2.10. TFs with '*' include optical lossy effect and they have the same format as the lossless expressions (see Eqs. (2.66) and(2.67)). n means the optical losses induced vacuum fluctuations. Figure taken from [2].

A schematic and its corresponding block diagram of a lossy cavity are shown in Fig. 2.11, where cavity losses are grouped into the transmission of the EM and are denoted as n. We can write the input-output relation of a lossy cavity as

$$\begin{aligned}\begin{bmatrix}\hat{b}_1(\Omega)\\ \hat{b}_2(\Omega)\end{bmatrix} &= \left[-\sqrt{R_i}\cdot\mathbf{I} + T_i\sqrt{R_e}\cdot\mathbf{M}^*_{\mathbf{cav}}\cdot\mathbf{M}^*_{\mathbf{op}}\right]\cdot\begin{bmatrix}\hat{a}_1(\Omega)\\ \hat{a}_2(\Omega)\end{bmatrix}\\ &+\left[\sqrt{T_i}\sqrt{R_e}\cdot\mathbf{M}^*_{\mathbf{cav}}\cdot\mathbf{M}_{\mathbf{pro}}\cdot\mathbf{M}^*_{\mathbf{d}}\right]h(\Omega),\\ &\left[\sqrt{T_i}\sqrt{T_e}\cdot\mathbf{M}^*_{\mathbf{cav}}\cdot\mathbf{M}^*_{\mathbf{s}}\cdot\mathbf{M}_{\mathbf{pro}}\right]\cdot\begin{bmatrix}\hat{n}_1(\Omega)\\ \hat{n}_2(\Omega)\end{bmatrix},\end{aligned} \tag{2.66}$$

with

$$\mathbf{M}^*_{\rm cav} = \frac{1}{\mathbf{I} - \sqrt{R_i R_e}\cdot \mathbf{M}^*_{\rm op}}.$$

$\mathbf{M}^*_{\mathbf{s}}$, $\mathbf{M}^*_{\mathbf{op}}$, $\mathbf{M}^*_{\mathbf{d}}$ have the same format as in the lossless expressions in Eq. (2.55), but replacing κ by

$$\kappa^* = \sqrt{R_e}\frac{8I^*\omega_0}{mc^2\Omega^2}, \tag{2.67}$$

due to the EM loss, results in a lower laser power circulating inside the cavity. We assume the cavity loss is far smaller than 1, $T_e \ll 1$. This enables an approximation to keep only the leading order of $\sqrt{T_e}$ in the input-output relation. For a resonant lossy cavity, we thus get the same format input-output relation as in Eq. (2.63)

$$\begin{aligned}\begin{bmatrix}\hat{b}_1(\Omega)\\ \hat{b}_2(\Omega)\end{bmatrix} =& e^{2i\phi_{cav}}\begin{bmatrix}1 & 0\\ -\kappa^*_{cav} & 1\end{bmatrix}\begin{bmatrix}\hat{a}_1(\Omega)\\ \hat{a}_2(\Omega)\end{bmatrix}\\ &+ e^{i\phi_{cav}}\frac{\sqrt{2\kappa^*_{cav}}}{h_{SQL}}\begin{bmatrix}0\\ 1\end{bmatrix}h(\Omega)\\ &\sqrt{T_e}e^{i\phi_{cav}}\sqrt{\frac{\kappa^*_{cav}}{\kappa^*}}\begin{bmatrix}1 & 0\\ -\sqrt{\frac{\kappa^*_{cav}}{T_i}}e^{i\phi_{cav}-i\Omega\tau} & 1\end{bmatrix}\begin{bmatrix}\hat{n}_1(\Omega)\\ \hat{n}_2(\Omega)\end{bmatrix}.\end{aligned} \tag{2.68}$$

We turn this input-output relation into

$$\begin{bmatrix}\hat{b}_1(\Omega)\\ \hat{b}_2(\Omega)\end{bmatrix} = \mathbf{M}_{\rm cav}\begin{bmatrix}\hat{a}_1(\Omega)\\ \hat{a}_2(\Omega)\end{bmatrix} + \mathbf{H}_{\rm cav}h(\Omega) + \mathbf{N}_{\rm cav}\begin{bmatrix}\hat{n}_1(\Omega)\\ \hat{n}_2(\Omega)\end{bmatrix}, \tag{2.69}$$

where $\mathbf{M}_{\rm cav}$, $\mathbf{H}_{\rm cav}$ and $\mathbf{N}_{\rm cav}$ correspond to the matrices in Eq. (2.68). This gives the general input-output relation expression of a lossy resonant cavity. We further simplify such a cavity into a new block diagram as shown in Fig. 2.12, which can be employed for any optical system containing a resonant cavity (i.e., interferometer arm cavities).

From those representative examples, we can conclude that block diagrams provide an effective method in calculating the input-output relation of a light field trav-

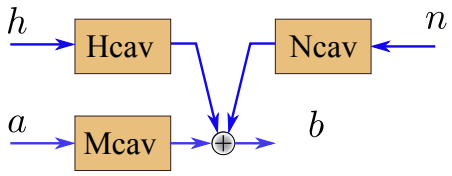

Figure 2.12.: A block diagram of a general lossy resonant optical cavity. The TFs are defined in Eqs. (2.68) and (2.69). Figure taken from [2].

elling through an optical system. More generally, all of the quadrature equations can be written as:

$$\begin{bmatrix} \hat{b}_1(\Omega) \\ \hat{b}_2(\Omega) \end{bmatrix} = \begin{bmatrix} M_{11} & M_{12} \\ M_{21} & M_{22} \end{bmatrix} \begin{bmatrix} \hat{a}_1(\Omega) \\ \hat{a}_2(\Omega) \end{bmatrix} + \begin{bmatrix} D_1 \\ D_2 \end{bmatrix} h(\Omega) + \sum_{i=\mathrm{LP}} \begin{bmatrix} N_{11}^{\mathrm{LP}} & N_{12}^{\mathrm{LP}} \\ N_{21}^{\mathrm{LP}} & N_{22}^{\mathrm{LP}} \end{bmatrix} \begin{bmatrix} \hat{n}_1^{\mathrm{LP}}(\Omega) \\ \hat{n}_2^{\mathrm{LP}}(\Omega) \end{bmatrix}, \tag{2.70}$$

where each of the transfer matrix elements is only determined by the specific optical layout. The first term is the fluctuations due to the light field (laser beam), the second term is the GW signal and the third term is the vacuum fluctuations due to optical losses from different lossy ports (LP), i.e., $\hat{n}^{\mathrm{arm}}$. With the output amplitude and phase quadratures, we can take a measurement of the mixed output quadratures which reads:

$$\hat{b}_\zeta(\Omega) = \hat{b}_1(\Omega)\cos\zeta + \hat{b}_2(\Omega)\sin\zeta, \tag{2.71}$$

enabled by a homodyne detection with detection angle ζ. Correspondingly, the h-normalised quantum NSD of this measurement is:

$$S_h(\Omega) = \frac{(\cos\zeta, \sin\zeta)\cdot \mathbf{M}\cdot(\mathbf{S_a} + \sum \mathbf{S_n})\cdot \mathbf{M}^\dagger \cdot (\cos\zeta, \sin\zeta)^T}{|D_1\cos\zeta + D_2\sin\zeta|^2}, \tag{2.72}$$

with $\mathbf{S_{a,n}}$ being the NSD matrix. The NSD matrix $\mathbf{S_n}$ thus is always an identity matrix. $\mathbf{S_a}$ is the NSD matrix induced by the laser fluctuations and the elements are the corresponding NSD defined in [54] as

$$\mathbf{S_a}(\Omega) = \begin{bmatrix} S_{a_1a_1}(\Omega) & S_{a_1a_2}(\Omega) \\ S_{a_2a_1}(\Omega) & S_{a_2a_2}(\Omega) \end{bmatrix}, \tag{2.73}$$

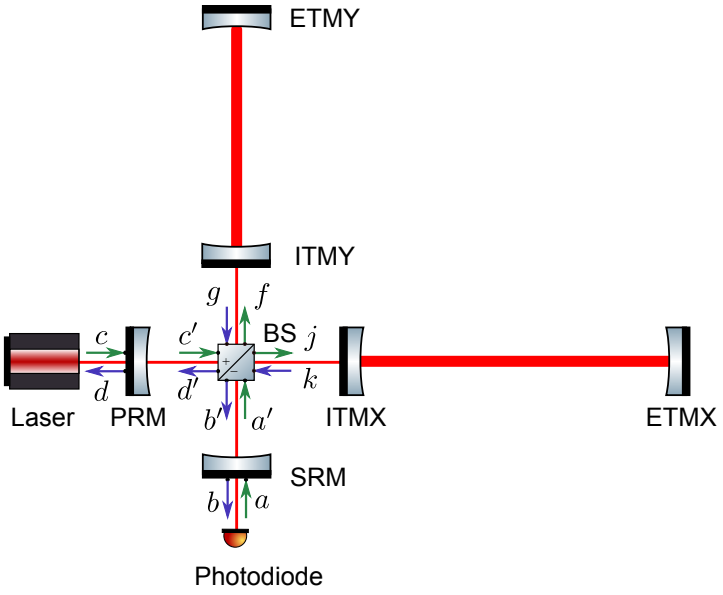

Figure 2.13.: Schematic of a simplified Advanced LIGO configuration. It is based on a dual-recycled Michelson interferometer and with arm cavities (see Section 1.2.1). Green and blue arrows specify the corresponding input and output electric fields at different ports.

with $\pi S_{a_i a_j}(\Omega)\delta(\Omega - \Omega') = \langle \mathrm{in}|\mathrm{a_i}(\Omega)\mathrm{a_j^\dagger}(\Omega')|\mathrm{in}\rangle_{\mathrm{sym}}$, i.e., if $|\mathrm{in}\rangle$ is a vacuum input $|0\rangle$. Then $S_{a_1 a_1}(\Omega) = S_{a_2 a_2}(\Omega) = 1$ and $S_{a_1 a_2}(\Omega) = S_{a_2 a_1}(\Omega) = 0$ lead to an identity matrix $\mathbf{S}_a = \mathbf{S}_{\mathrm{vac}} = \mathbf{I}$. A squeezed vacuum input results in a different NSD matrix $\mathbf{S}_{\mathrm{a}}$ which will be discussed in Chapter 3.

2.4. Quantum Noise of Advanced LIGO

Using the preparations performed in previous sections, we can now calculate the quantum noise of an advanced GW interferometer, such as Advanced LIGO, which includes arm cavities and dual-recycling cavities (with both *power recycling mirror* (PRM) and *signal recycling mirror* (SRM)) as shown in Fig. 2.13 (also see Fig. 1.4).

2.4.1. Lossless Case

We start our investigation with a perfect lossless model. In a Michelson interferometer, a 50:50 beam splitter (BS) equally splits a laser beam into two. The beams reflected by the ETMs and then again combined at the BS. Depending on the length of each arm, constructive and destructive interference takes place at the bright and dark port. Conventionally, for a 50:50 BS, the conjunction relations between four ports obey:

$$\hat{f} = \frac{\hat{c}' + \hat{a}'}{\sqrt{2}}, \qquad \hat{j} = \frac{\hat{c}' - \hat{a}'}{\sqrt{2}}, \qquad \hat{d}' = \frac{\hat{g} + \hat{k}}{\sqrt{2}}, \qquad \hat{b}' = \frac{\hat{g} - \hat{k}}{\sqrt{2}}. \tag{2.74}$$

In reality, the PRM forms resonant cavities with the arm cavities to increase the laser power circulating in the interferometer and in turn in the arm cavities, which immediately leads us to the direct relation between field c' and c as:

$$\hat{E}_{c'}(t) = \left[\hat{c}_1(t) + \sqrt{\frac{2I}{\hbar\omega_0}}\right]\cos(\omega_0 t) + \hat{c}_2(t)\sin(\omega_0 t), \tag{2.75}$$

where $I = I_0\mathcal{F}_{\mathrm{PRC}}/\pi$ with $\mathcal{F}_{\mathrm{PRC}}$ being the finesse of the power recycling cavity (PRC) (see Eq. (A.8)). Due to the relatively small cavity lengths, we ignore the propagation phase shift.

We know that arm cavities are also on resonance. We can recall the input-output relation in Eq. (2.63) and find

$$\begin{bmatrix} \hat{g}_1(\Omega) \\ \hat{g}_2(\Omega) \end{bmatrix} = e^{2i\Omega\tau}\begin{bmatrix} 1 & 0 \\ -\kappa_{\mathrm{cav}} & 1 \end{bmatrix}\begin{bmatrix} \hat{f}_1(\Omega) \\ \hat{f}_2(\Omega) \end{bmatrix} + \begin{bmatrix} 0 \\ e^{i\Omega\tau}\sqrt{2\kappa_{\mathrm{cav}}} \end{bmatrix}\frac{h_1(\Omega)}{h_{SQL}}, \tag{2.76}$$

$$\begin{bmatrix} \hat{k}_1(\Omega) \\ \hat{k}_2(\Omega) \end{bmatrix} = e^{2i\Omega\tau}\begin{bmatrix} 1 & 0 \\ -\kappa_{\mathrm{cav}} & 1 \end{bmatrix}\begin{bmatrix} \hat{j}_1(\Omega) \\ \hat{j}_2(\Omega) \end{bmatrix} + \begin{bmatrix} 0 \\ e^{i\Omega\tau}\sqrt{2\kappa_{\mathrm{cav}}} \end{bmatrix}\frac{h_2(\Omega)}{h_{SQL}}. \tag{2.77}$$

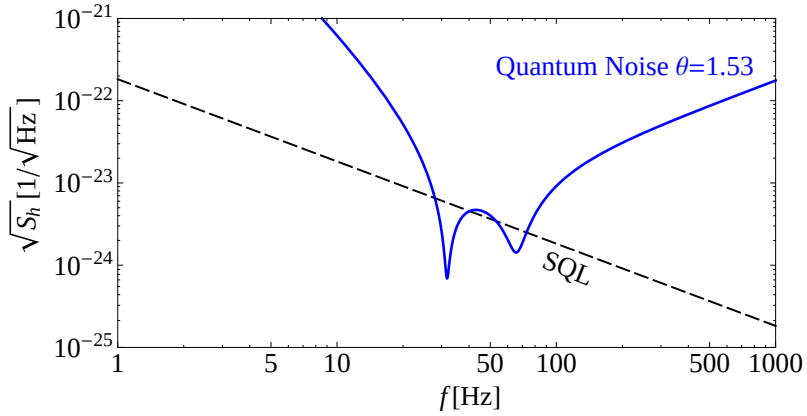

Figure 2.14.: Plot showing the quantum NSD of Advanced LIGO when only detecting the phase quadrature ($\zeta = \pi/2$). The SRM has a reflectivity $R_s = 0.99$ and a detuned phase $\theta = 1.53$. The black dashed line is the SQL. Sensitivity peaks are chosen around 50 Hz.

Our aim is still the input-output relation, namely the relation between b and a, or b' and a'. With Eq. (2.74), we can derive the output field b' by subtracting Eq. (2.76) from Eq. (2.77) which gives

$$\begin{bmatrix} \hat{b'}_1(\Omega) \\ \hat{b'}_2(\Omega) \end{bmatrix} = e^{2i\Omega\tau} \begin{bmatrix} 1 & 0 \\ -\kappa_{\rm cav} & 1 \end{bmatrix} \begin{bmatrix} \hat{a'}_1(\Omega) \\ \hat{a'}_2(\Omega) \end{bmatrix} + \frac{1}{\sqrt{2}} \begin{bmatrix} 0 \\ e^{i\Omega\tau}\sqrt{2\kappa_{\rm cav}} \end{bmatrix} \frac{h(\Omega)}{h_{SQL}}, \quad (2.78)$$

where $h(\Omega) = [h_1(\Omega) - h_2(\Omega)]$ is the definition of the differential GW strains.

The relation between b' and a' gives the input-output relation of a GW interferometer without a SRM. The last step is to consider the SRM forming a detuned cavity with the arm cavities. From [53] and [62] we know that the expression is tremendously complicated. Thus in this section, we attempt to use the approximate interpretation introduced in [65], which maps the three mirror cavities into two mirrors. The idea is based on the assumption that the length of the cavity formed by the SRM and the ITM is negligible compared to the length of the arm cavity. The SRM and the ITM are combined to give one effective mirror which adjusts the linewidth and detuned phase of a detuned cavity (see Eq. (2.46)) as

follows:

$$\Delta_{\mathrm{eff}} = \frac{2\sqrt{R_s}\gamma_i \sin 2\theta}{1 + R_s + 2\sqrt{R_s}\cos 2\theta}, \qquad \gamma_{\mathrm{eff}} = \frac{(1 - R_s)\gamma_i}{1 + R_s + 2\sqrt{R_s}\cos 2\theta}. \tag{2.79}$$

Consequently, the quantum NSD can be calculated according to Eq. (2.51) for a homodyne detection angle of $\zeta = \pi/2$ as:

$$S_h(\Omega) = \frac{4\gamma_{\mathrm{eff}}(\xi_c + \Delta_{\mathrm{eff}}\Omega^2)^2 + \left[\Delta_{\mathrm{eff}}\xi_c + \Omega^2(\gamma_{\mathrm{eff}}^2 - \Delta_{\mathrm{eff}}^2 + \Omega^2)\right]^2}{4\gamma_{\mathrm{eff}}\xi_c\Omega^2(\gamma_{\mathrm{eff}}^2 + \Omega^2)} h_{\mathrm{SQL}}^2. \tag{2.80}$$

Figure 2.14 illustrates how the SQL can be surpassed for a certain frequency range, e.g., 50 Hz, by applying a SRM. This is because the GW signals have been coherently fed back to the interferometer and the signal-recycled interferometer creates an optical spring [62], which modifies the dynamics of the test masses.

2.4.2. With Optical Losses

An ideal lossless model is not practical for real detection. Hence, we want to continue our investigation using a more realistic model where optical losses from the arm cavities and the SRM are considered. A schematic and the corresponding block diagram of Advanced LIGO with optical losses are shown in Fig. 2.15. We directly recall the lossy cavity block diagram as shown in Fig. 2.12 to represent the arm cavities. Based on these block diagrams, we can write down the input-output relation of the Advanced LIGO interferometer as:

$$\begin{aligned}
\begin{bmatrix} \hat{b}_1(\Omega) \\ \hat{b}_2(\Omega) \end{bmatrix} = &\left[-\sqrt{R_{\mathrm{sr}}}\mathbf{I} + e^{2i\theta}\frac{T_{\mathrm{sr}}\mathbf{M_{arm}}}{\mathbf{I} - e^{2i\theta}\sqrt{R_{\mathrm{sr}}}\mathbf{M_{arm}}}\right]\begin{bmatrix} \hat{a}_1(\Omega) \\ \hat{a}_2(\Omega) \end{bmatrix} \\
&+ \left[\frac{e^{i\theta}\sqrt{T_{\mathrm{sr}}}\mathbf{H_{arm}}}{\mathbf{I} - e^{2i\theta}\sqrt{R_{\mathrm{sr}}}\mathbf{M_{arm}}}\right] h(\Omega), \\
&+ \left[\frac{e^{i\theta}\sqrt{T_{\mathrm{sr}}}\mathbf{N}_{\mathrm{arm}}}{\mathbf{I} - e^{2i\theta}\sqrt{R_{\mathrm{sr}}}\mathbf{M_{arm}}}\right]\begin{bmatrix} \hat{n}_1^{\mathrm{arm}}(\Omega) \\ \hat{n}_2^{\mathrm{arm}}(\Omega) \end{bmatrix} \\
&+ \frac{e^{2i\theta}\sqrt{\mathcal{E}_{\mathrm{sr}}}\sqrt{T_{\mathrm{sr}}}\mathbf{M_{arm}}}{\mathbf{I} - e^{2i\theta}\sqrt{R_{\mathrm{sr}}}\mathbf{M_{arm}}}\begin{bmatrix} \hat{n}_1^{\mathrm{sr}}(\Omega) \\ \hat{n}_2^{\mathrm{sr}}(\Omega) \end{bmatrix}.
\end{aligned} \tag{2.81}$$

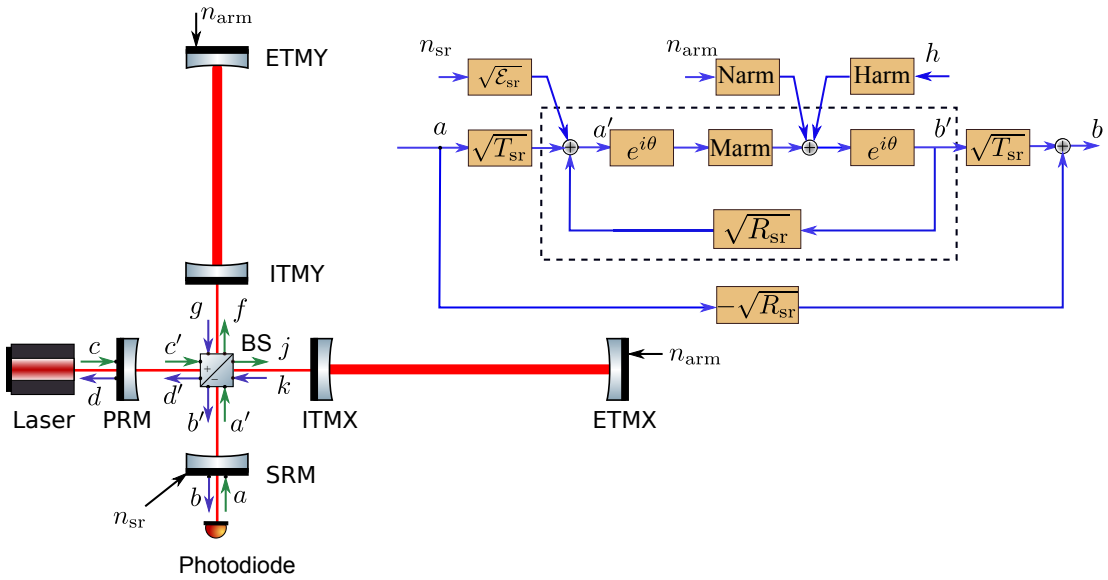

Figure 2.15.: Diagram showing the schematic and its corresponding block diagram of Advanced LIGO with optical losses included. $\hat{n}_{\rm arm}$ and $\hat{n}_{\rm sr}$ are the vacuum fluctuations induced by optical loss from the arm cavities ($\mathcal{E}_{\rm arm}$) and the SRM ($\mathcal{E}_{\rm sr}$). T_i and R_i are the transmissivity and reflectivity of ITMX/ITMY. Cavity losses are grouped into the transmission of ETMX/ETMY with $T_e = \mathcal{E}_{\rm arm}$. For the SRM, $R_{\rm sr} + T_{\rm sr} + \mathcal{E}_{\rm sr}$=1. $\mathbf{M}_{\rm arm}$, $\mathbf{N}_{\rm arm}$ and $\mathbf{H}_{\rm arm}$ are defined by Eqs. (2.68) and (2.69).

For the arm cavities, optical losses are grouped into the transmission of the cavity ETMs (ETMX and ETMY) as $\mathcal{E}_{\rm arm} = T_e$. For the SRM, the optical loss is $\mathcal{E}_{\rm sr}$; it satisfies $R_{\rm sr} + T_{\rm sr} + \mathcal{E}_{\rm sr} = 1$. $\hat{n}_{\rm arm}$ and $\hat{n}_{\rm sr}$ are the vacuum fluctuations induced by optical losses from the arm cavity and the SRM, respectively. $\mathbf{M}_{\rm arm}$ and $\mathbf{H}_{\rm arm}$ are defined by Eqs. (2.68) and (2.69). With the NSD definition in Eq. (2.72), we can obtain the quantum NSD of Advanced LIGO with optical losses in the arm cavities (the red dotted curve) and the SRM (the green dashed curve) as shown in Fig. 2.16.

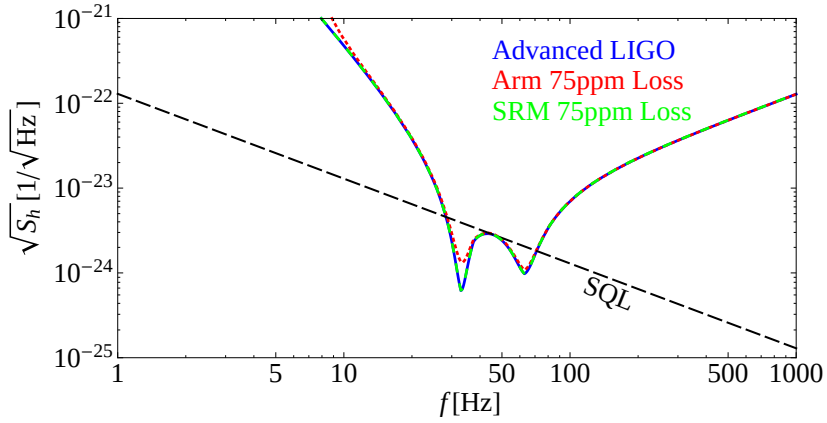

Figure 2.16.: Plot showing the quantum NSD of Advanced LIGO when optical losses from the arm cavity ETMs and the SRM are considered. The blue curve shows the lossless result which is exactly the same as in Fig. 2.14. Parameters are reused with $R_{sr} = 0.99$, $I = 100\,\text{kW}$, and $\theta = 1.35$. The red dashed line and green dashed line are the NSD of Advanced LIGO for a 75ppm loss from the arm cavity or the SRM, respectively.

Empirical loss values are typically provided by mirror manufacturers, and with state-of-the-art technology a single mirror loss of tens of ppm seems feasible. The plots in Fig. 2.16 demonstrate the quantum noise behaviour when mirror losses are included; this is in agreement with [58]. We found that a loss of 75 ppm from the SRM is negligible as the green dashed line (which includes the loss effect) almost coincides with the blue lossless curve. Optical losses from the arm cavities have a stronger influence and slightly degrade the low-frequency quantum noise behaviour compared to a case of a lossy SRM. This is because the storage time in the arm cavities are longer and thus results in multiple-trip losses. However, it is still quite small.

Based on the generic method (describing optical system input-output relation via block diagrams) developed and presented in this chapter, we will continue

our investigations to more specific techniques that allow to reduce low-frequency quantum noise in the following chapters.

Chapter 3.

Sensitivity of Intra-cavity Filtering

Advanced LIGO could have the quantum noise below the SQL through an implementation of a signal recycling mirror which forms a detuned cavity with the arm cavity ITMs and generates an optical spring as shown in Sections 2.4.1 and 2.4.2. Nevertheless, it is not a perfect solution since the sensitivity surpasses the SQL only with two narrow valleys (see Figs. 2.14 and Fig. 2.16), and moreover, this comes at the cost of a worse sensitivity at other frequencies.

Reducing quantum noise over the entire detection frequency band is important for advanced GW detectors. Two techniques have been previously proposed that could be applied to achieve this goal by modifying the input optics (input filter cavity) or the output optics (output filter cavity): *frequency-dependent squeezed input* and *frequency-dependent readout* (or *variational readout*) [54].

In the following (Section 3.1), we will first briefly review these two known filtering schemes (also referred to as 'Frequency-dependent Filtering' in this thesis) and present their quantum noise performances when optical losses from different optical components, such as arm cavities and filter cavities, are included. We then consider a new scheme called *intra-cavity filtering* in Section 3.2, in which

the optical cavity as a filter is placed inside the signal recycling cavity, formed by the SRM and the arm cavity ITMs. The analysis of different intra-cavity filtering schemes has been submitted for publication [1].

Frequency-dependent squeezed input

It is shown in [54] that the input quantum fluctuations can be manipulated into a *squeezed state* to surpass the SQL. A discussion of the generation of a squeezed state is beyond the scope of this thesis, but extensive explanations of a squeezed state, as well as the experimental feasibility, can be found in [66, 67, 68] *et al.* We follow the definition used in [54, 62, 63, 69] and represent the squeezed quadratures as

$$\begin{aligned}\hat{\mathbf{a}}_{\mathbf{s}}(\Omega) &= \mathbf{R}[-\phi]\begin{bmatrix} e^{r} & 0 \\ 0 & e^{-r} \end{bmatrix}\mathbf{R}[\phi]\hat{\mathbf{a}}(\Omega) \\ &= \begin{bmatrix} \cosh r + \sinh r\cos 2\phi & -\sinh r\sin 2\phi \\ -\sinh r\sin 2\phi & \cosh r - \sinh r\cos 2\phi \end{bmatrix}\hat{\mathbf{a}}(\Omega), \end{aligned} \tag{3.1}$$

where $\mathbf{R}[\phi]$ is the rotation matrix defined in Eq. (2.16) with ϕ being the *squeezing angle*, and r is the *squeezing factor*, i.e., a 10 dB phase squeezing corresponding to $r = 0.5\ln 10$.

As presented in Section 2.3, the quantum NSD can be generally computed given that the input-output relation of the optical system is known. It can be calculated according to the definitions in Eqs. (2.72) and (2.73). With a squeezed input, however, the NSD matrix $\mathbf{S}_a$ in these equations is no longer an identity matrix but it needs to be replaced by the squeezed NSD matrix $\mathbf{S_s}$ as

$$\mathbf{S_s}(\Omega) = \begin{bmatrix} \cosh 2r + \sinh 2r\cos 2\phi & -\sinh 2r\sin 2\phi \\ -\sinh 2r\sin 2\phi & \cosh 2r - \sinh 2r\cos 2\phi \end{bmatrix}, \tag{3.2}$$

according to the definition in Eq. (2.73).

For Advanced LIGO, we have the input-output relation as given in Eq. (2.78), where we consider the case of no SR cavity or the signal recycling cavity (SRC) being on resonance. In terms of applying frequency-dependent filtering, the two cases are similar. Here, for simplicity, we use the former case for example. Replacing $\mathbf{S_a}$ in Eq. (2.72) by Eq. (3.2), the quantum NSD of Advanced LIGO with squeezed input can be written as:

$$S_h(\Omega) = \frac{h_{\rm SQL}^2}{2}\left(\kappa_{\rm cav} + \frac{1}{\kappa_{\rm cav}}\right)\left(\cosh 2r + \cos 2(\phi + \text{arccot}\kappa_{\rm cav})\sinh 2r\right), \quad (3.3)$$

or equivalently (see explanation for Eq. (2.63)),

$$S_h(\Omega) = \frac{h_{\rm SQL}^2}{2}\left(\mathcal{K} + \frac{1}{\mathcal{K}}\right)\left(\cosh 2r - \cos 2(\phi + \text{arccot}\mathcal{K})\sinh 2r\right). \quad (3.4)$$

As we shall see, if the squeezing angle ϕ satisfies the frequency-dependent requirement as

$$\phi(\Omega) = -\text{arccot}\mathcal{K}, \qquad \mathcal{K} = \frac{T_i\kappa}{1 - 2\sqrt{R_i}\cos(2\Omega\tau) + R_i}, \quad (3.5)$$

the resulting quantum NSD yields

$$S_h(\Omega) = \frac{h_{\rm SQL}^2}{2}\left(\mathcal{K} + \frac{1}{\mathcal{K}}\right)e^{-2r}. \quad (3.6)$$

This gives an overall quantum noise reduction by a factor of e^{-2r}, with $0 < e^{-r} < 1$. Figure 3.1 shows a broadband quantum noise reduction with a 10 dB frequency-dependent squeezing input, where a 10 dB squeezing corresponds to $r = 0.5\ln 10$.

Frequency-dependent readout

Frequency-dependent readout enables a complete radiation pressure noise cancellation [54] by rotating the readout quadrature angle in a frequency-dependent way. It can be understood as follows: recalling the output expression of Advanced

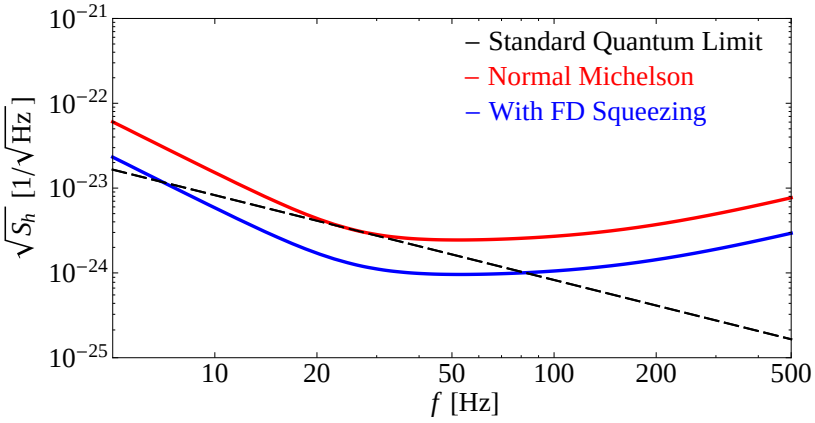

Figure 3.1.: Plot showing the quantum NSD of Advanced LIGO with 10 dB frequency-dependent (FD) squeezed input. The red curve shows a conventional Michelson interferometer as a reference.

LIGO again, Eq. (2.78), we have the output with a homodyne detection angle ζ as

$$\begin{aligned}\hat{b}_\zeta(\Omega) &= \hat{b}_1(\Omega)\cos\zeta + \hat{b}_2(\Omega)\sin\zeta \\ &= e^{-2i\Omega\tau}\left[(\cos\zeta - \mathcal{K}\sin\zeta)\hat{a}_1(\Omega) + \sin\zeta\hat{a}_2(\Omega)\right] + \sin\zeta\frac{\sqrt{2\mathcal{K}}}{h_{\mathrm{SQL}}}e^{-i\Omega\tau}h(\Omega).\end{aligned} \tag{3.7}$$

Consequently, the h-normalised NSD is

$$S_h(\Omega) = \frac{h_{\mathrm{SQL}}^2}{2\mathcal{K}}\left(\mathcal{K}^2 - 2\mathcal{K}\cot\zeta + \frac{1}{\sin^2\zeta}\right), \tag{3.8}$$

which gives a minimum noise value limited by shot noise only as

$$S_h(\Omega) = \frac{h_{\mathrm{SQL}}^2}{2\mathcal{K}}, \tag{3.9}$$

given that the readout angle is frequency-dependent and satisfies

$$\zeta(\Omega) = \mathrm{arccot}\mathcal{K}. \tag{3.10}$$

The frequency-dependent readout evades the low-frequency noise as shown in Fig. 3.2. It can be clearly seen that radiation pressure noise is completely evaded, therefore, this technique is also referred to as the *back action evasion* scheme.

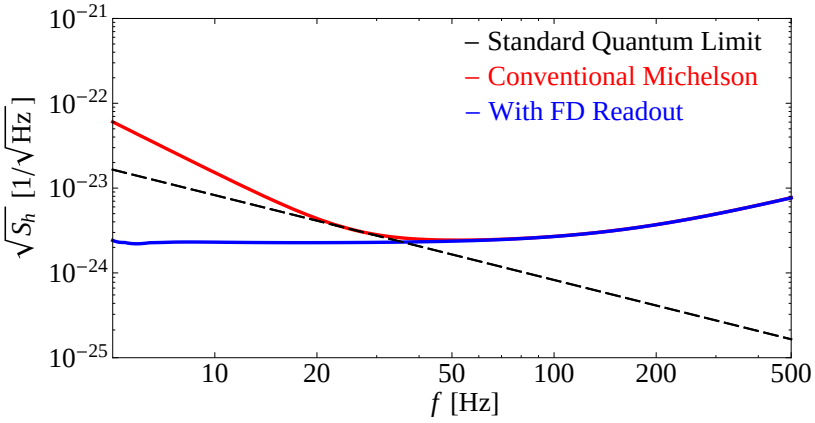

Figure 3.2.: Plot showing the quantum NSD of Advanced LIGO with frequency-dependent (FD) readout (blue). Compared with a conventional Michelson interferometer (red), the low-frequency quantum noise is completely evaded.

3.1. Frequency-dependent Filtering

For frequency-dependent squeezed input and frequency-dependent readout schemes, the key is to create a frequency dependence for the squeezing angle and the homodyne detection angle, as demanded by Eqs. (3.5) and (3.10). In this section, we will briefly review the realisation of this frequency-dependent angle by the use of detuned Fabry-Pérot cavities, which are known as 'Filter Cavities' and have been introduced in [54].

In Section 2.2.4, we have considered a rather complicated detuned Fabry-Pérot cavity, where the ETM mechanical motion and GW response have both been included. Here, the filter cavity is much simpler and only considered as rigid, which means no response to internal or external forces is accounted for as shown in Fig. 3.3. Thus, the cavity input-output relation can be quickly written down

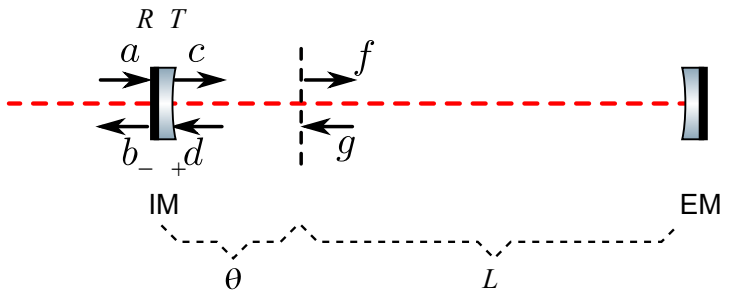

Figure 3.3.: Schematic showing a Fabry-Pérot cavity as a filter cavity with detuning phase θ, where $\omega_0 L/c = N \cdot \pi$. The input mirror is partially transmitting with transmissivity T. The EM is assumed to be a perfectly reflective mirror.

as:

$$\begin{bmatrix} \hat{b}_1(\Omega) \\ \hat{b}_2(\Omega) \end{bmatrix} = e^{i\psi_1}\mathbf{R}[\psi_2] \begin{bmatrix} \hat{a}_1(\Omega) \\ \hat{a}_2(\Omega) \end{bmatrix}, \tag{3.11}$$

with

$$\psi_1(\Omega) = \frac{\alpha_+(\Omega) - \alpha_-(\Omega)}{2}, \qquad \psi_2(\Omega) = \frac{\alpha_+(\Omega) + \alpha_-(\Omega)}{2}, \tag{3.12}$$

and $\mathbf{R}[\psi_2]$ being the rotation matrix defined by Eq. (2.16). Here $\alpha_+(\Omega)$ and $\alpha_-(\Omega)$ are the phase shifts of the upper and lower sidebands induced by the filter cavity. Given the sideband frequency is far smaller than the cavity free spectral range (see the FSR definition in Eq. A.5), these phase shifts can be approximated as

$$\alpha_\pm(\Omega) = 2\arctan\left(\frac{\Delta \pm \Omega}{\gamma}\right), \tag{3.13}$$

where $\gamma = T/4\tau$ is the cavity bandwidth and $\Delta = \theta/\tau$ is the cavity detuning frequency. As we can clearly see from Eq. (3.11), the quadrature rotation angle $\psi_2(\Omega)$ and the additional phase shift $\psi_1(\Omega)$, reflected by a detuned cavity, both show a frequency-dependent feature. They are determined by two important parameters: the cavity bandwidth γ and the cavity detuned frequency Δ. Therefore,

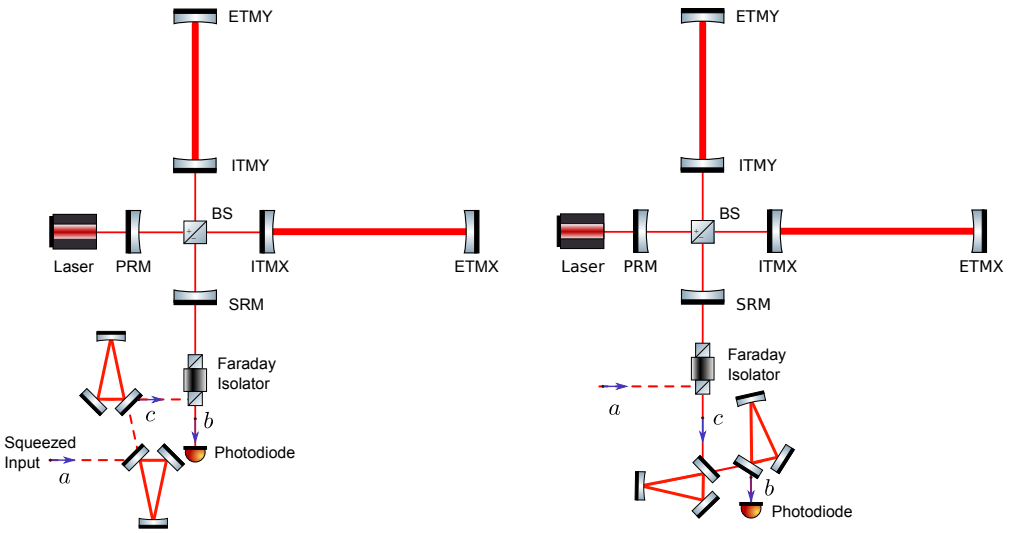

(a) Input Filtering (b) Output Filtering

Figure 3.4.: Schematic to show a dual-recycled Michelson topology with (a) a frequency-dependent squeezing and (b) a frequency-dependent readout. Both consist of a Michelson interferometer with arm cavities and a dual-recycling configuration.

if we can find realistic cavity parameters, which predict frequency dependencies as required by Eqs. (3.5) and (3.9) as

$$\psi_2(\Omega) = \phi(\Omega), \qquad \text{or} \qquad \psi_2(\Omega) = \zeta(\Omega), \tag{3.14}$$

then the detuned Fabry-Pérot cavity can be used to realise frequency-dependent squeezing input and frequency-dependent readout. Cavity parameters will therefore be determined by Eqs. (3.5), (3.10), and (3.14). Depending on cavity positions and functions, they form different *filtering schemes*. We will perform more detailed investigations on realistic schemes in Section. 3.1.1 and Section 3.2, including the practical designs of the filter cavities.

3.1.1. Lossless Input/Output Filtering

The scheme with the filter cavities placed before the squeezed state enters the GW detector is called input filtering as shown in Fig. 3.4(a) and these filter cavities are known as the *input filter cavities*. Filter cavities which modify the output optics and adjust the output signal as illustrated in Fig. 3.4(b) are called the *output filter cavities*.

We have obtained the quantum NSD of Advanced LIGO with input filtering and output filtering (See Figs. 3.1 and 3.2), however, specific filter cavity parameters are missing. In the following section, we will present how many of these cavities are actually needed for GW detectors and how to design a filter cavity to realise the required frequency-dependence. From Eqs. (3.5) and (3.10), we know that the cavity design for the input filter cavity should be the same as for the output filter case. Therefore, we use the input filtering as an example and deduce the input filter cavity parameters. The results will be valid for output filtering.

For a frequency-dependent squeezed input, the squeezing angle must satisfy

$$\psi(\Omega) = \phi(\Omega) = \text{arccot}\mathcal{K}, \tag{3.15}$$

where $\mathcal{K}$ is a function of Ω. Equation (3.12) indicates that the squeezing angle of a squeezed state after the filter cavity becomes

$$\psi(\Omega) = \theta_0 + \frac{1}{2}\sum_j^N \left(\alpha_{j+} + \alpha_{j-}\right), \qquad \alpha_{j\pm} = \arctan\left(\frac{\Delta_j \pm \Omega}{\gamma_j}\right), \tag{3.16}$$

where θ_0 is the original frequency-independent squeezing angle of the input squeezed state and N is the filter cavity number which shows how many filter cavities are needed for an optical configuration. We will shortly see that this number is determined by the expression of $\mathcal{K}$.

Cavity parameters can be resolved by solving the equation

$$\theta_0 + \frac{1}{2}\sum_j^N (\alpha_{j+} + \alpha_{j-}) = \text{arccot}\mathcal{K}. \tag{3.17}$$

We adopt a convenient mathematical solution introduced in [57] by using

$$e^{2i\psi} = \frac{1 + i\tan\psi}{1 - i\tan\psi}. \tag{3.18}$$

We then rearrange Eq. (3.15) and obtain

$$\tan\psi = \frac{1}{\mathcal{K}}. \tag{3.19}$$

Expressing the angle as shown in Eq. (3.16) in the form of an exponential format, we obtain

$$e^{2i\psi} = e^{2i\theta_0}\prod_j^N e^{i\alpha_{j+}} \cdot e^{i\alpha_{j-}}. \tag{3.20}$$

Combining Eqs. (3.18) and (3.20), Eq. (3.17) therefore equivalently turns into

$$\frac{\mathcal{K} + i}{\mathcal{K} - i} = e^{2i\theta_0}\prod_j^N \frac{\Omega + \Delta_j - i\gamma_j}{\Omega + \Delta_j + i\gamma_j} \cdot \frac{\Omega - \Delta_j + i\gamma_j}{\Omega - \Delta_j - i\gamma_j}. \tag{3.21}$$

It can be seen that different $\mathcal{K}$s correspond to different angles, thus indicating different cavity designs. In order to yield the parameters of the filter cavity, the explicit expression of $\mathcal{K}$ is therefore essential. We will briefly present two examples in the following where the difference is due to whether or not a resonant cavity response is present in the output of the GW detectors as illustrated in Fig. 3.5.

I. Interferometer without arm cavities

Based on the discussion in Section 2.4, an analog input-output relation of a GW detector without arm cavities as shown in Fig. 3.5(a) can be written as:

$$\begin{bmatrix} \hat{b}_1(\Omega) \\ \hat{b}_2(\Omega) \end{bmatrix} = e^{2i\Omega\tau}\begin{bmatrix} 1 & 0 \\ -\mathcal{K}_1 & 1 \end{bmatrix}\begin{bmatrix} \hat{a}_1(\Omega) \\ \hat{a}_2(\Omega) \end{bmatrix} + \frac{1}{2}\begin{bmatrix} 0 \\ e^{i\Omega\tau}\sqrt{2\mathcal{K}_1} \end{bmatrix}\frac{h(\Omega)}{h_{SQL}}, \tag{3.22}$$

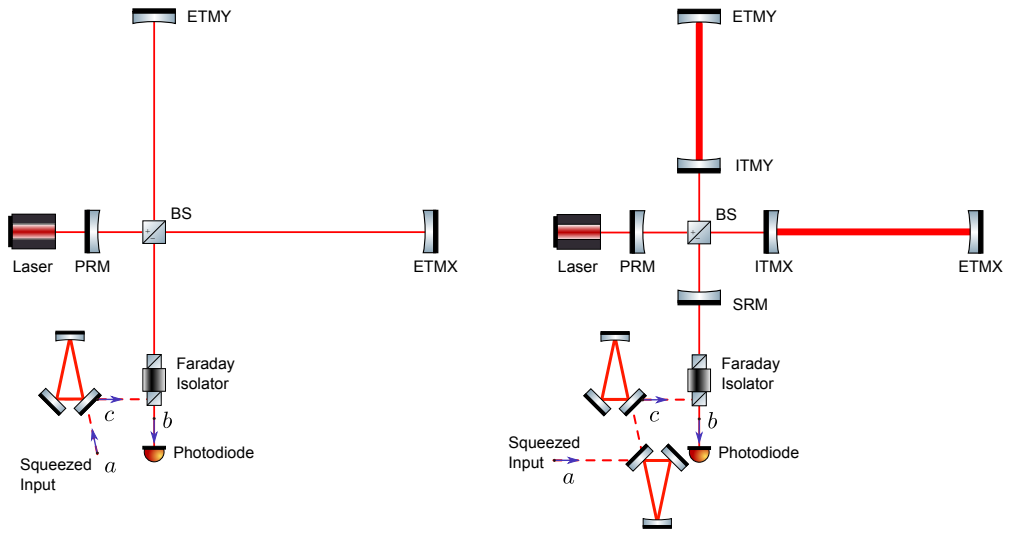

(a) (b)

Figure 3.5.: Schematic for two Michelson configurations with a frequency-dependent squeezed input. (a) A Michelson interferometer without the arm cavity nor the signal recycling cavity; (b) the Advanced LIGO configuration.

with

$$\mathcal{K}_1 = \frac{\Gamma^2}{\Omega^2}, \quad \Gamma = \sqrt{\frac{4I\omega_0}{mc^2}}, \qquad h_{SQL} = \sqrt{\frac{4\hbar}{m\Omega^2 L^2}}.$$

Replacing $\mathcal{K}$ in Eq. (3.21) by $\mathcal{K}_1$ for this case, the required relation is:

$$\frac{\Omega^2 + i\Gamma^2}{\Omega^2 - i\Gamma^2} = \frac{\Omega + \Delta - i\gamma}{\Omega + \Delta + i\gamma} \cdot \frac{\Omega - \Delta + i\gamma}{\Omega - \Delta - i\gamma}, \tag{3.23}$$

which immediately leads to the solution for the filter cavity parameters:

$$\gamma = \Delta = \frac{\Gamma}{\sqrt{2}} = \sqrt{\frac{2I\omega_0}{mc^2}}. \tag{3.24}$$

We found that: (i) the input frequency-independent squeezing angle θ_0 is 0; (ii) for a GW detector without any resonant cavity, one filter cavity ($N = 1$) is sufficient to meet the requirement. More specifically, the filter cavity bandwidth is about 28 Hz, using the parameters of the Advanced LIGO baseline design:

$I = 800\,\mathrm{kW}$, $m = 40\,\mathrm{kg}$, and the incident laser wavelength $\lambda = 1064\,\mathrm{nm}$. This narrow bandwidth implies that a long length and high finesse filter cavity is required (see Eq. A.6).

II. Interferometer with resonant cavity

For the configuration shown in Fig. 3.5(b), we can recall the expression of $\mathcal{K}_2$ from Eq. (2.39) and rewrite it here again as

$$\mathcal{K}_2 = \frac{\Lambda^4}{\Omega^2(\Omega^2+\gamma^2)}, \qquad \Lambda = (2\gamma\xi)^{\frac{1}{4}}. \tag{3.25}$$

The equation determining the filter cavity parameters is:

$$\frac{\Omega^4+\gamma^2\Omega^2-i\Lambda^4}{\Omega^4+\gamma^2\Omega^2+i\Lambda^4} = \frac{\Omega+\Delta_1-i\gamma_1}{\Omega+\Delta_1+i\gamma_1}\cdot\frac{\Omega-\Delta_1+i\gamma_1}{\Omega-\Delta_1+i\gamma_1}\cdot\frac{\Omega+\Delta_2-i\gamma_2}{\Omega+\Delta_2+i\gamma_2}\cdot\frac{\Omega-\Delta_2+i\gamma_2}{\Omega-\Delta_2-i\gamma_2} \tag{3.26}$$

Again, the input frequency-independent squeezing angle θ_0 is 0 and due to the highest order of Ω being 4 now, two filter cavities are needed to cancel both the opto-mechanical response and the cavity optical response. Cavity parameters can be achieved by solving the equation $\Omega^4+\gamma^2\Omega^2-i\Lambda^4=0$. Note that γ_j and Δ_j are always real numbers and $\gamma_j > 0$ is always true according to the definition expressed in Eq. (3.12). Inserting the parameters of Advanced LIGO, we obtain the required bandwidth is around 100 Hz, which is still narrow.

In conclusion, the parameters of the filter cavity can be obtained by solving the frequency-dependent equation

$$\mathcal{K} - i = 0 \tag{3.27}$$

and these solutions, which are complex numbers, correspond to $\pm\Delta_j \mp i\gamma_j$ and determine the parameters of filter cavities. $\mathcal{K}$ is a function of Ω^{2N}, where N is number of the filter cavities needed.

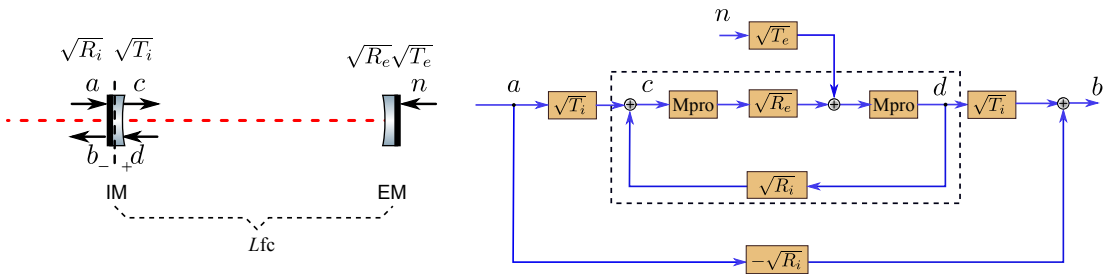

Figure 3.6.: Diagrams showing the schematic of a lossy filter cavity and its block diagram. The filter cavity is considered as a rigid cavity that does not sense external forces (GW signals). Optical losses are grouped into the transmission T_e of the filter cavity EM as before.

3.1.2. Lossy Input/Output Filtering

Based on the filter cavity TF as shown in Eq. (3.11), we can use a block diagram to represent a filter cavity when optical losses are considered within the filter cavity EM transmission as shown in Fig. 3.6. According to the general expression of a cavity (see Eq. (2.60)), we immediately obtain the input-output relation of a filter cavity including optical losses as:

$$\begin{bmatrix} \hat{b}_1(\Omega) \\ \hat{b}_2(\Omega) \end{bmatrix} = \left[-\sqrt{R_i}\mathbf{I} + \frac{T_i \mathbf{M}^{\mathbf{fc}}_{\mathbf{op}}}{\mathbf{I} - \sqrt{R_i}\mathbf{M}^{\mathbf{fc}}_{\mathbf{op}}} \right] \begin{bmatrix} \hat{a}_1(\Omega) \\ \hat{a}_2(\Omega) \end{bmatrix} + \left[\frac{\sqrt{T_i}\sqrt{T_e}\mathbf{M}^{\mathbf{fc}}_{\mathbf{pro}}}{\mathbf{I} - \sqrt{R_i}\mathbf{M}^{\mathbf{fc}}_{\mathbf{op}}} \right] \begin{bmatrix} \hat{n}_1(\Omega) \\ \hat{n}_2(\Omega) \end{bmatrix}, \tag{3.28}$$

where

$$\mathbf{M}^{\mathbf{fc}}_{\mathbf{pro}} = e^{i\Omega\tau_{\mathrm{fc}}}\mathbf{R}[\Omega\tau_{\mathrm{fc}}], \qquad \mathbf{M}^{\mathbf{fc}}_{\mathbf{op}} = \sqrt{R_e}\mathbf{M}^{\mathbf{fc}}_{\mathbf{pro}} \cdot \mathbf{M}^{\mathbf{fc}}_{\mathbf{pro}}, \qquad \tau_{\mathrm{fc}} = \frac{L_{\mathrm{fc}}}{c}. \tag{3.29}$$

We simplify this input-output relation into

$$\begin{bmatrix} \hat{b}_1(\Omega) \\ \hat{b}_2(\Omega) \end{bmatrix} = \mathbf{M}_{\mathbf{fc}} \begin{bmatrix} \hat{a}_1(\Omega) \\ \hat{a}_2(\Omega) \end{bmatrix} + \mathbf{N}_{\mathbf{fc}} \begin{bmatrix} \hat{n}_1(\Omega) \\ \hat{n}_2(\Omega) \end{bmatrix}, \tag{3.30}$$

where $\mathbf{M}_{\mathbf{fc}}$ and $\mathbf{N}_{\mathbf{fc}}$ correspond to the matrices in Eq. (3.28). We thus have a new block diagram of a filter cavity when optical losses are considered as shown in

Fig. 3.7.

As we have shown in Section 2.4.2, optical losses either from the arm cavity or the SRM are negligible given the loss level of each mirror is only several ppm, e.g., 35 ppm. In the following section, we will compare the quantum noise performance when optical losses from filter cavities are considered.

Lossy input filtering

We consider the implementation of frequency-dependent squeezing for Advanced LIGO first, adding optical filter cavities before the Advanced LIGO configuration (see Fig. 2.15). The input filtering scheme for Advanced LIGO and its corresponding block diagram are shown in Fig. 3.8.

According to the frequency-dependent requirement demonstrated in Section 3.1, two filter cavities are needed for such a configuration. With the specific block diagram, we are able to write down the final input-output relation and achieve the quantum NSD. However, showing them is not necessary since the final equation with optical loss effects taken into account is lengthy and only contains simple physics. Following the same procedure, we could investigate the quantum NSD of Advanced LIGO with a frequency-dependent squeezed input when optical losses from different ports are considered. Figure 3.9(a) shows the quantum noise behaviour of Advanced LIGO under different conditions: (i) the blue curve gives

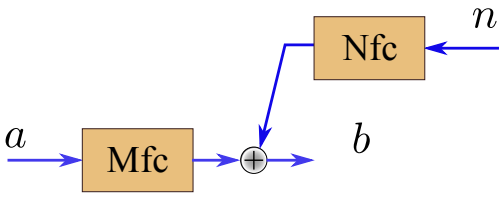

Figure 3.7.: A block diagram of a general lossy filter cavity. The TFs are defined in Eqs. (3.28) and (3.30).

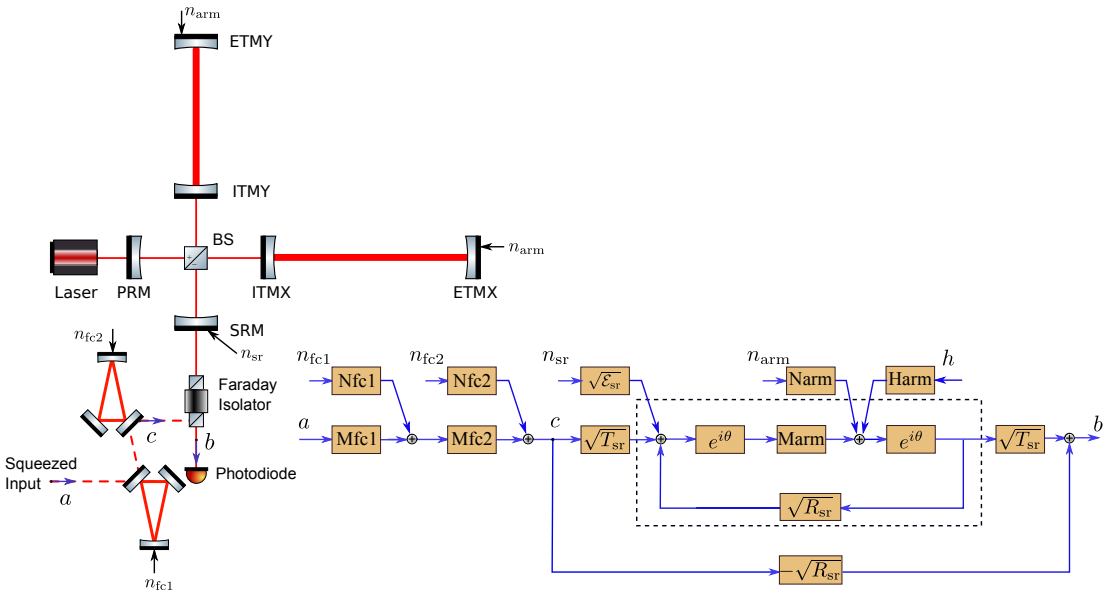

Figure 3.8.: Diagrams showing the schematic of Advanced LIGO with frequency-dependent squeezing input and its corresponding block diagram. Input filter cavities are placed before the squeezed state enters the interferometer (see Fig. 2.15). Here, the SRM is assumed to be tuned.

the ideal plot when 10 dB frequency-dependent squeezing is realised by the use of lossless filter cavities. This has already been discussed and shown in Fig. 3.1; (ii) the green dashed curve, which almost matches the blue one, includes a 75 ppm cavity round-trip loss in both arm cavities but still with lossless filter cavities; (iii) the magenta dashed curve shows the influence of a 75 ppm round-trip loss from each filter cavity. We have found that: (I) optical losses (below 100 ppm, which is achievable) from arm cavities, more specifically from optical components in the main interferometer, i.e., BS, PRM, SRM, are negligible compared to the influence from the input filter cavities; (II) low-frequency quantum noise is degraded due to optical losses from input filter cavities.

We are aware that optical losses from filter cavities affects low-frequency quantum noise. Figure 3.10(a) then shows degradation levels of radiation pressure noise due

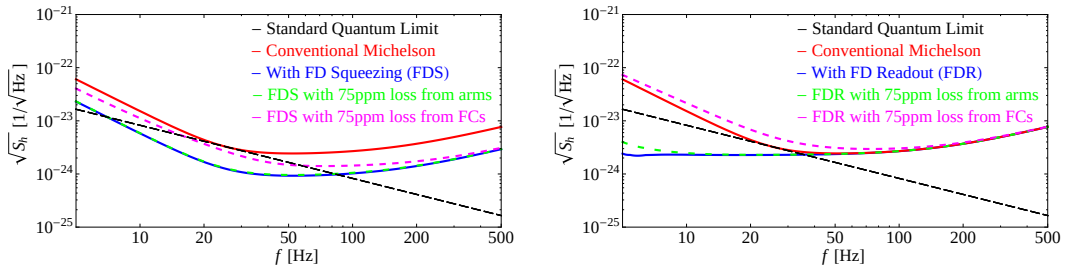

(a) Input filtering

(b) Output filtering

Figure 3.9.: Plots showing the quantum NSD of Advanced LIGO when (a) lossy input filtering and (b) lossy output filtering is implemented. Optical losses are considered from two ports: arm cavities and filter cavities (FC), respectively. The blue curves in (a) and (b) in turn provide the ideal 10 dB frequency-independent squeezing or frequency-dependent readout, which have been presented in Figs. 3.1 and 3.2. The green and magenta dashed curves show loss effects due to 75 ppm losses from arm cavities and input filter cavities, respectively.

to different loss levels. Not surprisingly, low loss input filter cavities are always preferred.

Lossy output filtering

Now that we have a detailed description of the lossy input filtering model, the lossy output filtering is rather obvious. The schematic of Advanced LIGO with a frequency-dependent readout and its block diagram are shown in Fig. 3.11. Likewise, the input-output relation of Advanced LIGO with a frequency-dependent readout can be achieved via this block diagram. We compare the quantum noise performance when 75 ppm losses from arm cavities and output filter cavities are considered, respectively, as we discussed for the input filtering case.

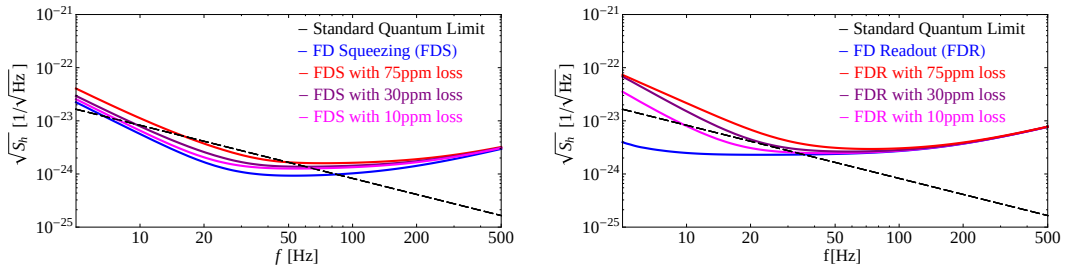

(a) Input filtering

(b) Output filtering

Figure 3.10.: Plots showing the quantum NSD of Advanced LIGO when different levels of optical losses from different input and output filter cavities are considered. (a) Quantum noise changes using input filtering and (b) Quantum noise behaviour when using output filtering. The blue curves in both plots are ideal cases. The other traces correspond to different losses entering both filter cavities.

The blue curve in Fig. 3.9(b) shows the ideal back action evasion of Advanced LIGO by using two lossless output filter cavities, which confirms what has been predicted in Fig. 3.2. The red plot depicts the quantum noise of Advanced LIGO based on the basic configuration as a reference. We can see that even a 75 ppm optical loss from the arm cavity degrades the low-frequency quantum noise as shown in Fig. 3.9(b) by the dashed green line. The magenta curve in Fig. 3.9(b) shows a strong degradation when there are 75 ppm losses from the output filter cavities. We found that the output filtering scheme is extremely susceptible to losses from output filter cavities. This is due to the fact that the measured output quadrature is close to the amplitude quadrature, which means the GW signal is much smaller than in the non-filtering case, therefore is more susceptible to optical losses in output filter cavities. With 75 ppm losses, the sensitivity is even worse than the case without the use of any output filtering scheme, which means if we cannot find a low-loss cavity for output filtering, the implementation does not

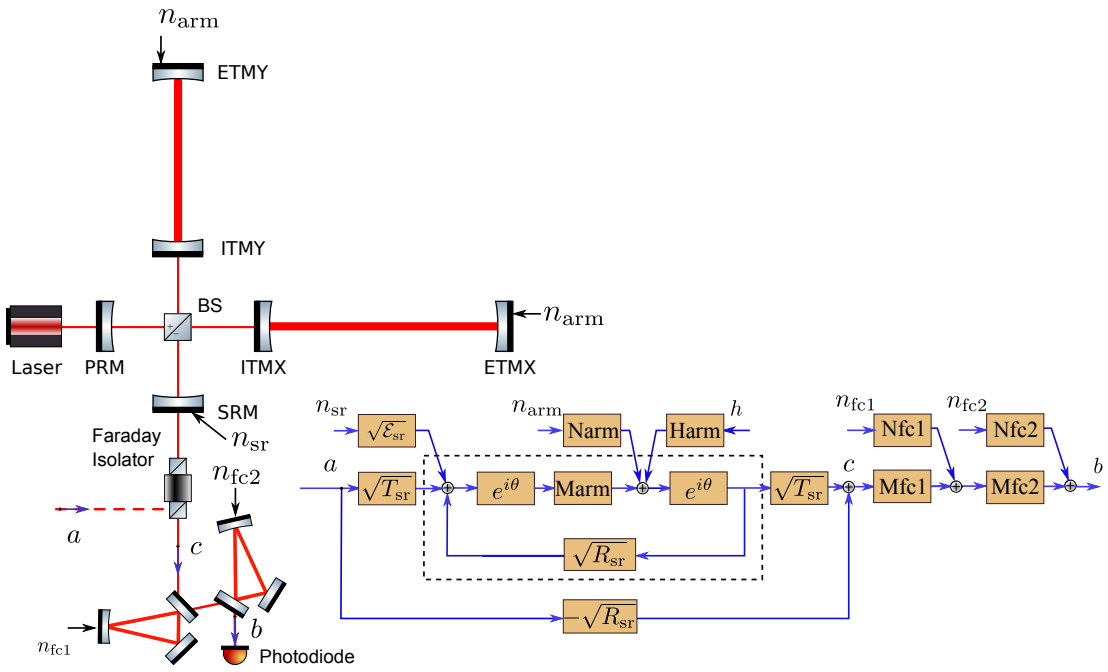

Figure 3.11.: Diagrams showing the schematic of Advanced LIGO with a frequency-dependent readout and its corresponding block diagram. Filter cavities are placed after the interferometer but before the output detected by photodiode. Here the SRM is assumed to be tuned again.

seem practical at all.

Figure 3.10(b) again compares the quantum noise behaviour of Advanced LIGO with frequency-dependent readout when different optical loss levels from output filter cavities are considered. Compared with input filtering, due to the severe optical loss issue, implementation of output filtering is much less encouraging.

Hence, the realisation of a filter cavity is important, particularly when imperfection effects, i.e., optical losses, are taken into account. We investigate the design of an optical cavity in greater detail in Chapter 5 arming at minimum cavity optical losses.

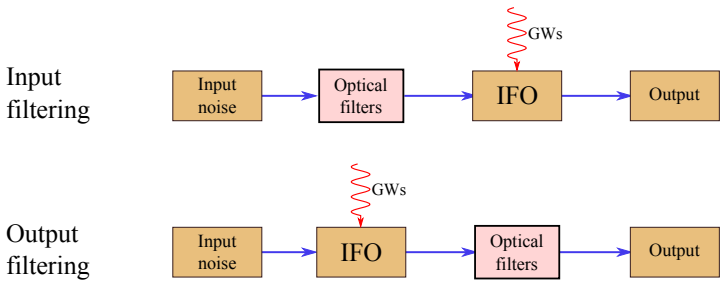

Figure 3.12.: Block diagrams illustrating input filtering (upper) and output filtering (lower) schemes for GW detectors. The vacuum noise enters through the dark port of an interferometer (IFO). GWs are sensed by the ITMs and ETMs of the IFO and their differential motion is detected by the photodetector. The output contains both GW signals and noises.

3.2. Intra-cavity Filtering

We have considered placing optical filters before and after a dual-recycled Michelson interferometer to enhance the quantum noise sensitivity of GW detectors (see Fig. 3.4), which can be summarised into two block diagrams as illustrated in Fig. 3.12.

In this section, we consider a new filtering scheme: intra-cavity filtering, in which we place the optical filters inside the *signal recycling cavity* (SRC), formed by the SRM and ITMs. A generic intra-cavity filtering scheme and its corresponding block diagram are schematically shown in Fig. 3.13. Given different optical filters chosen for the intra filtering scheme (see the pink block in Fig. 3.13), the interferometer could have different quantum noise sensitivities. In this thesis we will only focus on the following three different intra-filtering schemes: (i) cancelling the radiation pressure noise, (ii) working as a speed meter, or (iii) achieving a broadband quantum noise reduction. Note that the major results presented in

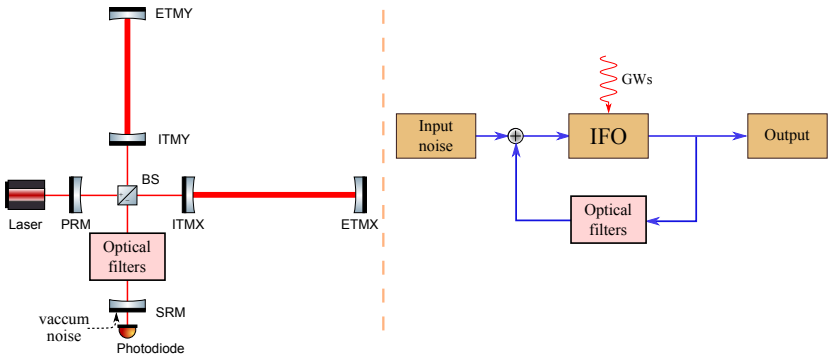

Figure 3.13.: Schematic of an Advanced GW interferometer with intra-filtering and its block diagram. Optical filters are placed between the Michelson interferometer and the SRM. GWs create differential motion in the perpendicular arms and are detected by the photodiode. The vacuum noise enters the IFO at the dark port. A feedback loop is formed due to the SRM. Figure taken from [1].

this section can also be found in the submitted paper [1].

3.2.1. Case I: Cancelling Radiation Pressure Noise

Kimble *et al*. [54] revealed that the radiation pressure noise of GW detectors can be completely cancelled by utilising ideal frequency-dependent readout; the sensitivity then is only limited by the shot noise (see Eq. (3.9) and Fig. 3.2). As shown in Section 3.1, this can be realised by the use of cascade filter cavities, which provide the required frequency-dependence for the homodyne detection angle. However, as shown in Fig. 3.9(b), the performance of a frequency-dependent readout is extremely susceptible to optical losses, in particular the losses of the output filter cavities. We use the ideal frequency-dependent readout scheme as a reference and investigate an intra-cavity filtering scheme for cancelling the radiation pressure noise with an improved robustness to optical losses.

We propose an intra-cavity filtering scheme as schematically shown in Fig. 3.14, in which one filter cavity and a resonant-sideband-extraction (RSE) mirror [70] are placed inside the SRC. The RSE mirror is used to remove the frequency response of the arm cavities such that only one filter cavity is needed fro cancelling the redaction pressure dependence (see a TF $\mathbf{M_{ifo}}$ of the interferometer according to Eq. (2.25)), namely

$$\mathbf{M_{ifo}} = e^{2i\Omega L/c}\begin{bmatrix} 1 & 0 \\ -\kappa & 1 \end{bmatrix}, \tag{3.31}$$

with

$$\kappa = \frac{8I_0\omega_0}{mc^2\Omega^2} \tag{3.32}$$

rather than Eq. (2.38). Note that one can equivalently use two filter cavities as described in Section 3.1 to cancel the radiation pressure noise without the use of the RSE mirror.

We found from Eqs. (3.26) and (3.27) that with such a κ, one filter cavity is sufficient to evade the radiation pressure noise by choosing the filter cavity detuning frequency and bandwidth to be (see Eq. (3.24))

$$\Delta_f = \gamma_f = \sqrt{\frac{2I_c\omega_0}{mc^2}}. \tag{3.33}$$

The combined effect of $\mathbf{M_{ifo}}$ (see Eq. (3.31)) and $\mathbf{M_{fc}}$ (see Eq. (3.11)) on the quadrature can therefore be described by

$$\begin{aligned}
\mathbf{M_{fc}}\mathbf{M_{ifo}}\mathbf{M_{fc}} &= e^{2i\phi_{\rm tot}}\begin{bmatrix} \cos\zeta_f & -\sin\zeta_f \\ \sin\zeta_f & \cos\zeta_f \end{bmatrix}\begin{bmatrix} 1 & 0 \\ -\kappa & 1 \end{bmatrix}\begin{bmatrix} \cos\zeta_f & -\sin\zeta_f \\ \sin\zeta_f & \cos\zeta_f \end{bmatrix} \\
&= e^{2i\phi_{\rm tot}}\begin{bmatrix} \cos 2\zeta_f + \frac{\kappa}{2}\sin 2\zeta_f & -\sin 2\zeta_f - \kappa\sin^2\zeta_f \\ \sin 2\zeta_f - \kappa\cos^2\zeta_f & \cos 2\zeta_f + \frac{\kappa}{2}\sin 2\zeta_f \end{bmatrix} \\
&= e^{2i\phi_{\rm tot}}\begin{bmatrix} 1 & -\kappa \\ 0 & 1 \end{bmatrix},
\end{aligned} \tag{3.34}$$

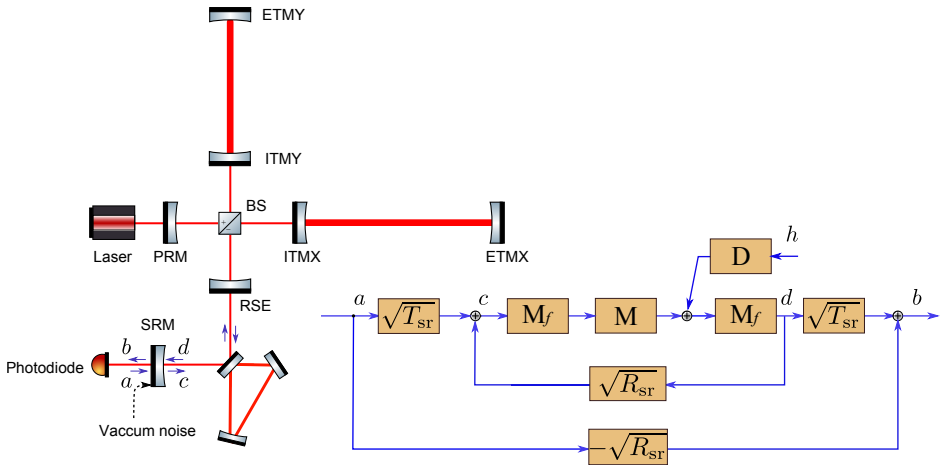

Figure 3.14.: Diagram showing a schematic and its corresponding block diagram of an intra-filtering scheme for evading radiation pressure noise. An optical filter is placed in the signal recycling cavity. Vacuum noise directly enters the IFO while the output gets filtered by the filter cavity. The resonant-sideband-extraction (RSE) mirror is used to effectively cancel the arm cavities response. Figure taken from [1].

and the GW TF afterwards is

$$\mathbf{M_{fc}H_{arm}} = e^{i(\Omega L/c+\phi_{\rm fc})}\begin{bmatrix}\cos\zeta_f & -\sin\zeta_f\\ \sin\zeta_f & \cos\zeta_f\end{bmatrix}\begin{bmatrix}0\\ \frac{\sqrt{2\kappa}}{h_{\rm SQL}}\end{bmatrix} = e^{i(\Omega L/c+\phi_{\rm fc})}\begin{bmatrix}-\frac{\sqrt{2\kappa}}{h_{\rm SQL}}\sin\zeta_f\\ \frac{\sqrt{2\kappa}}{h_{\rm SQL}}\cos\zeta_f\end{bmatrix}, \tag{3.35}$$

with the rotation angle

$$\tan\zeta_f = \kappa/2, \tag{3.36}$$

after the filter cavity and $\phi_{\rm tot} = \Omega L/c + \phi_{\rm fc}$. This upper triangular matrix shows that the radiation pressure noise from the input amplitude quadrature is removed from the output phase quadrature. Corresponding to the schematic in Fig. 3.14, it means that if we measure the output phase quadrature b_2 which depends only on the input phase quadrature a_2, we shall obtain a sensitivity only limited by

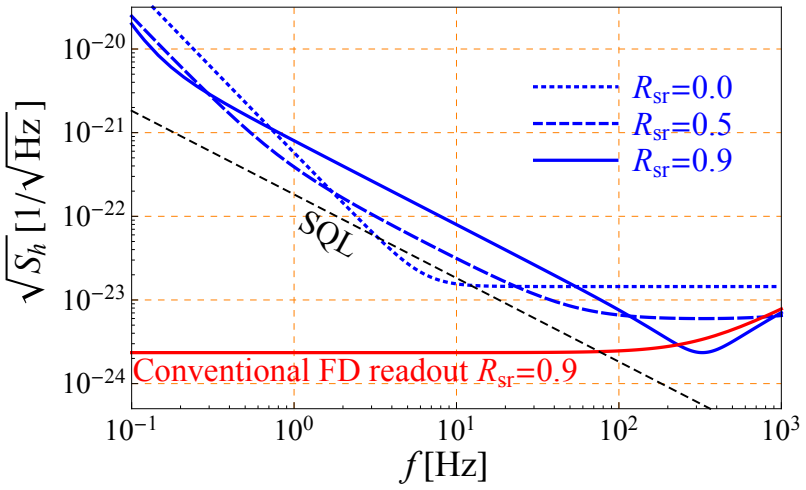

Figure 3.15.: Plot showing the sensitivity of the intra-cavity filtering scheme for evading radiation pressure noise with different signal recycling mirror reflectivities (blue) in comparison with the conventional frequency-dependent (FD) readout scheme (red) proposed in [54]. Figure taken from [1].

the shot noise. We then consider the SRM, which forms a feedback loop as shown in the block diagram, and achieve the final input-output relation

$$\boldsymbol{b} = \left[-\sqrt{R_{\rm sr}}\mathbf{I} + T_{\rm sr}\mathbf{M_c}\mathbf{M_{fc}}\mathbf{M_{ifo}}\mathbf{M_{fc}}\right]\boldsymbol{a} + \sqrt{T_{\rm sr}}\mathbf{M_c}\mathbf{M_{fc}}\mathbf{H_{arm}}h, \tag{3.37}$$

where $\mathbf{M_c} = \left[\mathbf{I} - \sqrt{R_{\rm sr}}\mathbf{M_{fc}}\mathbf{M_{ifo}}\mathbf{M_{fc}}\right]^{-1}$.

Naively one should expect that by just placing *one* filter cavity inside the signal recycling cavity we can achieve the same sensitivity as the conventional frequency-dependent readout as shown in Fig. 3.2. However, as shown in Fig. 3.15, this is not the case, and the performance is worse. Moreover, the sensitivity decreases as we increase the reflectivity of SRM ($R_{\rm sr}$); even when the reflectivity goes to zero (no signal-recycling mirror), we do not recover the frequency-dependent readout.

To understand the sensitivity degradation in comparison with the conventional

frequency dependent readout, we first look at the case of $R_{\rm sr} = 0$. We can write down the input-output relation for the phase quadrature explicitly as (normalized with respect to strain)

$$y_2 = \frac{e^{i\phi_{\rm tot}} h_{\rm SQL}}{\sqrt{2\kappa}\cos\zeta_f} a_2 + h \equiv \delta h + h\,. \tag{3.38}$$

At low frequencies $\Omega \ll \Omega_q$, $\kappa \gg 1$, $\cos\zeta_f \sim 1/\kappa$ and the strain-referred noise term δh reads

$$\delta h|_{\Omega\ll\Omega_q} \approx \sqrt{\frac{\kappa}{2}}\, h_{\rm SQL} a_2 \propto \frac{h_{\rm SQL}}{\Omega} a_2\,. \tag{3.39}$$

Therefore, even though it is a shot-noise limited sensitivity, the spectrum of the shot noise is not flat and increases at low frequencies as shown by the dotted line in Fig. 3.15. This comes from the additional rotation of the input vacuum field by the filter cavity, which is absent in the usual frequency-dependent readout (see Eq. (3.7)).

For $R_{\rm sr} \neq 0$, the expression for the output phase quadrature (strain-referred) is:

$$y_2 = \frac{e^{i\phi_{\rm tot}}(1-\sqrt{R_{\rm sr}}e^{2i\phi_{\rm tot}})h_{\rm SQL}}{\sqrt{2T_{\rm sr}\kappa}\,\cos\zeta_f}\, a_2 + h \equiv \delta h + h\,, \tag{3.40}$$

with the phase factor being

$$e^{2i\phi_{\rm tot}} = e^{2i\Omega L_{\rm arm}/c}\frac{(\Omega - i\Omega_q/2)^2 - \Omega_q^2/4}{(\Omega + i\Omega_q/2)^2 - \Omega_q^2/4}\,. \tag{3.41}$$

To understand the behaviour as shown in Fig. 3.15, we consider the case of $T_{\rm sr} \ll 1$ at three different frequency regimes: (i) *at very low frequencies* $\Omega \ll \Omega_q/2$, we have $e^{2i\phi_{\rm tot}} \sim 1$ and $\cos\zeta \sim 1/\kappa$. We can therefore obtain

$$\delta h|_{\Omega\ll\Omega_q/2} \approx \sqrt{\frac{T_{\rm sr}\kappa}{8}} h_{\rm SQL} a_2 \propto \sqrt{T_{\rm sr}}\frac{h_{\rm SQL}}{\Omega} a_2\,. \tag{3.42}$$

The frequency dependence is the same as $R_{\rm sr} = 0$ (see Eq. (3.39)) but with an additional factor $\sqrt{T_{\rm sr}}$—the smaller $T_{\rm sr}$ the better the sensitivity; (ii) *at intermediate frequencies* around $\Omega_q/2$, we have

$$1 - \sqrt{R_{\rm sr}}e^{2i\phi_{\rm tot}} \approx \frac{2i\,\Omega\,\Omega_q}{(\Omega + i\Omega_q/2)^2 - \Omega_q^2/4}\,. \tag{3.43}$$

At frequencies smaller than (yet still around) $\Omega_q/2$, it is approximated to be $-4i\Omega/\Omega_q$; at higher frequencies $\Omega \gtrsim \Omega_q/2$, it approximately equals to $2i\Omega_q/\Omega$. Therefore, we obtain the strain-referred noise term:

$$\delta h|_{\Omega\lesssim\Omega_q/2} \propto \frac{\Omega\sqrt{\kappa}}{\sqrt{T_{\rm sr}}}\, h_{\rm SQL}a_2 \propto \frac{h_{\rm SQL}}{\sqrt{T_{\rm sr}}}a_2\,, \tag{3.44}$$

and

$$\delta h|_{\Omega\gtrsim\Omega_q/2} \propto \frac{1}{\Omega\sqrt{\kappa}\sqrt{T_{\rm sr}}}\, h_{\rm SQL}a_2 \propto \frac{h_{\rm SQL}}{\sqrt{T_{\rm sr}}}a_2\,, \tag{3.45}$$

where we used the fact that $\Omega\sqrt{\kappa} \propto \Omega^0$. This explains why the spectrum is parallel to the SQL around intermediate frequencies. We also notice that the sensitivity decreases as we increase the reflectivity (smaller $T_{\rm sr}$); (iii) *at very high frequencies* $\Omega \gg \Omega_q/2$, we have

$$1-\sqrt{R_{\rm sr}}e^{2i\phi_{\rm tot}} \approx T_{\rm sr}/2 - 2i\Omega L_{\rm arm}/c, \tag{3.46}$$

and

$$\delta h|_{\Omega\gg\Omega_q/2} \propto \frac{T_{\rm sr}-4i\Omega L_{\rm arm}/c}{\sqrt{T_{\rm sr}\kappa}} h_{\rm SQL}a_2\,. \tag{3.47}$$

At very high frequencies, the noise spectrum increases as frequency Ω, which matches the spectrum behaviour as shown in Fig. 3.15 (the blue solid curve).

It is worthy mentioning that if the filter cavity is tuned to be resonant, instead of detuned for evading the radiation-pressure noise, the above scheme becomes a speed meter, even when the RSE mirror is removed, as we will discuss in section 3.2.2.

3.2.2. Case II: Realising a Speed Meter

In this section, we investigate the intra-cavity filtering as a speed meter, inspired by the speed meter scheme introduced in [57].

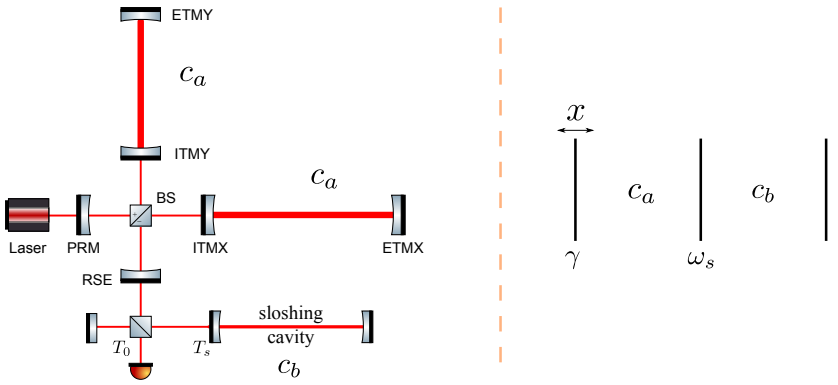

Figure 3.16.: The speed meter realised by adding an additional sloshing cavity at the output port proposed in [57] (left) and its simplified two-cavity-mode model (right). Figure taken from [1].

Brief review of the speed meter with a sloshing cavity

The speed meter scheme with a sloshing cavity, which motivates our work, is shown in Fig. 3.16, where a sloshing cavity combined with a RSE mirror is added to the interferometer output. Again the RSE mirror is applied to cancel the effect of the ITMs of the arm cavities, and it has the same transmissivity as the ITMs. In this case, the speed response can then be understood qualitatively by using the model of two coupled cavity modes as shown by the right part of Fig. 3.16. In particular, the cavity mode c_a corresponds to the optical field inside the arm cavities, and the cavity mode c_b is the field inside the sloshing cavity. These two cavity modes are coupled via the sloshing mirror with a characteristic coupling rate given by the sloshing frequency ω_s, which is defined as

$$\omega_s = \frac{c\sqrt{T_s}}{2\sqrt{L_{\rm arm}L_s}}, \tag{3.48}$$

with L_s being the length of the sloshing cavity and T_s being the transmissivity of the sloshing mirror.

The classical equations of motion for these two cavity modes can be written as

$$\dot{c}_a + \gamma c_a = -i\,G\,x - i\,\omega_s c_b\,, \tag{3.49}$$

$$\dot{c}_b = -i\,\omega_s c_a\,. \tag{3.50}$$

Here $\gamma = cT_0/4L_{\rm arm}$ is the *signal extraction rate*, with T_0 being the transmissivity of the extraction mirror (see Eq. (2) of [57]), and G quantifies the response strength of the cavity mode to the test mass displacement. Solving these two equations in the frequency domain yields

$$c_a(\Omega) = \frac{G\,\Omega}{\Omega^2 - \omega_s^2 + i\Omega\gamma} x(\Omega)\,. \tag{3.51}$$

At low frequencies $\Omega \ll \omega_s$ and with a small extraction rate $\gamma < \omega_s$, we have

$$c_a(\Omega) \approx -\frac{G\,\Omega}{\omega_s^2} x(\Omega) \propto -i\,\Omega\,x(\Omega)\,, \tag{3.52}$$

which implies the speed response.

The exact input-output relation for such a scheme has been shown in [57] (see Eqs. (12), (13) and (14) in the paper), and is in a similar form as Eq. (2.38) with $\mathcal{K}$ redefined by

$$\mathcal{K}_{\rm sm} = \frac{16\omega_0 I_c}{mL_{\rm arm}c|\Omega^2 - \omega_s^2 + i\gamma\Omega|^2}\,. \tag{3.53}$$

Notice that $\mathcal{K}_{\rm sm}$ is nearly a constant at low frequencies instead of having a strong frequency dependence. This means that in order to evade the radiation pressure noise at low frequencies by satisfying Eq. (3.10), one can simply measure a quadrature that is frequency independent with a detection angle

$$\zeta_{\rm sm} = \arctan \mathcal{K}_{\rm sm}|_{\Omega\to 0}\,. \tag{3.54}$$

A frequency-dependent readout is only needed when a better sensitivity is particularly required at high frequencies. This is due to the fact that high-frequency sensitivity is normally degraded if $\zeta_{\rm sm}$ is different from zero (which represents the phase quadrature).

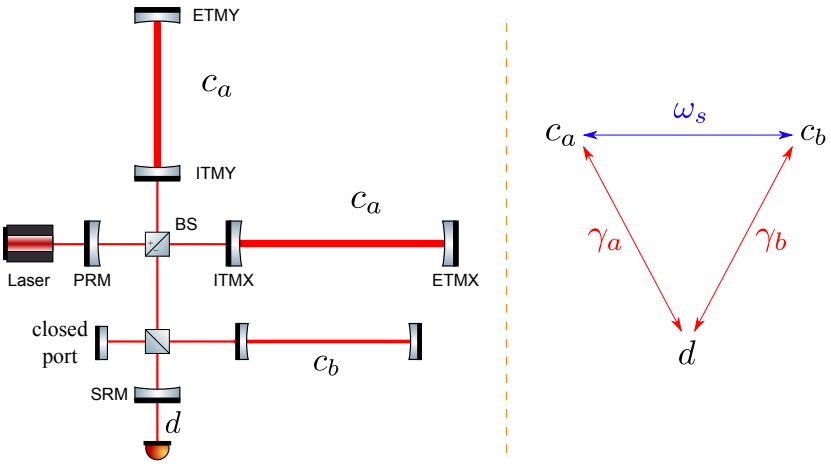

Figure 3.17.: The intra-cavity filtering scheme as a speed meter (left). Compared with the speed meter with a sloshing cavity shown in Fig. 3.16, there is no RSE mirror but with a SRM. The right part shows the simplified mode coupling model. Figure taken from [1].

Intra-cavity filtering as a speed meter

In Fig. 3.19, we show the corresponding intra-filtering scheme. In terms of complexity, it is the same as the sloshing cavity scheme, but the sensitivity performance is different. As we will show, it has two interesting features. The *first* one is that it also has a speed response, and the characteristic frequency ω_s (up to which the speed response dominates) is given by

$$\omega_s = \frac{c\sqrt{T_{\rm ITM}T_s}}{2\sqrt{L_{\rm arm}L_s}} = \sqrt{\gamma_{\rm arm}\gamma_s}\,. \tag{3.55}$$

This differs from Eq. (3.48) by an extra factor of $\sqrt{T_{\rm ITM}}$ which is the transmissivity coefficient of the arm cavity ITMs. Thus, the sloshing frequency is determined by the compound mirror formed by the ITMs and the sloshing mirror. This feature makes it appealing in the sense that we can realise a speed meter with a relatively short sloshing cavity. For example, given the ITM transmittance $T_{\rm ITM} = 0.01$ and $T_s = 900$ppm, we can set the sloshing frequency around 100Hz for a 100m sloshing cavity. However, this would be very challenging for the speed

meter proposed in [57], in which case the sloshing mirror transmittance T_s needs to be 90ppm rather than 900 ppm given a 100m sloshing cavity. The *second* interesting feature is that it can also have a position response at low frequencies when the parameters are chosen properly. This can potentially provide a way to create a *Local Oscillator* (LO) for a practical readout scheme similar to the DC readout realisation described in [2].

To perform a detailed analysis of this scheme's quantum noise, one can use the standard input-output formalism by writing down the propagation equations for the fields and solve a set of linear equations in the frequency domain. Instead, here we will follow the approach in [65] by mapping parameters of the optics into several characteristic quantities, and using the narrow band approximation to define some effective modes. The advantage of this method is that it allows us to gain a clearer insight into the dynamics of the intra-cavity filtering scheme. We define: (i) c_a — the differential mode of the two arm cavities; (ii) c_b — the cavity mode inside the sloshing cavity; (iii) d — the external field; and (iv) ω_s, γ_a and γ_b — the characteristic frequencies for the coupling between c_a, c_b and d, as illustrated schematically in the right part of Fig. 3.19. These characteristic frequencies, ω_s, ω_a, ω_b, $\gamma_a$and γ_b, are related to the parameters of the optical components, which are shown explicitly in Appendix B.

We can then write down the Hamiltonian for the intra-cavity filtering scheme consisting of two optical modes and one test mass with reduced mass m, which reads:

$$\hat{\mathcal{H}} = \hat{\mathcal{H}}_0 + \hat{\mathcal{H}}_{\rm int} + \hat{\mathcal{H}}_{\rm ext} + \hat{\mathcal{H}}_{\rm GW}\,. \tag{3.56}$$

It contains four parts:

(i) The free Hamiltonian $\hat{\mathcal{H}}_0$ reads:

$$\hat{\mathcal{H}}_0 = \hbar\omega_a \hat{c}_a^\dagger \hat{c}_a + \hbar\omega_b \hat{c}_b^\dagger \hat{c}_b + \frac{\hat{p}^2}{2m}\,. \tag{3.57}$$

(ii) The interaction Hamiltonian $\hat{\mathcal{H}}_{\rm int}$ is

$$\hat{\mathcal{H}}_{\rm int} = \hbar G_a \hat{x} \hat{c}_a + \hbar \omega_s \hat{c}_a^\dagger \hat{c}_b + \text{H.C.}\,, \tag{3.58}$$

where 'H.C.' denotes the *Hermitian conjugate*. The first term represents the interaction between the cavity mode $\hat{c}_a$ and the test mass $\hat{x}$ via radiation pressure with $G_a = \omega_0 \bar{c}_a / L_{\rm arm}$ and $\bar{c}_a$ being the steady-state amplitude of $\hat{c}_a$ due to the coherent pumping of the laser. The second term describes the coupling between the two cavity modes with the coupling rate given by ω_s.

(iii) The interaction Hamiltonian $\hat{\mathcal{H}}_{\rm ext}$ between the cavity modes and the external field $\hat{d}$ reads

$$\hat{\mathcal{H}}_{\rm ext} = i\hbar(\sqrt{2\gamma_a}\,\hat{a}^\dagger + \sqrt{2\gamma_b}\,\hat{b}^\dagger)\hat{d}\,e^{-i\omega_0 t} + \text{H.C.}\,. \tag{3.59}$$

(iv) The energy $\hat{\mathcal{H}}_{\rm GW}$ from the interaction between the test mass and the GW tidal force $F_{\rm GW}$ is given by

$$\hat{\mathcal{H}}_{\rm GW} = -\hat{x}\,F_{\rm GW}\,. \tag{3.60}$$

Given the above Hamiltonian, we can obtain the corresponding equations of motion. Specifically, for the test mass, we obtain

$$m\ddot{\hat{x}} = \hat{F}_{\rm rad} + F_{\rm GW}\,, \tag{3.61}$$

with the radiation pressure force $\hat{F}_{\rm rad}$ defined as

$$\hat{F}_{\rm rad} \equiv -\hbar G_a(\hat{c}_a + \hat{c}_a^\dagger)\,. \tag{3.62}$$

For the cavity modes $\hat{c}_a$ and $\hat{c}_b$, we have

$$\dot{\hat{c}}_a + (\gamma_a + i\Delta_a)\hat{c}_a = -iG_a\hat{x} - i\omega_s\hat{c}_b + \sqrt{2\gamma_a}\,\hat{d}_{\rm in}\,, \tag{3.63}$$

$$\dot{\hat{c}}_b + (\gamma_b + i\Delta_b)\hat{c}_b = -i\omega_s\hat{c}_a + \sqrt{2\gamma_b}\,\hat{d}_{\rm in}\,. \tag{3.64}$$

The above detuning frequency $\Delta_{a,b}$ is defined as $\Delta_j \equiv \omega_j - \omega_0$ $(j = a, b)$. The interferometer output is related to the cavity modes through the standard input-output relation:

$$\hat{d}_{\rm out} = -\hat{d}_{\rm in} + \sqrt{2\gamma_a}\,\hat{c}_a + \sqrt{2\gamma_b}\,\hat{c}_b\,. \tag{3.65}$$

These equations can be solved in the frequency domain and are generally quite lengthy but straightforward. Here we focus on the tuned case of $\Delta_a = \Delta_b = 0$, which gives

$$\hat{c}_a = \frac{G_a(\Omega + i\gamma_b)\hat{x} + [\sqrt{2\gamma_a}(\gamma_b - i\Omega) - i\sqrt{2\gamma_b}\omega_s]\hat{d}_{\rm in}}{(\Omega + i\gamma_a)(\Omega + i\gamma_b) - \omega_s^2}\,, \tag{3.66}$$

$$\hat{c}_b = \frac{G_a\omega_s\hat{x} + [\sqrt{2\gamma_b}(\gamma_a - i\Omega) - i\sqrt{2\gamma_a}\omega_s]\hat{d}_{\rm in}}{(\Omega + i\gamma_a)(\Omega + i\gamma_b) - \omega_s^2}\,. \tag{3.67}$$

and the radiation pressure noise reads:

$$\hat{F}_{\rm rad} = \frac{2\hbar G_a[\sqrt{\gamma_a}(\gamma_b - i\Omega)\hat{d}_1 + \sqrt{\gamma_b}\omega_s\hat{d}_2]}{(\Omega + i\gamma_a)(\Omega + i\gamma_b) - \omega_s^2}\,, \tag{3.68}$$

with $\hat{d}_1 \equiv (\hat{d}_{\rm in} + \hat{d}_{\rm in}^\dagger)/\sqrt{2}$ and $\hat{d}_2 \equiv (\hat{d}_{\rm in} - \hat{d}_{\rm in}^\dagger)/\sqrt{2}i$.

The response to the test-mass displacement at the output reads:

$$\hat{d}_{\rm out}^{|x}(\Omega) = \frac{G_a[\sqrt{2\gamma_a}\,\Omega + \sqrt{2\gamma_b}(i\sqrt{\gamma_a\gamma_b} + \omega_s)]\hat{x}(\Omega)}{(\Omega + i\gamma_a)(\Omega + i\gamma_b) - \omega_s^2}\,. \tag{3.69}$$

As we can see, the first term in the bracket of the numerator is proportional to Ω, which gives the speed response, while the remaining term proportional to $\sqrt{\gamma_b}$ gives the linear displacement response. Therefore, it contains a mix of speed and displacement response. This is similar to the polarising Sagnac interferometer with an imperfect polarising beam splitter [2], and it implies that a potential local oscillator for a homodyne detection can be extracted. The turning frequency $\Omega_{\rm turn}$, at which the speed response becomes dominant, is given by (see Eq. (3.69)):

$$\Omega_{\rm turn} = \omega_s\sqrt{\frac{\gamma_b}{\gamma_a}}\,. \tag{3.70}$$

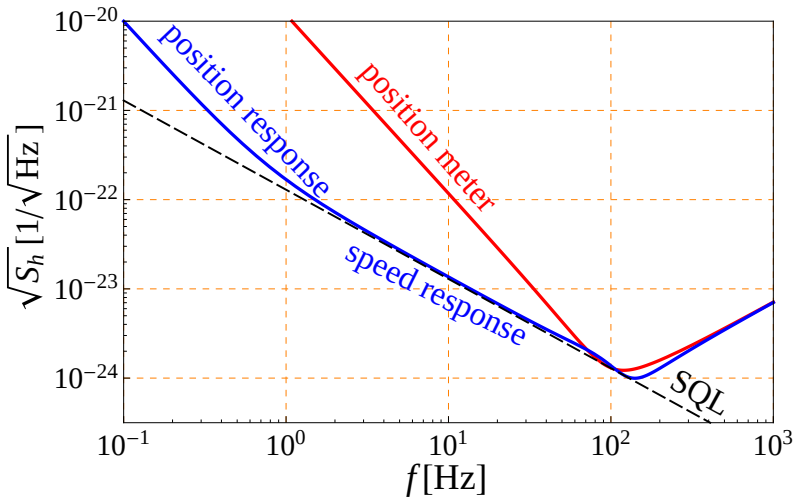

Figure 3.18.: The sensitivity curve for the intra-cavity filtering scheme (blue) in comparison with the usual position meter (red). There is a smooth transition from a position response to speed response. Figure taken from [1].

In the limit of $\gamma_b \to 0$, it approaches the speed meter

$$\hat{d}^{|x}_{\text{out}}(\Omega)|_{\gamma_b \to 0} = \frac{\sqrt{2\gamma_a}\, G_a\, \Omega}{\Omega^2 + i\gamma_a \Omega - \omega_s^2} \hat{x}(\Omega) \tag{3.71}$$

with a sloshing frequency given by Eq. (3.55) when the proper phase is chosen (see its definition in Eq. (B.9)).

In Fig. 3.18, we show the resulting sensitivity by choosing $\gamma_a/2\pi = \omega_s/2\pi = 100\,\text{Hz}$ and $\gamma_b/2\pi = 0.007\,\text{Hz}$ (blue). Indeed, at low frequencies the sensitivity curve is similar to that of a position meter (red) and it smoothly transits to the speed meter sensitivity in the intermediate frequencies. Given these parameters, the turning frequency Ω_{turn} is around 1 Hz which matches the blue curve.

These characteristic frequencies can be mapped to parameters for the optics by using their definitions in Eqs. (B.9) and (B.10) (Appendix B). We summarise these parameters in Table. 3.1. Two possible designs are presented in terms of including

Mirror [1]	With SRM	Without SRM
Sloshing mirror	0.0048 (0.0)	0.00080 (0.0)
ITM	0.012 (π)[2]	0.068 (π)
SRM	0.50 (0.0)	1.0 (0.0)

Table 3.1.: A table showing the power transmissivity (and the reflection phase) of relevant mirrors in the three-port-junction as shown in Fig. B.1 (Appendix B), resulting in the sensitivity (blue) in Fig. 3.18. The left column values refer to a model combining the SRM, the sloshing mirror, and the arm cavity ITMs. The righthand column values correspond to a design without the SRM, however, giving the same sensitivity. Here, optical losses are not considered.

the SRM or not. From the mirror parameters shown in Table. 3.1, we conclude that an intra-cavity filtering scheme could be implemented as an alternative speed meter without stringent design requirements. Meanwhile, a scheme in the absence of the SRM could also have a speed meter response, but this requires a high reflection sloshing mirror.

Figure 3.19 shows two equivalent intra-filtering speed meter schemes. Given the use of ideal optical components, they have the same performance as discussed (see Fig. 3.18). However, the schematic on the right-hand side may be a more practical implementation accounting for the complexity and control; and it is same as an input or output filtering scheme. Since a detailed design is beyond the scope of this work, in this thesis we do not distinguish them.

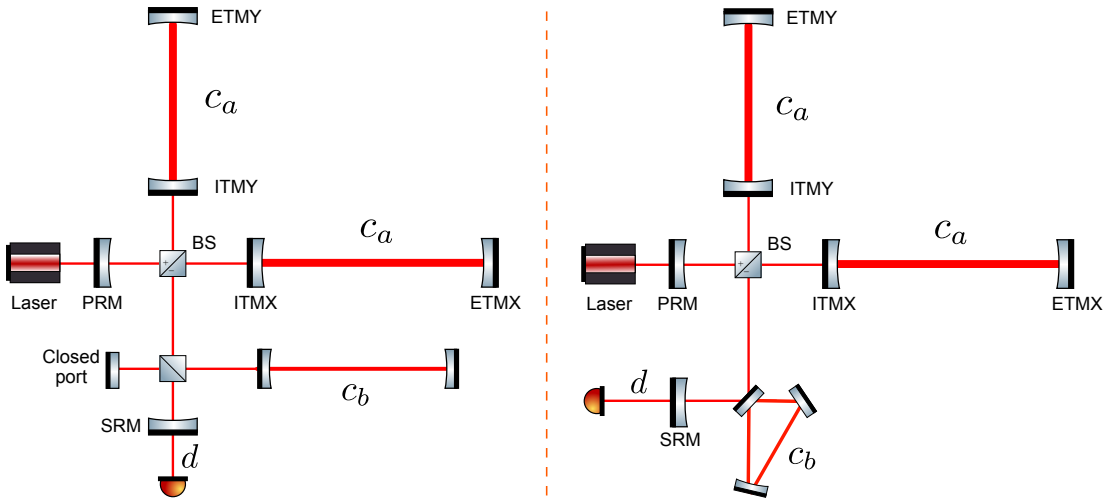

Figure 3.19.: Two equivalent intra-cavity filtering schemes as speed meter. Compared with the speed meter with a sloshing cavity shown in Fig. 3.16, there is no RSE mirror but a signal recycling mirror (SRM).

3.2.3. Case III: Achieving a Broadband Optimisation

In the previous two sections, we have been focusing our investigation on two specific intra-filtering schemes; both offer explicit analytical expressions that help to gain clear insights. However, these particular models cover only a small parameter space of all possible intra-cavity filtering schemes. In this section we present a numerical optimisation with the aim to maximise a certain cost function so as to evaluate the overall limits to the performance of this scheme.

For optimisation, we use the cost function introduced in [71] including realistic non-quantum noises (e.g., suspension and mirror coating thermal noise, etc):

$$\mathcal{C}(\boldsymbol{x}) = \left\{ \int_{f_{\rm min}}^{f_{\rm max}} \mathrm{d}(\log_{10} f)\, \log_{10} \left[\frac{h_{\rm ref}}{h_{\rm intra}(\boldsymbol{x})} \right] \right\}^{-1}, \tag{3.72}$$

where $[f_{\rm min},\, f_{\rm max}]$ is the frequency range of the optimisation; $\boldsymbol{x}$ is the set of optical parameters that can be tuned by the algorithm, in particular the parameters of the compound optics (including transmissivity and reflectivity of the filter cavity, the SRM, and the BS1); $h_{\rm ref}$ is the square root of the total noise spectral density

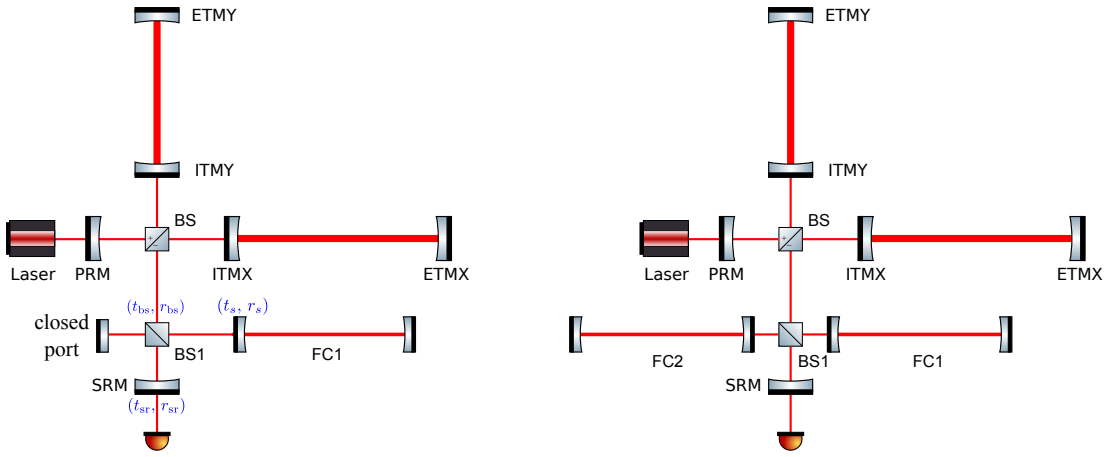

Figure 3.20.: The intra-cavity filtering schemes based on numerical optimisation based on one filter cavity and a closed port (left) and two filter cavities (right), using the cost function Eq. (3.72). Figure taken from [1].

Parameter	Lossless case	Lossy case
FC input mirror	0.0057 (0.0)	0.0090 (0.0)
SRM	0.040 (−0.045)	0.027 (−0.018)
BS1	0.25 (−0.017)	0.13 (−0.0032)

Table 3.2.: A table summarising the optimal power transmissivity (and the reflection phase) of the optics in the intra-cavity filtering scheme shown in Fig. 3.20 (left). The lossless values refer to an idealised model. The 30 ppm column provides parameters based on an optical loss at the mirrors of 30 ppm. The reflectivity coefficients are complex numbers indicating the phase shift of the propagation as shown in Fig. B.1.

(NSD) of a reference design (which can be the Advanced LIGO baseline design); and h_{intra} is the square root of the total NSD of the intra-cavity filtering scheme. We will maximise the results by integrating over $\log f$ instead of f.

We initially considered an intra-cavity filtering scheme with two optical cavities placed inside the signal recycling cavity as shown in the righthand side of Fig. 3.20, optimising the cost function based on the NSD of the Advanced LIGO design. However, the optimisation results suggested that a configuration as shown in the lefthand side of Fig. 3.20 with only one filter cavity is sufficient to achieve an equivalently good result. A scheme using one filter cavity will relieve the control requirement. Henceforth, we select the one filter cavity scheme to optimise. The outcomes of the optimisation are provided in Fig. 3.21, where the dashed black curve shows the NSD of Advanced LIGO as a reference [7, 72]. The optimised parameters are summarised in Table. 3.2. We found that an intra-cavity filtering scheme with one optical cavity placed inside the signal recycling cavity is able to improve quantum noise and we have compared the quantum noise of an ideal lossless case (green) with a model including 30 ppm mirror loss (blue). We found that optical losses degrade low-frequency quantum noise in the intra-filtering scheme and its loss susceptibility is similar to the input-filtering scheme which is shown as the red curve in the figure (for both schemes, the filter cavity length is assumed to be 100 m).

3.3. Conclusion

Previous work has shown that quantum noise can be reduced over a broad frequency band by modifying the input optics (input filtering) and output optics (output filtering) [54]. We showed the quantum noise performances when optical losses are taken into account. Optical losses degrade the low-frequency quantum noise of both filtering schemes, particularly the frequency-dependent readout. We have investigated an alternative filtering scheme — intra-cavity filtering, by placing an optical cavity inside the signal recycling cavity, as a practical imple-

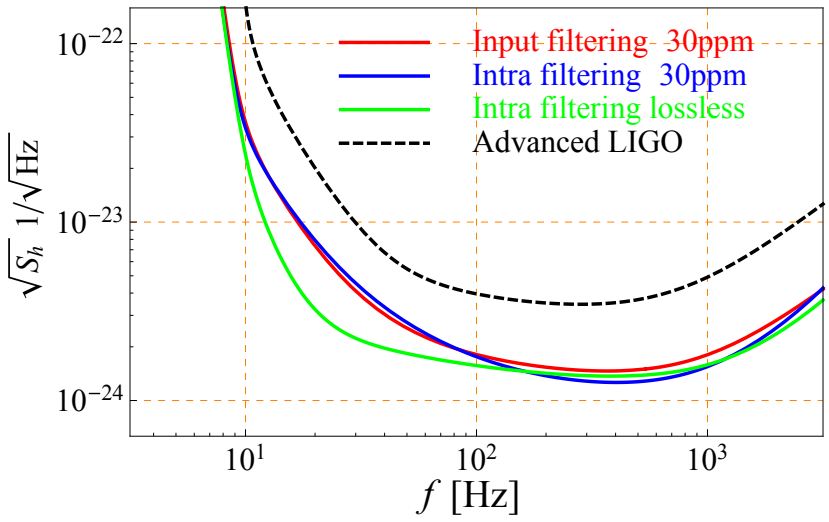

Figure 3.21.: Plot showing the numerically optimised quantum noise spectral density of an intra-cavity filtering (see Fig. 3.20 (left)). Figure taken from [1].

mentation for future GW detectors. This scheme has been analysed with three independent approaches with the aim to achieve a similar quantum noise suppression as predicted for input and output filtering schemes.

We first considered the intra-filtering as an alternative method to cancel the radiation pressure noise, hoping to reproduce the excellent low-frequency quantum noise performance realised by the ideal frequency-dependent readout. However, it turned out that the filter cavity produces a frequency-dependent phase shift that significantly reduce the sensitivity at intermediate frequencies. More explicitly, we have shown the resulting noise spectrum: (i) at low frequencies, is scaled as $\sqrt{T_{\rm sr}}/\Omega^2$, (ii) at intermediate frequencies as $1/(\Omega\sqrt{T_{\rm sr}})$, and (iii) at high frequencies as $\Omega/\sqrt{T_{\rm sr}}$.

We continued our investigation and considered the intra-filtering as a speed meter similar to the one proposed in [57, 64]. In our case, we considered a vertex formed

by the arm cavities, an intra-cavity and the SRM. Such a scheme, first of all, eases the stringent requirement of the sloshing cavity design presented in [57] as the bandwidth is not determined by the sloshing mirror only, but is now also related to the transmissivity of the arm cavity ITM (T_{ITM}). We found that due to the presence of the ITMs, the manufacturing requirement for the sloshing mirror can be relieved by a factor of $\sqrt{T_{\mathrm{ITM}}}$. We also found that the quantum noise of this scheme, at low frequencies, shows a position-meter-like response and then smoothly transits to a speed-meter response in the intermediate frequencies, given that proper parameters are chosen for the vertex components. We showed that by setting the coupling frequency of the arm cavities and the intra-filtering cavity to $\omega_s/2\pi = 100\,\mathrm{Hz}$, the decay characteristic frequency of the arm cavity to $\gamma_a/2\pi = 100\,\mathrm{Hz}$, and the decay characteristic frequency of the intra-filtering cavity to $\gamma_b/2\pi = 0.007\,\mathrm{Hz}$, the quantum noise of an intra-filtering was found to be that of a position meter response below 1 Hz and a speed meter response between 1 Hz and 100 Hz based on the Advanced LIGO baseline design.

The quantum noise behaviour of the intra-filtering varies when choosing different optical filters inside the signal recycling cavity. We presented a global optimisation of the intra-cavity filtering scheme based on one filter cavity, aiming at reducing quantum noise over a broad frequency band. This optimisation uses the Advanced LIGO sensitivity as a reference and takes into account classical noises such as seismic noise, suspension and mirror thermal noises. We showed that, with reasonable optical losses, for instance 30 ppm per mirror, the quantum noise of an intra-filtering scheme is comparable to the frequency-dependent squeezing, and so this scheme can be considered as an potential alternative.

Even though an intra-cavity filter scheme is not able to evade completely the radiation pressure noise, we found its implementation as a speed meter eases the tight requirements of the cavity design compared to a sloshing-cavity speed

meter. Meanwhile, its combination of position and speed response encourages future investigation of an intra-cavity filter scheme as a practical alternative for GW detectors. Additionally, the global optimisation of an intra-cavity filtering produced a similarly low quantum noise behaviour as the frequency-dependent squeezing.

Chapter 4.

Polarising Sagnac Interferometer for the Einstein Telescope

Future gravitational wave detectors, such as the Einstein Telescope, allows to implement new schemes to reduce the radiation pressure noise. A Sagnac interferometer is known to have very good low-frequency quantum noise performance [58]. In this chapter, we will investigate replacing the Einstein Telescope low-frequency interferometers by realistic polarising Sagnac interferometers. A practical DC readout scheme will be presented based on the polarising Sagnac topology. The core results have been presented in the recently published paper by Wang *et al* [Phys. Rev. D **87**, 096008 (2013)][2] and a number of figures with captions showing in this thesis are taken from this paper.

4.1. Brief Review

In this chapter we investigate the low-frequency quantum noise reduction for the large-scale GW observatory, Einstein Telescope (ET), replacing the low-frequency

Michelson interferometer by a polarising Sagnac interferometer. We will first briefly review the optical design of the ET and the basic features of a Sagnac interferometer, and then describe how to practically implement a polarising Sagnac topology with DC readout for the ET low-frequency interferometers.

4.1.1. The Einstein Telescope

The aim of the Einstein gravitational-wave Telescope (ET) project is the realisation of a third generation GW observatory in Europe with around a factor of 10 broadband sensitivity improvement with respect to the advanced detectors [73], e.g., Advanced LIGO [7] and Advanced VIRGO [74].

ET consists of three co-located detectors that are folded together into a triangular formation, each detector being formed by two Michelson interferometers (xylophone design [75, 76]), one for low-frequency gravitational waves (ET-LF) and one for high-frequency gravitational waves (ET-HF). ET therefore hosts six Michelson interferometers, all of which have 10km long arm cavities and use a dual- recycled Michelson configuration (see Fig. 1.4). ET-LF was proposed to optimise the sensitivity between 2-40 Hz, and the ET-HF is particularly concerned with high-frequency sensitivity from 40 Hz to 10 kHz by using high power lasers. Cryogenic technology will be employed in the ET-LF interferometers, so that relatively lower power laser beams are required.

From Fig. 1.7, we know that an optimal laser power results from a trade between the radiation pressure noise at low frequencies and the high-frequency shot noise. However, this limitation would no longer be a boundary for ET as its xylophone design allows the sensitivity optimisation for the ET-LF and the ET-HF independently. The ET-HF could employ high laser power to reduce the shot noise with no influence on the low-frequency interferometers; the ET-LF then offers

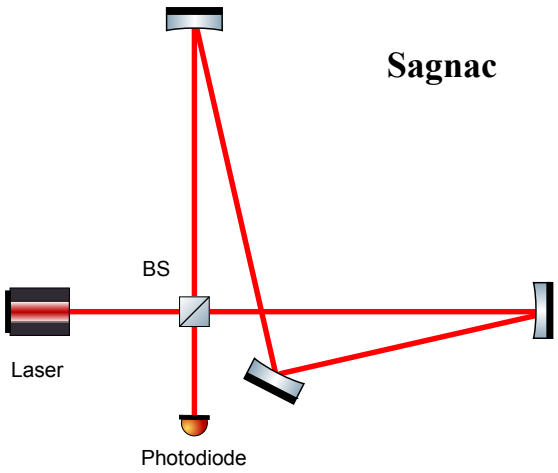

Figure 4.1.: A schematic of a Sagnac topology. A Sagnac interferometer employs optics in a manner that directs each beam after the central BS to propagate through both arms one after another but with opposite propagation directions.

the flexibility to apply different techniques to reduce the radiation pressure noise apart from the current input filtering design.

4.1.2. A Sagnac Topology and Possible Configuration for GW detectors

The ET design is not rigid and allows flexible choices of different topologies and optical layouts other than the current proposed dual-recycled Michelson interferometer. A Sagnac interferometer which is known to have a good low-frequency quantum noise performance [58] could be a possible implementation for the ET-LF interferometers. Compared to a Michelson topology (See Fig. 1.2) in which laser beams after the central beam splitter (BS) travel through each arm separately, a Sagnac interferometer employs optics in a way that direct each beam, after the central BS, propagating through both arms one after another but with

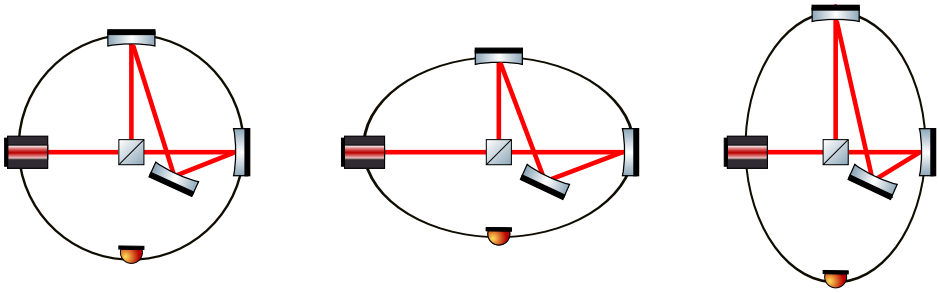

Figure 4.2.: Diagram showing the null-response of a Sagnac interferometer to a static displacement in arms. The dark fringe is independent of the mirror position.

opposite travelling directions, as shown in Fig. 4.1. Since the two beams share the same optical path, an important feature of a Sagnac topology shall be seen and has been illustrated in Fig. 4.2: it has no response to a static displacement in the arms. In fact, the Sagnac interferometer was initially proposed to measure rotation rather than mirror displacement [77]. This is one of the reasons why initially, the preferred topology design for interferometric measurements for GW detection was the Michelson interferometer as it is naturally suitable to 'see' GW signals (see Fig. 1.3). The Sagnac interferometer was not as appealing to the GW community, until a successful experimental measurement of a zero-area Sagnac showing that the Sagnac could be insensitive to rotation and potentially reach the required sensitivity to measure GW signals [78]. Later on, a Sagnac interferometer was found to function as a speed meter which has an excellent quantum noise (1 Hz - 100 Hz) behaviour [58] with only little susceptibility to optical losses, and since then the performance of a Sagnac interferometer for GW detection has been further explored [79, 80, 81].

Similar to a Michelson interferometer, a Sagnac interferometer can employ arm cavities, as well as the dual-recycling configuration (see Section 1.2.1). Currently, the two most promising Sagnac configurations for GW detection with a dual-

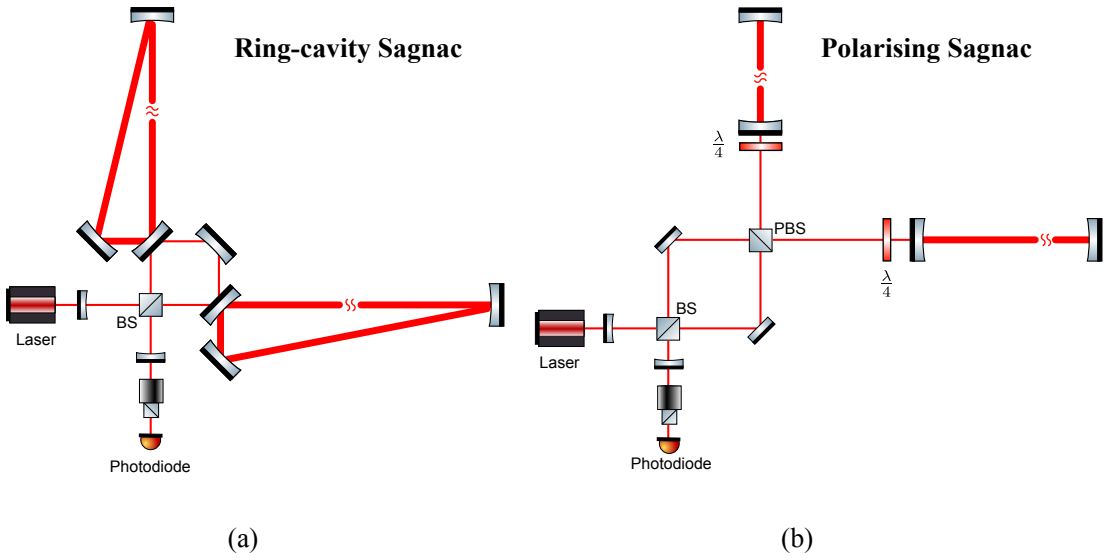

Figure 4.3.: Diagram showing two possible implementations for GW detectors with a Sagnac topology: (a) a ring-cavity Sagnac and (b) a polarising Sagnac. The polarising configuration has two linear Fabry-Pérot arm cavities with a length of several kilometers. A PBS transmits p-polarised and reflects s-polarised light. A QWP transforms the linearly polarised beam into a circularly polarised beam and vice versa with a rotated 90° angle relative to the initial linear polarisation.

recycled configuration and resonance cavities in the arms are shown in Fig. 4.3. The Sagnac, shown in Fig. 4.3(a), consisting of two ring cavities in the arms, is referred to as a *ring-cavity Saganc* [58]. The schematic on the right illustrates a Sagnac interferometer with minimum changes to the current Michelson infrastructure by using polarising optics: a polarising beamsplitter (PBS) and two quarter-wave plates (QWPs), and is referred to as a *polarising Sagnac* [79]. It is known already that a Sagnac interferometer using a unique angle squeezed vacuum injection (with no filter cavities added) can reduce the radiation pressure noise to a comparably low level as a Michelson interferometer with filter cavities (see the frequency-dependent squeezing input in Chapter 3). This has also been

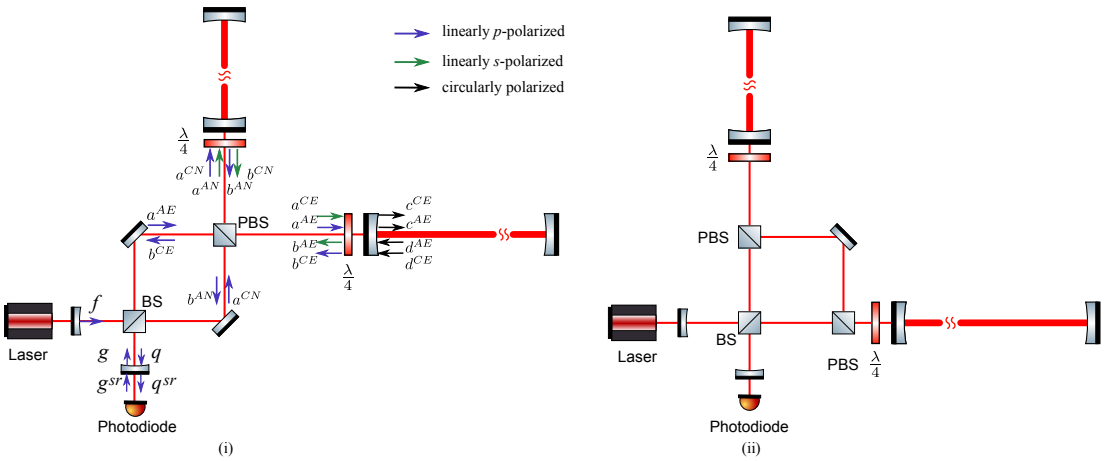

Figure 4.4.: Two versions of a polarising Sagnac interferometer configuration. Both require minimum changes to the current ET-LF Michelson interferometers; relevant parameters are summarised in Table 4.1. The left configuration which specifies each light field (i.e., a, b *etc*) will be used to evaluate the input-output relations in Section 4.3.1. The arrows denote the p-polarised (blue) and s-polarised (green) beams, which are respectively totally transmitted and reflected by an ideal PBS. Light fields circulating inside both arm cavities are circularly polarised beams (black) with both direction rotations. Figure taken from [2].

proven experimentally in a table-top setup by using a non-filtered squeezing input in a Sagnac interferometer [82].

Given the ET baseline being 10 km long, a ring-cavity Sagnac implies several potential issues, such as elliptical spot sizes on cavity mirrors and a larger small-angle scattering [79]. We therefore only focus our investigation on the polarising Sagnac. We can show that configurations (i) and (ii) in Fig. 4.4 will exhibit the same quantum noise performance if ideal and lossless optical components are considered. However, in reality each optical component is not perfect and will

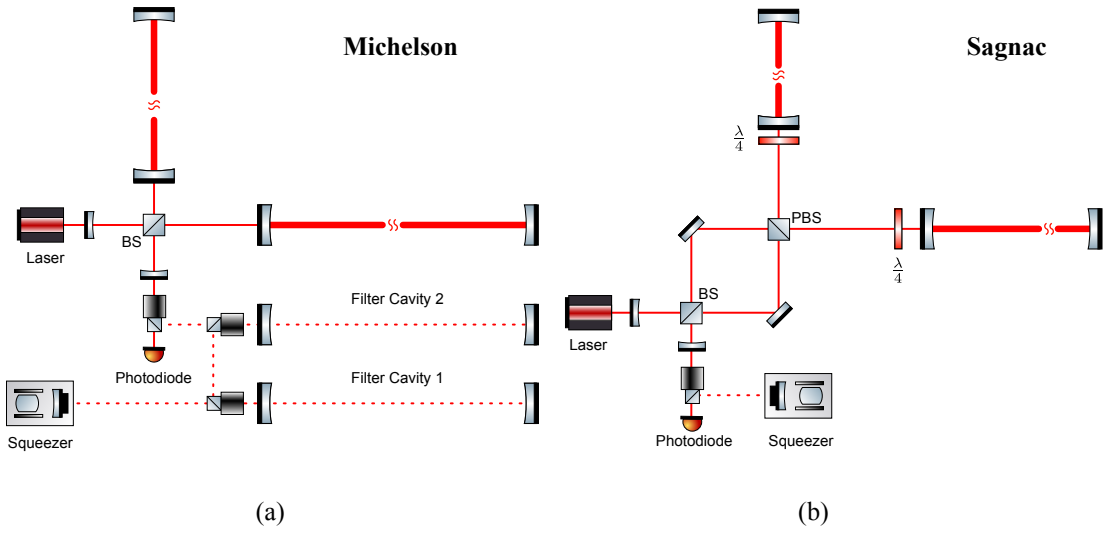

Figure 4.5.: Diagram comparing two topologies: (a) Michelson and (b) polarising Sagnac for the ET-LF interferometers. The Michelson interferometer with frequency-dependent squeezing is the current design as shown in [32] while the polarising Sagnac is based on the former layout but with minimum changes.

have to allow for imperfections, such as losses of optics and a *finite extinction ratio* of a PBS. From the schematics, we see that the main difference between these two configurations is the number of PBSs and their positions. Since configuration (i) employs only one PBS, we expect it to have lower optical losses due to the PBS finite extinction ratio, and therefore select it as the alternative to compare the quantum noise performance to the initial Michelson ET-LF interferometer, using two auxiliary filter cavities as shown in Fig. 4.5. It appears that a Sagnac interferometer reduces the complexity and in turn the costs for the construction of the ET significantly.

Parameter	Michelson	Sagnac
Arm length	10 km	10 km
Distance PRM-BS	10 m	10 m
Distance BS-ITM	300 m	300 m
Distance BS-PBS	-	10 m
Distance PBS-QWP	-	10 m
Distance QWP-ITM	-	280 m

Table 4.1.: A table summarising the baseline parameters of the ET-LF Michelson interferometer and an alternative Sagnac interferometer. The Michelson values are taken from the original design study report [32]. The Sagnac values are suggested by us for an ET Sagnac layout. Table taken from [2].

4.2. Realistic Polarising Sagnac Interferometer

We consider the polarising Sagnac interferometer in Fig. 4.4 (i) as an alternative for the ET-LF when imperfections of optical components are taken into account, in particular the finite extinction ratio of the PBS. We therefore analyse the quantum noise performance of such a realistic Sagnac interferometer with an imperfect PBS, assuming an extinction ratio being 1/1000 [83]. We propose the Sagnac interferometer baseline parameters with minimal but reasonable changes and summarise them in Table 4.1, considering that this ET Sagnac topology is compatible with the current ET-LF infrastructure.

An ideal PBS only transmits the p-polarised light field and reflects the s-polarised light field[1]. Quarter wave plates (QWPs) are used to transform the linearly po-

[1]We denote the component of the electric field parallel to the *incident plane* as p-polarised and the component perpendicular to the incident plane as s-polarised. Here, the incident plane

larised light field into a circular polarisation and again to transform the circularly polarised light field into a linearly polarised light field, rotated by 90° with respect to the initial linear polarisation. More specifically, a p-polarised beam is totally transmitted by an ideal PBS and then enters one arm. This beam will have passed through the QWP twice on its return to the PBS and so becomes s-polarised. This s-polarised beam is then reflected by the PBS and enters the second arm cavity (rather than transmitted back to the central BS). Transformed by the second QWP twice, it eventually returns back into its original p-polarisation at the PBS and interferes with the p-polarised beam in the opposite direction at the central BS. The interferometer will indicate any signals in the form of GW sidebands leave this interferometer at the dark port, detected by the photodiode.

4.3. Quantum noise of a Sagnac Interferometer

The quantum noise behaviour of a polarising Sagnac interferometer as shown in Fig. 4.4 (i) can be obtained following the similar procedure as we described in Section 2.4 for the Advanced LIGO (a Michelson topology). We will again use the block diagrams to achieve the input-output relation of a Sagnac interferometer, including the effects of the finite extinction ratio of the PBS. We start our consideration from an ideal case in which the perfect PBS fully transmits a p-polarised beam and reflects a s-polarised beam. Based on this study, we then extend the polarising Sagnac model, taking into account the realistic finite extinction ratio of a PBS. Arm cavities optical losses are considered for both cases.

Note that, in this thesis, we only consider the resulting output mixing two polarised fields due to imperfection that a PBS has a finite extinction ratio, ignoring

is the plane made by the propagation direction and a vector perpendicular to the reflection surface.

the mixes resulting from other effects, such as the misaligned axes of the PBS and QWPs. The quantum noise analysis of a polarising Sagnac interferometer as shown in the following has been published in [2]. A complete analysis of such a polarised Sagnac interferometer considering imperfect wave plates has not yet been performed, however, we have estimated the effect in a preliminary calculation; a wave plate with the retardation accuracy of $< \lambda/500$ [84] will result in a smaller effect compared to a PBS with an extinction ratio around 1/1000 ($\sim$ a factor of 3 lower); the leakage from an imperfect quarter wave plate is not in a desired polarisation for the DC readout described in Sec. 4.4, but if this leakage would dominate the output, a suitable DC readout scheme can be achieved directly using this field as a local oscillator.

4.3.1. Polarising Sagnac Interferometer with Perfect PBS

A polarising Sagnac with an ideal PBS implies that, for the configuration as shown in Fig. 4.4 (i), only the p-polarised vacuum field enters the interferometer at the dark port when the input laser is p-polarised.

As introduced in Section 2.3, a complicated optical system can be divided into several subsystems and then be represented by combining the subsystem TFs. The polarising Sagnac interferometer (see Fig. 4.4 (i)) can therefore be split into several principal parts as shown by the blocks in Fig. 4.6, each block being a transfer function (TF). $\mathbf{M}_{\mathrm{arm}}$ is the TF of the arm cavity, $\mathbf{M}_{\mathrm{h}}$ is the GW signal TF and $\mathbf{M}_{\mathrm{n}}$ is the noise TF which is induced by optical losses [2]. They are corresponding to the TFs derived for a generic arm cavity ($\mathbf{M}_{\mathrm{cav}}$, and $\mathbf{H}_{\mathrm{cav}}$, and $\mathbf{N}_{\mathrm{cav}}$) as shown in Eq. (2.69) (also see Fig. 2.12). All the fields, i.e., g, a^{AE}, are denoted in the schematic as shown in Fig. 4.4 (i).

In order to achieve the quantum noise spectral density (NSD) (see Eq. (2.72)),

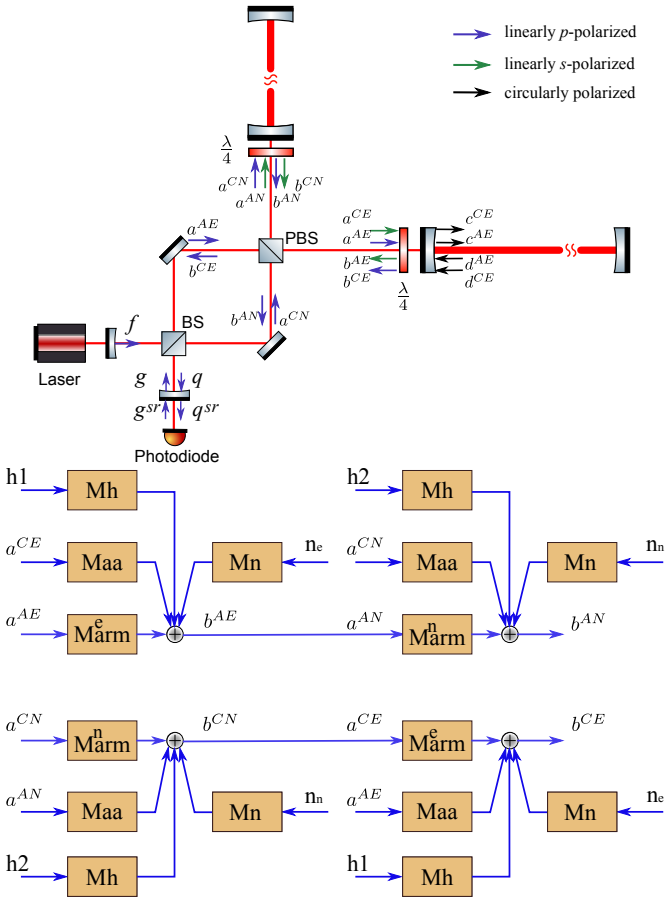

Figure 4.6.: Block diagrams of a polarising Sagnac interferometer. Each light field corresponds to that as shown in Fig. 4.4 (i) and each block follows the definition in Eq. (2.69). The mechanical displacements $x_{1,2}$ are due to the radiation pressure force of the light circulating in the cavities and the GW signals, and occur only at the end mirrors. Any light transmitted by the end mirror (EM) is considered as an optical loss. For a lossless cavity, $R_e = 1$, $T_e = 0$. QWPs are assumed to be perfect for polarisation rotation. Note that $\mathbf{M}^n_{\rm arm}$ is exactly the same as $\mathbf{M}^e_{\rm arm}$; the different subscripts simply indicate which light field enters which arm first. Figure taken from [2].

explicit input-output relation (between g and q) of this Sagnac interferometer are required. Following the travelling path of the input field g through such a polarising Sagnac interferometer, we can write down the input-output relation from Fig. 4.6. The junction equations of light fields at the central BS define the relations of the input vacuum field g and the output field q, the dimensionless GW strain h and additional optical losses induced quadrature n at the central BS as

$$\begin{aligned} g &= \frac{a^{AE} - a^{CN}}{\sqrt{2}}, \qquad & q &= \frac{b^{CE} - b^{AN}}{\sqrt{2}}, \\ h &= h_1 - h_2, & n &= \frac{n_e - n_n}{\sqrt{2}}, \end{aligned} \tag{4.1}$$

where the subscripts e, n in the noise fluctuations $n_{e,n}$ represent the origins of the optical losses from the horizontal arm and the vertical arm, respectively (conventionally, the *east* and the *north* arm). With these equations, we can deduce the relation between g and q (see Fig. 4.4 (i)) including optical losses [2]. From Fig. 4.6, we can write down

$$\begin{aligned} b^{CE} - b^{AN} &= \mathbf{M}_{\text{arm}}(a^{CE} - a^{AN}) + \mathbf{M}_{\text{aa}}(a^{AE} - a^{CN}) \\ &\quad + \mathbf{M}_{\text{h}}(h_1 - h_2) + \mathbf{M}_{\text{n}}(n_e - n_n), \\ &= \mathbf{M}_{\text{arm}}(a^{CE} - a^{AN}) + \sqrt{2}q \cdot \mathbf{M}_{\text{aa}} + h \cdot \mathbf{M}_{\text{h}} + \sqrt{2}n \cdot \mathbf{M}_{\text{n}}, \end{aligned} \tag{4.2}$$

and

$$\begin{aligned} a^{CE} - a^{AN} &= b^{CN} - b^{AE} \\ &= \mathbf{M}_{\text{arm}}(a^{CN} - a^{AE}) - \mathbf{M}_{\text{aa}}(a^{CE} - a^{AN}) \\ &\quad - \mathbf{M}_{\text{h}}(h_1 - h_2) - \mathbf{M}_{\text{n}}(n_e - n_n), \end{aligned} \tag{4.3}$$

[2] Optical losses of the arm cavities are again grouped into the transmission of the cavity ETMs as we have assumed for a Michelson interferometer as shown in Section 2.4.2.

where $\mathbf{M}_{\rm arm}$, $\mathbf{M}_{\rm h}$ and $\mathbf{M}_{\rm n}$ are defined in Eqs. (2.68) and (2.69), and

$$\mathbf{M}_{\rm aa} = e^{2i\phi_{arm}} \begin{bmatrix} 0 & 0 \\ -\kappa_{arm} & 0 \end{bmatrix}, \tag{4.4}$$

is induced by the two polarised fields circulating inside the arm cavities [2]. Solving Eq. (4.3), we then obtain

$$\begin{aligned} a^{CE} - a^{AN} =& \frac{1}{\mathbf{I} + \mathbf{M}_{\rm aa}} \left[\mathbf{M}_{\rm arm}(a^{CN} - a^{AE}) - \mathbf{M}_{\rm h}(h_1 - h_2) - \mathbf{M}_{\rm n}(n_e - n_n) \right], \\ =& \frac{1}{\mathbf{I} + \mathbf{M}_{\rm aa}} \left[-\sqrt{2} g \cdot \mathbf{M}_{\rm arm} - h \cdot \mathbf{M}_{\rm h} - \sqrt{2} n \cdot \mathbf{M}_{\rm n} \right]. \end{aligned} \tag{4.5}$$

Substituting the above equation into Eq. (4.2), we obtain the input-output relation of a Sagnac interferometer with a perfect PBS including the optical losses from the arm cavities as

$$q = \mathbf{M}_{\rm sag} g + \mathbf{H}_{\rm sag} h + \mathbf{N}_{\rm sag} n, \tag{4.6}$$

where

$$\begin{aligned} \mathbf{M}_{\rm sag} &= e^{2i\phi_{sag}} \begin{bmatrix} 1 & 0 \\ -\kappa_{sag} & 1 \end{bmatrix}, \qquad \mathbf{H}_{\rm sag} = e^{i\phi_{sag}} \frac{\sqrt{2\kappa_{sag}}}{h_{SQL}} \begin{bmatrix} 0 \\ 1 \end{bmatrix} \\ \mathbf{N}_{\rm sag} &= e^{i\phi_{sag}} \sqrt{T_e} \sqrt{\frac{\kappa_{sag}}{\kappa}} \begin{bmatrix} 1 & 0 \\ N & 1 \end{bmatrix}, \\ N &= e^{2i\phi_{arm}} \kappa_{arm} - e^{i\phi_{arm} - i\Omega\tau} \sqrt{\frac{\kappa \kappa_{arm}}{T_i}}. \end{aligned} \tag{4.7}$$

The above parameters follow the same definitions as in [58] and are defined as

$$\begin{aligned} \kappa_{arm} &= \frac{T_i \kappa}{1 - 2\sqrt{R_i}\cos(2\Omega\tau) + R_i}, \qquad h_{SQL} = \sqrt{\frac{8\hbar}{m\Omega^2 L^2}}, \\ \phi_{arm} &= \arctan\left(\frac{1 + \sqrt{R_i}}{1 - \sqrt{R_i}} \tan \Omega\tau \right), \quad \kappa = \frac{8 I_c \omega_0}{m c^2 \Omega^2}, \quad \tau = \frac{L}{c}, \\ \phi_{sag} &= 2\phi_{arm} + \frac{\pi}{2}, \qquad \kappa_{sag} = 4\kappa_{arm} \sin^2 \phi_{arm}, \end{aligned} \tag{4.8}$$

where h_{SQL} is the *Standard Quantum Limit* (SQL), R_i and T_i are the reflectivity and transmissivity of the arm cavity ITMs, I_c is the circulating power inside the

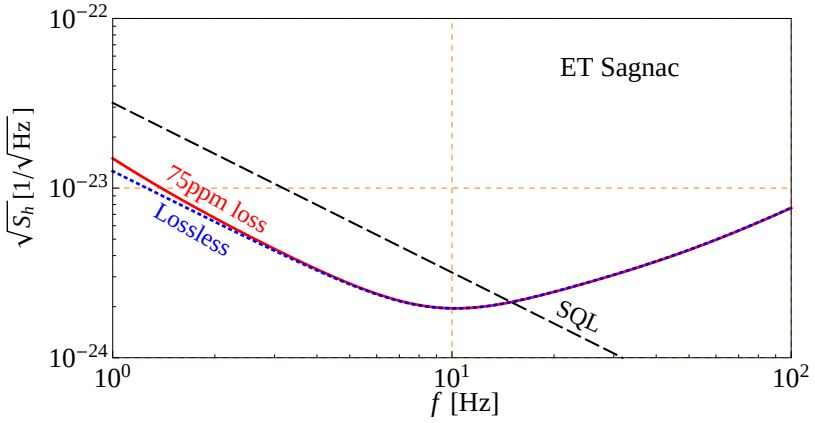

Figure 4.7.: Plots showing the quantum NSD of a polarising Sagnac interferometer with the original ET-LF Michelson parameters [32] (See Table 4.3): 10 km long arm cavities, 10 dB unique angle squeezing input and 18 kW cavity circulating power. The solid red line is the polarising Sagnac interferometer with the same cavity round-trip loss being considered, 75 ppm. The dotted blue plot shows the quantum noise spectrum of a perfect lossless polarising Sagnac interferometer. The dashed black line is the SQL defined by Eq. (4.8). It will be shown as a reference in all the NSD plots henceforth. Figure taken from [2].

arm cavities, L is the arm cavity length, ω_0 is the laser frequency, Ω is the GW signal angular frequency and m is the reduced mass of the TMs [2].

What we have achieved above is the input-output relation of a Sagnac interferometer without a SRM (see Eq. (4.6)). Now we consider the SRM to have the input-output relation between g^{sr} and q^{sr}. By substituting the non-signal-recycled Sagnac interferometer matrices and the SRM parameters into Eq. (2.61), we therefore can achieve the full input-output relations of a perfect Sagnac interferometer with dual-recycling configuration which is in agreement with [58]. Previous results have shown that the use of the SRM to reduce the high-frequency quantum noise comes at the cost of worsening the low-frequency sensitivity. How-

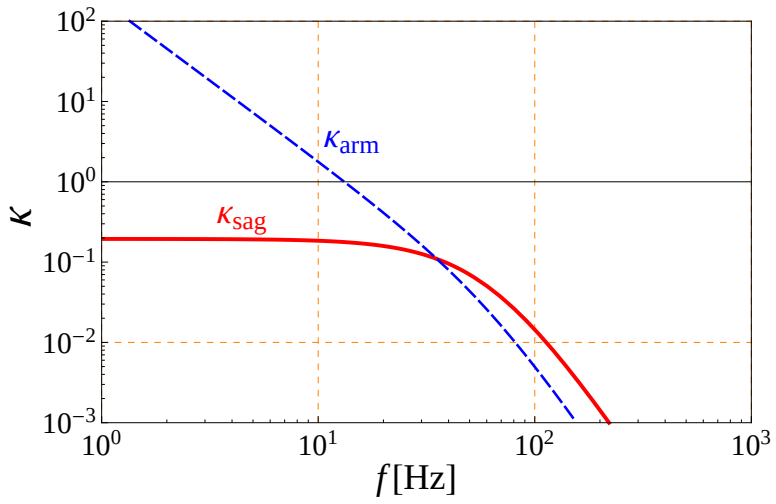

Figure 4.8.: Plots comparing the dimensionless κ between a Michelson interferometer ($\kappa_{\rm arm}$) and a Sagnac interferometer($\kappa_{\rm sag}$). The definitions are presented in Eq. 4.8.

ever, due to the xylophone design of the ET, the optimisation of the high frequency sensitivity [32] can be performed separately. The SRM for the ET-LF is no longer necessary. It is known that an interferometer without the signal recycling cavity will relieve the control difficulty.

Providing the input-output relation for a Sagnac interferometer with a perfect PBS, the quantum NSD yields (see the NSD definition in Eq. (2.72)):

$$S_h = \frac{e^{2r_p}(\cot\zeta - \kappa_{sag})^2 + e^{-2r_p}}{2\kappa_{sag}} h_{SQL}^2 + S_n, \tag{4.9}$$

where the term S_n comes from the optical losses and r_p is the squeezing factor (given perfect polarisers, only p-polarised fields are propagating through the Sagnac interferometer), i.e., a 10 dB phase squeezing corresponding to $r_p = 0.5 \ln 10$ (see Eqs. (3.2) and (3.6)). By applying the proposed ET-LF Michelson parameters [32] summarised in Table. 4.3 (noted as Michelson values), we obtain the sensitivity of a Sagnac-type ET given an ideal PBS and two QWPs. Figure 4.7 shows the quantum noise of such a Sagnac interferometer when a 75 ppm

round-trip loss from the arm cavities is taken into account. The lossless case is also given as a reference. In order to cancel the radiation pressure noise, the homodyne detection angle is set to

$$\zeta = \zeta_{opt} = \operatorname{arccot}\left(\kappa_{sag}|_{\Omega\to 0}\right), \tag{4.10}$$

according to Eq. (4.9) and the fact that low-frequency κ_{sag} is nearly a constant as shown in Fig. 4.8. A Sagnac interferometer therefore can naturally have an excellent low-frequency quantum noise performance by detecting at an optimal detection angle. Although the speed meter concept has yet to be experimentally proven, our investigation is still meaningful. It significantly reduces the complexity of the configuration as neither the two auxiliary filter cavities nor the SRM is needed (see Fig. 4.5).

We compare the quantum noise behaviour of an ET-LF Sagnac (solid curves) to that of the ET-LF Michelson (the brown dash-dotted curve), as shown in Fig. 4.9. While retaining all of the original ET-LF Michelson parameters, in particular with the same circulating power of 18 kW, the Sagnac interferometer achieves a better quantum noise behaviour below 5 Hz (magenta curve), and a worse peak sensitivity between 5 Hz and 30 Hz. This suggests that by further reducing other limiting noise sources, such as seismic noise, gravity gradient noise, and suspension and mirror coating thermal noise (see Section. 1.3.1), a Sagnac provides a better quantum-noise limited sensitivity below 5 Hz. Though the sensitivity at the frequency band from 5 Hz to 30 Hz is worse, this should be viewed in the context of a better low-frequency sensitivity and the much lower complexity of the Sagnac configuration (no filter cavities nor the SRM). Besides, we can potentially achieve a better peak sensitivity by increasing the laser power circulating inside the arm cavities as shown in Fig. 4.9 (the red and purple curves). This is because the peak level is determined by the shot noise which is inversely proportional to the laser power (see Eq. 1.10), while the low-frequency quantum noise is can-

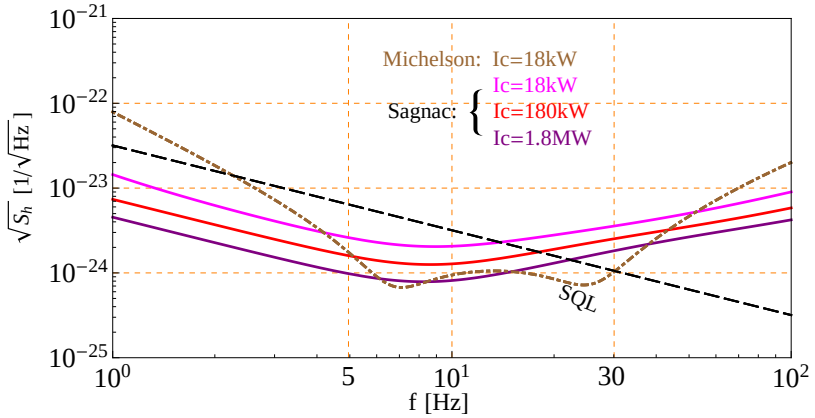

Figure 4.9.: Plots showing the quantum NSD of a lossless Sagnac interferometer with different powers circulating inside the arm cavities (I_c). The sensitivity peak is chosen around 10 Hz by adjusting the input power and the reflectivity of the cavity input mirror. The sensitivity curve for the ET-LF Michelson interferometer is shown as the dot-dashed brown line for comparison. Figure taken from [2].

celled out by setting the homodyne detection angle to the optimal value ζ_{opt} (see Eq. (4.10)) [2]. Note that the bandwidth of the arm cavities is simultaneously adjusted to optimise the sensitivity peak around 10 Hz by changing the reflectivity of the cavity ITMs. For different circulating powers, the values are summarised in Table 4.2.

However, due to the finite mirror absorption, an increase in the circulating power implies an increase of the mirror temperature and in turn increases the mirror thermal noise and suspension thermal noise. Based on the simple analytical model introduced in [32] (page 150-155), when the laser power is increased by a factor of 10, the mirror temperature would be doubled to approximately 20 K, which indicates a factor of $\sqrt{2}$ increase of the thermal noise. This level is still below the quantum-noise limit. A full optimisation is beyond the scope of this thesis, but further technical improvements would definitely be beneficial in the long term.

Cavity Circulating Power (I_c)	Cavity ITM Reflectivity (R_i)
18 kW	0.9818
180 kW	0.9712
1.8 MW	0.9531

Table 4.2.: A table summarising the reflectivity of the cavity ITM (R_i) for different laser powers (I_c) inside the Sagnac interferometer arm cavities.

4.3.2. Sagnac Interferometer with Imperfect PBS

A realistic configuration in our case will include the effects induced by the finite extinction ratio of the PBS. According to the state-of-the-art manufacturing quality, a PBS with $\eta_{p,s} = 1/1000$ for p-polarised field transmission and s-polarised field reflection is feasible. The relations of the fields at the PBS are

$$\begin{aligned}
e_s &= \sqrt{\eta_s}\cdot a_s + \sqrt{1-\eta_s}\cdot d_s, & e_p &= \sqrt{\eta_p}\cdot d_p + \sqrt{1-\eta_p}\cdot a_p,\\
f_s &= \sqrt{\eta_s}\cdot b_s + \sqrt{1-\eta_s}\cdot c_s, & f_p &= \sqrt{\eta_p}\cdot c_p + \sqrt{1-\eta_p}\cdot b_p,\\
g_s &= \sqrt{\eta_s}\cdot c_s + \sqrt{1-\eta_s}\cdot b_s, & g_p &= \sqrt{\eta_p}\cdot b_p + \sqrt{1-\eta_p}\cdot c_p,\\
h_s &= \sqrt{\eta_s}\cdot d_s + \sqrt{1-\eta_s}\cdot a_s, & h_p &= \sqrt{\eta_p}\cdot a_p + \sqrt{1-\eta_p}\cdot d_p,
\end{aligned} \tag{4.11}$$

with each field indicated in Fig. 4.10. The reflected p-polarised fields and transmitted s-polarised fields are also referred to as *leakages*. Given such a PBS in a polarising Sagnac interferometer, it results in an output that contains both orthogonally polarised fields, as shown in Fig. 4.11.

Again, in order to achieve the quantum noise behaviour, the input-output relation is significant. However, due to the effect of the realistic PBS with a finite extinction ratio, both the input and the output will contain s-polarised and p-polarised beams, and s-polarised and p-polarised vacuum fluctuations.

We have shown in Section 2.4.1 that the optical losses (i.e., absorption, scattering

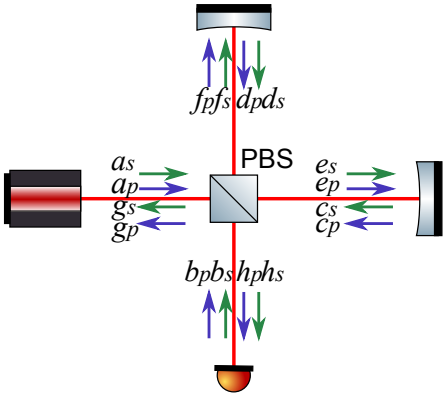

Figure 4.10.: Figure showing the relations of polarised light fields at the four ports of a PBS. Subscripts s and p represent the polarisation of each field. The arrows denote the p-polarised (blue) and s-polarised (green) beams. The PBS has an extinction ratio of η_p for the transmitted p-polarised beam and η_s for the reflected s-polarised beam. Figure taken from [2].

loss) at the BSs, including the central BS and PBS, are negligible. Therefore, we ignore the losses at the BSs but focus our attention on the leakage due to a finite extinction ratio. Note that loss effects from the arm cavities are still included. A similar block diagram as shown in Fig. 4.6 can be obtained as illustrated in Fig. 4.12 when an imperfect PBS with extinction ratios η_s and η_p is taken into account.

Since the block diagram is highly symmetric in terms of the propagation direction of the light fields, here we use the light field that first enters the vertical arm for example to represent the relations. The opposite field can be derived following the same procedure as demonstrated in Section 4.3.1. The conjunction equations at the central BS for both polarisations therefore can be extended from Eq. (4.1)

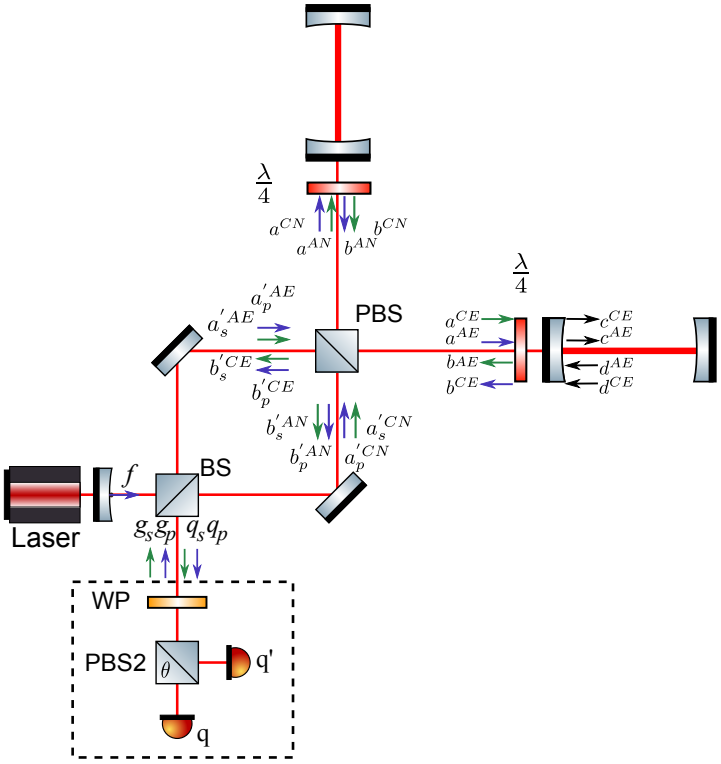

Figure 4.11.: Schematic of a polarising Sagnac interferometer with an imperfect PBS. The input beam is still purely p-polarised. The output has the coupled orthogonal s-polarised field due to the PBS imperfection. We also refer to this s-polarised field as the leakage from the PBS, which is the Michelson response. Homodyne detection is achieved as shown in the dashed box by using a wave plate (WP) and another PBS, which will be detailed in Section 4.4.4. A squeezed vacuum is injected at the detection port. Figure taken from [2].

into

$$g_p = \frac{a_p'^{AE} - a_p'^{CN}}{\sqrt{2}}, \qquad g_s = \frac{a_s'^{AE} - a_s'^{CN}}{\sqrt{2}},$$
$$q_p = \frac{b_p'^{CE} - b_p'^{AN}}{\sqrt{2}}, \qquad q_s = \frac{b_s'^{CE} - b_s'^{AN}}{\sqrt{2}}. \tag{4.12}$$

Reading from the block diagram illustrated in Fig. 4.12, we obtain the orthogo-

nally polarised output q_p and q_s as (up to the order of $\sqrt{\eta_p}$ and $\sqrt{\eta_s}$)[3],

$$\begin{aligned} q_p =&(-\sqrt{\eta_p}\mathbf{I} + \mathbf{M}_{\rm CLG}\mathbf{M}_{\rm sag})g_p + \sqrt{\eta_s}\mathbf{M}_{\rm CLG}\mathbf{M}_{\rm arm}g_s \\ &+ \mathbf{M}_{\rm CLG}\mathbf{H}_{\rm sag}h + \mathbf{M}_{\rm CLG}\mathbf{N}_{\rm sag}n\,, \end{aligned} \tag{4.13}$$

$$\begin{aligned} q_s =& -g_s + \sqrt{\eta_s}\mathbf{M}_{\rm CLG}\mathbf{M}_{\rm arm}g_p \\ &+ \sqrt{\eta_s}\mathbf{M}_{\rm CLG}\mathbf{H}_{\rm arm}h + \sqrt{\eta_s}\mathbf{M}_{\rm CLG}\mathbf{N}_{\rm arm}n\,, \end{aligned} \tag{4.14}$$

where the corresponding matrices and parameters are defined in Eqs. (4.7) and (4.8). The closed loop gain due to the leakages of the PBS with finite $\eta_{s,p}$ is given by

$$\mathbf{M}_{\rm CLG} = \left[\mathbf{I} - \sqrt{\eta_p(1-\eta_s)}\mathbf{M}_{\rm sag}\right]^{-1}, \tag{4.15}$$

which is approximate to an identity matrix $\mathbf{I}$ due to the small values of $\eta_{p,s} \ll 1$. We thus expect the influence to be negligible and the approximated input-output relation can be obtained as

$$q_p \approx \mathbf{M}_{\rm sag}g_p + \sqrt{\eta_s}\mathbf{M}_{\rm arm}g_s + \mathbf{H}_{\rm sag}h\,, \tag{4.16}$$

$$q_s \approx -g_s + \sqrt{\eta_s}\mathbf{M}_{\rm arm}g_p + \sqrt{\eta_s}\mathbf{H}_{\rm arm}h\,. \tag{4.17}$$

Two interesting results can be seen from these relations: (i) a unique polarised output (either q_p or q_s) contains both orthogonally polarised vacuum fluctuations (g_p and g_s). More specifically, for the p-polarised output (apart from a Sagnac response as the perfect case), it contains the s-polarised vacuum g_s which induces a radiation pressure noise that has the same frequency dependence as the one in a typical Michelson interferometer (see the $\mathbf{M}_{\rm arm}g_s$ term in Eq. (4.16)). The mixing of the Sagnac-type noise and the Michelson-type noise will degrade the low-frequency quantum noise of the Sagnac interferometer; (ii) the s-polarised

[3]Here, we keep the leading order up to $\sqrt{\eta_{p,s}}$, so that the main features of the Sagnac and Michelson response of both polarisations are maintained. Two complete equations are shown in Appendix C.

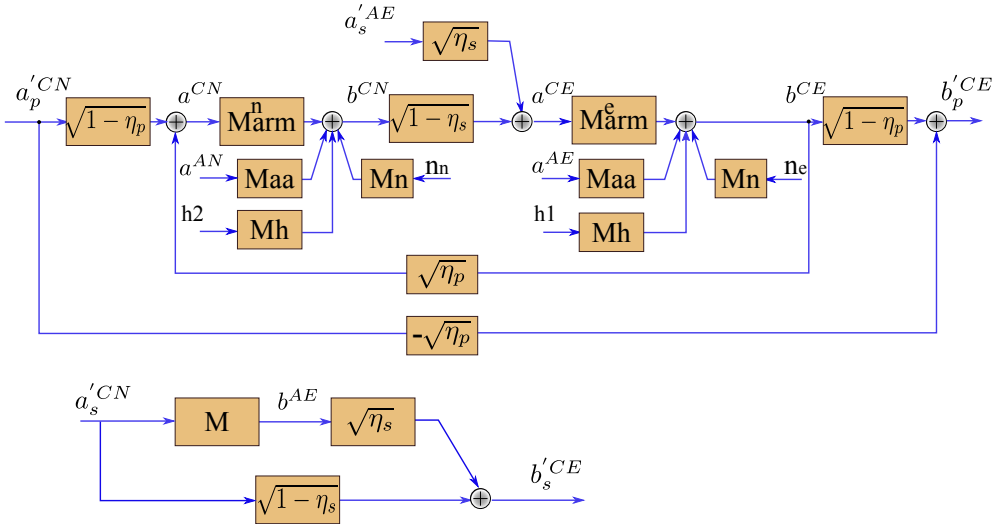

Figure 4.12.: A block diagram of a polarising Sagnac interferometer with finite extinction ratios $\eta_{p,s}$ of the PBS. Block $\mathbf{M}$ is defined as $\sqrt{\eta_s}\sqrt{\eta_p}\mathbf{M}_{\mathrm{CLG}}\mathbf{M}_{\mathrm{sag}}$ and the other blocks remain the same as the perfect case in Fig.4.6. A closed loop is formed due to the effective reflection leakage of the p-polarised beam. The output contains both polarisations. Figure taken from [2].

output shows a Michelson-type response (see the $\mathbf{H}_{\mathrm{arm}}h$ term) which can be used to create a local oscillator (LO) in a similar way as the DC readout scheme that will be implemented in Advanced LIGO (see Section 4.4). This is achieved by producing a small offset ΔL of the two arms (see Fig. 1.2 and Eq. (1.6))

$$q_s \approx -g_s + \sqrt{\eta_s}\mathbf{M}_{\mathrm{arm}}g_p + q_{\mathrm{LO}}, \tag{4.18}$$

with

$$q_{\mathrm{LO}} = \sqrt{\eta_s}\mathbf{H}_{\mathrm{arm}}\Delta L/L\,. \tag{4.19}$$

The two outputs are orthogonally polarised and so in order to mix them another PBS is employed to mix them at the output port, as shown schematically in the dashed box in Fig. 4.11. The output is adjustable by modifying the optical axis

of the PBS2. The resulting outputs therefore can be expressed in terms of the *detection ratio angle* θ (or referred to as the optical axis rotation angle) as

$$q^{\theta} = q_p \cos\theta + q_s \sin\theta\,, \tag{4.20}$$

$$q'^{\theta} = q_p \sin\theta + q_s \cos\theta\,. \tag{4.21}$$

By setting θ close to zero, the major response of q^{θ} is still the Sagnac signal and the term $q_s \sin\theta$ then provides the required LO. We will present the detailed readout scheme in Section 4.4. The relative phase difference between q_p and q_s determines the homodyne detection angle ζ. Due to the orthogonal polarisations, ζ can be tuned by defining the thickness of a wave plate (WP) before the PBS as shown in the dashed box of Fig. 4.11.

The final input-output relation (for small θ) therefore is given by

$$\begin{aligned} q &= q_1^{\theta}\cos\zeta + q_2^{\theta}\sin\zeta \\ &\approx (q_{p_1} + \theta\, q_{s_1})\cos\zeta + (q_{p_2} + \theta\, q_{s_2})\sin\zeta\,, \end{aligned} \tag{4.22}$$

and the quantum noise NSD of q is

$$\begin{aligned} S_h =& \frac{e^{2r_p}(\cot\zeta - \kappa_{sag})^2 + e^{-2r_p}}{2\kappa_{sag}} h_{SQL}^2 \\ &+ \frac{e^{2r_s}[(\sqrt{\eta_s}+\theta)\cot\zeta - \sqrt{\eta_s}\kappa_{arm}]^2 + e^{-2r_s}\theta^2}{2\kappa_{sag}} h_{SQL}^2\,, \end{aligned} \tag{4.23}$$

with r_p and r_s being the squeezing factors for the p-polarised and s-polarised input squeezed states, which can be different values. We find that (i) the term in the first line is the typical response of a Sagnac interferometer (see: Eq. (4.9)), and κ_{sag} is a constant at low frequencies (below the arm cavity bandwidth, see Fig. 4.8). By setting the correct homodyne detection angle ζ (see Eq. (4.10)), the radiation pressure noise can be removed; (ii) the term in the second line of Eq. (4.23) comes from the finite extinction ratio η_s and the non-zero detection ratio angle θ (for the DC readout). The low-frequency quantum performance is

Parameter	Michelson	Sagnac
Arm length (L)	10 km	10 km
Input Power (after IMC)	3 W	15 W
Input Power at BS	138 W	690 W
Arm Cavity Power (I_c)	18 kW	180 kW
Temperature	10 K	20 K
Mirror Mass	211 kg	211 kg
Laser Wavelength	1550 nm	1550 nm
SR Detuning Phase	0.6	-
SR Transmittance	20%	-
Filter Cavities	2 × 10 km	-
Squeezed Level	10 dB	±10 dB
Scatter loss per surface	37.5 ppm	37.5 ppm

Table 4.3.: A table summarising the parameters of ET-LF interferometers. The Michelson values are taken from the design study [32]. The Sagnac parameters proposed here refer to the high-power scenario with a circulating power of $I_c = 180\,\text{kW}$ which gives the sensitivity shown in Fig. 4.9. Table taken from [2].

worse due to the frequency dependence of $\kappa_{arm} \propto \Omega^{-2}$ as shown in Fig. 4.8. Its value is higher at lower frequencies. Smaller η_s and θ can help to improve the performance. However, the value η_s is determined by the quality of the PBS and the potential for improvement is small. The θ must not be too small to ensure the presence of a LO as we will shortly see in Section 4.4. Injecting an amplitude squeezed light for the s-polarisation, namely $r_s < 0$, has been recognised as an effective approach to minimise the influences.

With the expression of the quantum NSD of an imperfect polarising Sagnac in

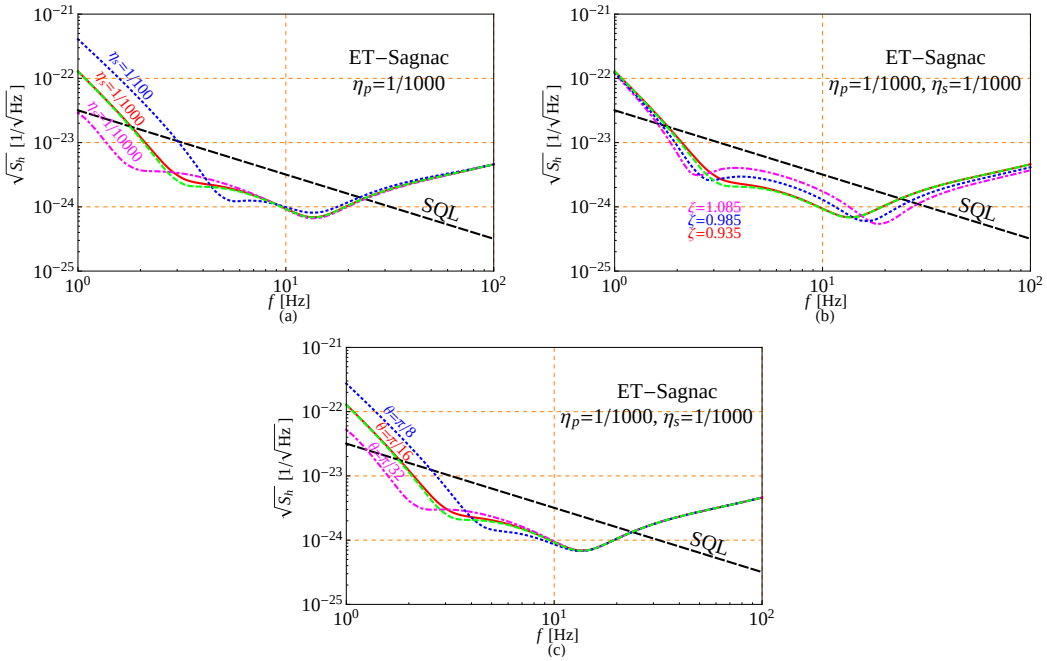

Figure 4.13.: Plots showing the quantum NSD of polarising Sagnac interferometers with different specifications for selected parameters. The configuration assumes the Sagnac interferometer parameters shown in Table. 4.3. All plots are based on a default parameter set with detection angle $\theta = \pi/16$, homodyne detection angle $\zeta = 0.935$ and $\eta_s = \eta_p = 1/1000$. Part (a) shows the impact of different extinction ratios η_s. η_p is fixed, as it has little influence on the final result. Part (b) illustrates a narrow band quantum noise mitigation via a homodyne detection angle selection. Part (c) shows the noise spectrum for different detection ratio angles. The dashed green curves in all plots, which are almost overlapped with the red curves (lossless Sagnac), illustrate the sensitivity of a lossy Sagnac interferometer when an arm cavity round-trip loss of 75 ppm is considered. Figure taken from [2].

Eq. (4.23), we investigate its performance when different parameters are selected. We show the results based on the ET-LF original design (apart from the factor of 10 power increase circulating in the arm cavity, $I_c = 180\,\mathrm{kW}$) summarised as Sagnac values in Table 4.3. Note that the qualitative characteristics are independent of the power levels. The reason to present the results with an increased power is because it is more suitable to show the limits of a potential practical Sagnac implementation for the ET-LF.

The quantum NSD results of an imperfect Sagnac are shown in Fig. 4.13 for various parameters. They have been published in [2]. In order to compare the quantum noise performances with different parameters, we use the red curve (see all the figures in Fig. 4.13) as a reference. It is based on the following parameter set: (1) the detection ratio angle $\theta = \pi/16$, (2) a homodyne detection angle $\zeta = 0.935$, (3) reasonable PBS extinction ratios $\eta_s = \eta_p = 1/1000$, and (4) a 10 dB phase squeezing for the p-polarisation, $r_p = 0.5 \ln 10$ and a 10 dB amplitude squeezing for the s-polarisation, $r_s = -0.5 \ln 10$. The dashed green curve shows the quantum noise sensitivity when 75 ppm arm cavity round-trip losses are included and is almost identical to the lossless red curve. This is due to the fact that the low-frequency quantum noise is covered by the Michelson-type noise. The optical losses thus have negligible influence on the sensitivity. In Fig. 4.13 (a), PBSs with different η_s are considered with $\eta_p = 1/1000$, the detection angle $\theta = \pi/16$, and the homodyne detection angle $\zeta = 0.935$. Figure 4.13 (b) shows the quantum noise behaviour by changing the homodyne detection angle ζ with $\eta_s = \eta_p = 1/1000$ and $\theta = \pi/16$. Figure 4.13 (c) gives the quantum noise sensitivity change in terms of the detection ratio θ. We have found that (I) the p-polarised transmission ratio has negligible impact on the quantum noise sensitivity but the performance is significantly influenced by the s-polarised reflection ratio, given both $\eta_{s,p} \ll 1\%$; (II) a narrow-band quantum noise mitigation can be

achieved by optimising the homodyne detection angle ζ; (III) a smaller θ, namely a smaller portion of the Michelson response at the output is preferable so as to have a lower level of quantum noise, as long as the minimum DC requirement for the DC readout is satisfied, which will be detailed in Section 4.4.

4.4. DC Readout

In this section we propose a new and practical readout scheme for the ET-LF with a realistic polarising Sagnac topology as shown in Fig. 4.11. As introduced in Section 1.2.1, the GW signals (with frequency $\Omega \sim$ kHz) create modulation sidebands upon the carrier field (with frequency $\omega_0 \sim 10^{15}$ Hz). The sidebands frequencies are therefore $\omega_0 \pm \Omega \approx \omega_0$, since $\omega_0 \gg \Omega$, and cannot be distinguished directly from the carrier field by a photodetector. Therefore, in order to extract the GW signal, a reference light, also referred to as a local oscillator (LO) field, is required to beat with the sidebands on the photodiode. A homodyne detection concept called DC readout is the current favourable readout scheme for GW detection [85, 86, 87]. This is due to the fact that the DC-readout LO light leaks from the interferometer, and thus is already pre-filtered by the large baseline interferometer; it is automatically on-axis and phase locked to the signal field [2].

For a Michelson interferometer, it is easy to achieve and control the amount of light field leakage into the detection port by setting an offset of the differential arm lengths. However, in an ideal Sagnac interferometer, the detection port is remaining on the dark fringe, regardless of the mirror position (see Fig. 4.2). In the following, we study how to implement a practical LO for the imperfect polarising Sagnac interferometer with DC readout (Section 4.4.4). In Section 4.4.1, we will present how to select and control the homodyne detection angle for such an interferometer based on the requirements we have briefly discussed in Section 4.3.2.

4.4.1. Required Light Level and Homodyne Detection Angle

In Section 4.3.2, assuming a perfect LO, we specified the optimal homodyne angle of the polarising Sagnac interferometer. In this section, we study how to achieve a practical LO to ensure the required homodyne detection.

There are several requirements of the LO in order to perform a desired DC-readout. First of all, the photodiode performance must be shot noise limited; the power of the LO should therefore be large enough to have the photodiode dark noise below the shot noise limit. Meanwhile, the power of the LO must dominate over the waste light due to higher order modes coupling into the dark port, as well as the stray light on the photodiode. Additionally, it must also have the correct homodyne phase [2]. It is known that the detected signal and the shot noise of the LO field both scale as the square root of the LO power. The exact light power required in the LO thus depends on the technical details of the interferometer implementation. It is reasonable to assume that the absolute value of the LO power is always satisfied (assuming that the stray light and photodiode dark noise is similar in a Michelson and Sagnac interferometer) and we only focus on the required ratio of the LO power to the circulation power at the central BS. Since the ET design has not yet reached such level of detail, we therefore use specifications for Advanced LIGO interferometers [85, 87] as guidelines, where the ratio of the power of the LO to central BS circulating power (which we call β) is 1.75×10^{-5}. In the following section, we focus our investigation on realisations of such a LO.

4.4.2. Non-50:50 Central BS Induced Imbalance

An easy way to have a leaked light field at the dark port is through the imbalance non-50:50 of the central BS. However, it is not difficult to notice that this field is

similar to the leakage of a Michelson interferometer due to an arm imbalance [88]. This creates a DC light field not being in a desired quadrature (orthogonal to the signal field); it thus cannot serve as a good reference light.

Below we consider two methods to achieve a LO light power in the Sagnac interferometer which is in the right quadrature: (i) non-zero Sagnac area and (ii) PBS leakage.

4.4.3. Sagnac Area Effect

The effective arm length difference due to a non-zero area $\mathbf{A}$ responds to Earth rotation Ω_{earth} is defined as

$$\Delta L = \frac{4\mathbf{A} \cdot \Omega_{\text{earth}}}{c}, \tag{4.24}$$

where c is the speed of light and ΔL is the same as shown in Eqs. (4.19) and (1.6). The ratio β therefore is

$$\beta = \sin^2\left(\frac{2\pi\Delta L}{\lambda}\right). \tag{4.25}$$

It gives reasonable units as

$$\beta = 1.75 \times 10^{-5} \left(\frac{A}{1350\,\text{m}^2}\right)^2 \left(\frac{1550\,\text{nm}}{\lambda}\right)^2 \left(\frac{\sin(\text{latitude})}{\sin(52^\circ)}\right)^2. \tag{4.26}$$

The above equation indicates that a $1350\,\text{m}^2$ area is required to have $\beta = 1.75 \times 10^{-5}$. For the ET, this would be feasible but probably costly due to the extra required underground cavern space.

Using this method, it is possible to obtain a required homodyne angle. However, it is suboptimal as it requires another 90° phase shift field to ensure the desired homodyne detection angle, usually via the arm imbalance (see Section 4.4.2). The homodyne angle therefore is determined by the ratio of the LO power created by

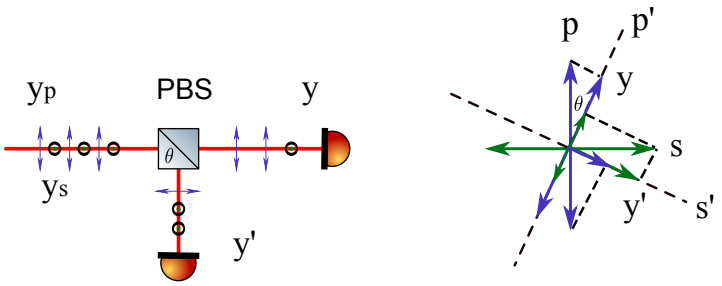

Figure 4.14.: Diagrams illustrating a scheme of the outputs of two orthogonal polarised beams with an optical axis rotated PBS. The input beams contain both polarisations: p-polarised beam (arrow) and s-polarised beam (circle). The left diagram shows the optical layout at the detection port; the right diagram illustrates the output details by rotating the PBS's polarisation axes (p-s) by an angle θ (p′-s′). Figure taken from [2].

the Sagnac area (fixed) to the light power due to an arm imbalanced (typically unknown prior to construction) [88]. Hence, we consider the PBS leakage generated LO detailed in the next section to be more practical [2].

4.4.4. PBS Leakage Light

As studied in Section 4.3.2, the s-polarised output due to the PBS leakage is a Michelson-type signal. In this section, we consider using this output as the LO.

A PBS with rotated polarisation axes combined the orthogonally polarised beams as illustrated in Fig. 4.14. Therefore, the output power can be adjusted with a rotation angle θ as

$$y = y_p \cos\theta + y_s \sin\theta, \tag{4.27}$$

$$y' = y_p \sin\theta + y_s \cos\theta. \tag{4.28}$$

From Section 4.3.2, we have known that the Michelson signal from the imperfect

polarising Sagnac interferometer is orthogonal to the Sagnac signal. The output power of the Michelson interferometer is η_s times of the Sagnac's. Figure 4.13(c) has specified that a smaller rotation angle θ is always preferable (much lower quantum noise). We can thus set this Michelson interferometer to bright the fringe and then send all of the power to the output as the LO (see Eq. (4.20)). The ratio β produced by the Michelson leakage is given by

$$\beta = \eta_s \sin^2\theta = 1.75 \times 10^{-5} \left(\frac{\eta_s}{0.001}\right) \left(\frac{\sin\theta}{0.13}\right)^2 . \tag{4.29}$$

Given $\eta_s = 1/1000$, we choose the minimum $\theta = \pi/24$ such that $\beta = 1.75 \times 10^{-5}$.

If the Michelson signal (s-polarisation) is used as a LO for DC readout, the homodyne detection angle ζ is determined by the relative phase difference between this LO and the Sagnac signal (p-polarisation). Since both the Michelson and Sagnac signals are the interferometer outputs, then in principle, they are naturally in-phase at the detection port (see q_s and q_p in Fig. 4.13). However, due to the orthogonal polarisations, a wave plate is able to shift the phase between them. The required homodyne detection angle is defined by the wave plate orientation and thickness. This well defined method to select the homodyne detection angle has obvious advantages compared to the Sagnac area approach presented in Section 4.4.3.

4.4.5. Potential Control of a Sagnac with PBS Leakage

We have shown in the above section that the output q (see Fig. 4.11) gives the readout signal, which is mainly a Sagnac response combining with a small fraction of Michelson response. It would be also interesting to investigate the other output q'. Preliminary results of using it as error signals for the interferometer control have been presented in [2]. This work has been carried out by Bond *et al* [4].

[4]The simulation results are modelled in FINESSE for this purpose.

4.5. Conclusion

In order to mitigate the low-frequency quantum noise, the proposed ET Michelson interferometers require auxiliary optical filter cavities to achieve the frequency-dependent squeezing. Such a configuration is more complicated compared to one without such extra optics. Additionally, the influence of optical losses from the input filter cavities will result in a quantum noise sensitivity degradation (see Chapter 3). We therefore studied a polarising Sagnac interferometer as an alternative to replace the low-frequency Michelson interferometers. Our scheme employs polarising optics (a PBS and two QWPs) to direct the beam whilst being compatible with the current ET infrastructure and avoiding the potential technical problems of long ring-shape arm cavities.

We found that by increasing the circulating power by a factor of 10 (which we deem feasible) a Sagnac interferometer without the filter cavities nor the SRM can achieve a similarly low level of quantum noise as a Michelson with filter cavities between 5 and 30 Hz; its sensitivity is even greater below 5 Hz. We also found that the influence of the expected ET round-trip losses is negligible in the frequency band we are concerned with.

We extended our model to consider an imperfect polarising Sagnac interferometer, in which the effects of a realistic PBS are included. We found that the effect induced by the PBS finite extinction ratio is described by the output mixing with the orthogonally polarised fields, each field containing both p-polarised and s-polarised vacuum fluctuations, respectively. The Sagnac signal is contained only in the p-polarised output while the Michelson signal is s-polarised. For the p-polarised output field, apart from the Sagnac-type response (signal and noise), the s-polarised vacuum fluctuations directly couple in and induce a noise that has the same frequency dependence as the one in a typical Michelson interferometer.

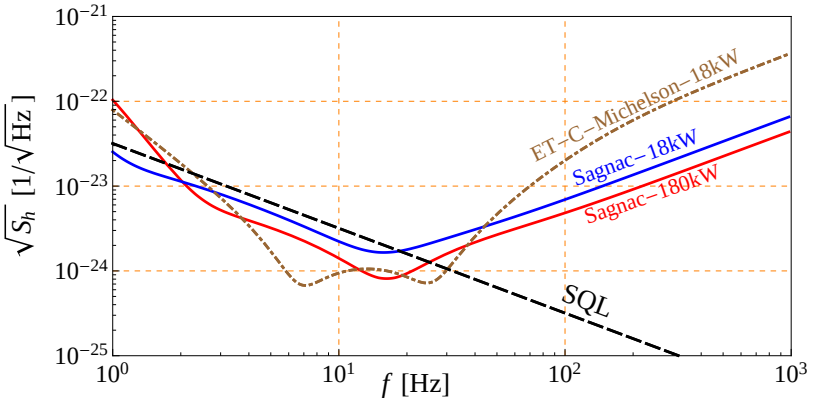

Figure 4.15.: Plots comparing the quantum NSD of the proposed Sagnac topology (blue curve) against the ET-C Michelson topology based on same ET-LF Michelson parameters (See Table. 4.3). The Sagnac topology uses parameters $\theta = \pi/24$, $\zeta = 0.935$ and $\eta_s = \eta_p = 1/1000$ to ensure a LO for DC readout. Both Sagnac curves include the effects of optical losses, and the ET-C curve shown here does not consider optical losses in the filter cavities. The red curve shows a Sagnac with a higher power, 180 kW, circulating in the arm cavities, which would be a possible implementation to increase the peak sensitivity. Figure taken from [2].

Since the quantum behaviour of the Michelson at low frequencies is worse than the Sagnac, this combination of the two signals results in a degraded sensitivity.

We presented the quantum noise sensitivity for a practical implementation for a polarising Sagnac interferometer. It uses a factor of 10 increased circulating power while otherwise retaining the original ET parameters. We considered a polarising Sagnac with the overlaid Michelson and found that the quantum noise behaviour is significantly influenced by the s-polarising extinction ratio η_s as this characterises the directly coupling of the Michelson response. In this case, optical losses rarely impact the quantum noise performance because the low-frequency

behaviour is dominated by the Michelson-type radiation pressure noise. A narrow-band sensitivity optimisation is available by carrying out a homodyne detection with optimal angle. We found that an imperfect Sagnac interferometer with a PBS with extinction ratios $\eta_s = \eta_p = 1/1000$ can achieve a low quantum noise curve comparable to that of a Michelson with filter cavities. Such an implementation offers greatly reduced complexity and reduced costs which occur with the auxiliary optics: two input filter cavities and the SRM. Advanced technologies, i.e., better suspensions and cryogenic mirrors, can easily be employed in such a topology.

The detector output of this imperfect polarising Sagnac interferometer contains two signals: a p-polarised Sagnac signal and a s-polarised Michelson signal. The DC-readout LO is achieved through the Michelson signal. We found that the low-frequency quantum noise can be further improved by reducing the Michelson signal present in the output, by means of reducing the detection ratio angle [2]. However, a minimum LO field is required for homodyne detection. By using the Advanced LIGO specification: the ratio of LO power to central BS circulating power 1.75×10^{-5} as a reference, we considered two approaches to achieve the required LO. We initially investigated a DC light generated by the non-zero Sagnac area response to the Earth rotation and found this to be impractical. It implies a large carven area given the original infrastructure and suboptimal homodyne detection angle selection. We showed that the LO provided by the non-perfect PBS is convenient and the homodyne detection angle can be easily set by means of using a wave plate to shift the phase between the Michelson signal and Sagnac signal.

The required LO level is achievable with realistic PBS extinction ratios and detection ratio angle. With a PBS extinction ratios of 1/1000, a detection ratio angle of $\pi/24$ was proposed to improve the radiation pressure noise. Figure 4.15 (blue

curve) shows the quantum noise behaviour of a polarising Sagnac interferometer, which retains all ET-LF Michelson parameters. A comparable sensitivity[5] to the ET-LF Michelson interferometer is shown in Fig. 4.15 (red curve) by using a circulating power of 180 kW power inside the arm cavities, which should be considered for its potential to further reduce the radiation pressure noise.

[5]If using the inspiral horizon distance for compact binary coalescences to assess the performances of the ET with two different topologies, we can quantitatively identify the sensitivity of the Sagnac interferometer and Michelson interferometer. Combining the ET-HF sensitivity given in [7], we achieve the detection range for two topologies as: Michelson-3351 Mpc and Sagnac-2739 Mpc based on Eq. (6) in [17]. Assuming the binary neuture star mergers are uniformly distributed in volume, this results in a lower detection rate when using the Sagnac topology would be lower by less than a factor of 2 relative to the Michelson. This indicates that the proposed Sagnac interferometer is indeed competitive and appealing for the Einstein Telescope.

Chapter 5.

Experimental Test of Cavity Loss

In order to enhance the sensitivity of future GW detectors, frequency-dependent squeezing may be implemented soon [89]. Due to optical losses, particularly from the filter cavity as presented in Chapter 3, the frequency-dependent readout is challenging with respect to a realistic implementation. The frequency-dependent squeezing scheme is indeed less sensitive to optical losses than several other possible schemes, but the minimisation of these losses is still the key challenge for an experimental realisation (see Fig. 3.9(a)). This also holds for the intra-cavity filtering scheme (see Fig. 3.21). The optical loss estimation of Fabry-Pérot cavities is therefore of great interest for all filtering schemes.

Previous work suggests that a longer filter cavity would have a lower total optical loss [55, 89], given that the cavity round-trip loss is fixed and independent from the cavity length. It is important to examine whether these two parameters are truly uncorrelated, particularly with realistic cavity mirrors, e.g., with a rough mirror surface [90], taken into account.

Filter cavities usually have a fixed bandwidth which is associated with the GW detector's detection band (see Section 3.1), for instance, the filter cavity band-

width of Advanced LIGO is around 100 Hz. As we will explain in the following sections, this means that the cavity finesse could be lower given a longer cavity length and vice versa. Since the total optical loss of a cavity is determined by a product of the cavity round-trip loss and its finesse, both the cavity length and the cavity finesse must be jointly optimised. More details will be presented in the following sections.

For a stable cavity, the beam spot sizes on the cavity mirrors are scaled to the cavity length. Usually, a longer cavity will accordingly have larger beam sizes on the cavity mirrors. The University of Birmingham group has carried out theoretical analysis into the light field coupling and scattering, considering the interactions between the optical fields and imperfect mirror surfaces [91, 92]. The simulation results presented in [92] indicate that the cavity round-trip loss is larger for larger beam sizes on cavity mirrors. In order to verify the relation between the cavity optical losses and the cavity length, we propose an experiment to characterise the optical losses of a length-varying linear impedance matched (ideally, $T_1 = T_2$) [93] Fabry-Pérot cavity with cavity finesse $\mathcal{F} \approx 2000$. The goal of this experiment is to observe cavity losses which are mainly due to scattering induced by distorted mirror surfaces.

In this chapter, we will describe the design and setting up of a table-top cavity aiming to evaluate the optical loss of a length-variable Fabry-Pérot cavity, with the cavity length being adjusted from 2 cm to 2 m. We will firstly illustrate our experimental design and then present our preliminary simulation results with three different real mirror surface distortions being considered. Finally, we present our preliminary results on the cavity optical losses characterisation. Two analytical models to estimate the cavity losses are provided, which could be directly used once the setup is ready. The results of this experiment aim to support the filter cavity development for future GW detectors.

5.1. Optical Loss in a Filter Cavity

The filter cavity bandwidth and the detuning frequency in Eqs. (3.24) and (3.26) indicate that the bandwidth γ of a filter cavity is almost fixed as it is required to provide an angular rotation over the detection band of the GW detectors (approximately 100 Hz for Advanced LIGO). Applied to the bandwidth definition in Eq. (A.6), this means the cavity free-spectral range (FSR) divided by the cavity finesse $\mathcal{F}$ reads

$$\gamma = \frac{\mathrm{FSR}}{\mathcal{F}} = \frac{c}{2L \cdot \mathcal{F}}\,. \tag{5.1}$$

This gives two possibilities for the installation of filter cavities in GW detectors: (i) a high finesse cavity with a relatively short cavity length, and (ii) a low finesse cavity but with a long length. In terms of practical difficulties and installation costs, the first option has obvious advantages, however, this has to be considered together with optical loss effects. A high finesse means a higher number of round-trips inside the cavity, resulting in a larger total optical loss [55]. Therefore, a trade-off between cavity finesse and cavity length drives our experimental investigation.

From Eq. (A.7), we know that the cavity finesse is defined by the reflectivities of its mirrors. In fact, the effective reflectivity is a function of the cavity round-trip loss

$$\mathcal{F} = \frac{2\pi}{T_1 + T_2 + \mathcal{E}_{\mathrm{rt}}}, \tag{5.2}$$

with $T_{1,2} = t_{1,2}^2$ and $\mathcal{E}_{\mathrm{rt}}$ being the cavity round-trip loss. Here optical losses are collected into the transmission of the EM as was done in Chapter 2. Therefore, the effective reflectivity of the EM is

$$r_2^{\mathrm{eff}} = \sqrt{1 - T_2 - \mathcal{E}_{\mathrm{rt}}}. \tag{5.3}$$

From Eq. (5.2), we know that the cavity round-trip loss can be characterised by means of estimating the cavity finesse.

Our test cavity consists of two mirrors with fixed radii of curvatures (RoCs). When the cavity length is varied, different spot sizes will be on both cavity mirrors given that the fundamental beam (Gaussian beam) is on resonance. We aim to see the change in cavity round-trip loss due to beam size changes and in turn have the cavity finesse change as a function of the cavity length.

We have designed a table-top experiment aiming to estimate the optical losses of a high finesse (2093) cavity as a function of cavity length. The reason for limiting the cavity finesse to roughly 2000 is due to practical control issues, as a cavity with a higher finesse is more difficult to control and is more susceptible to misalignment of the input beam [94] and a cavity with a lower finesse would have a non-measurable loss effect.

5.2. Cavity Design

In this section, we will further discuss the cavity parameters chosen for our experiment.

5.2.1. Mirror Radius of Curvature and Beam size

Given a cavity with a Gaussian beam wavefront curvature which perfectly matches the cavity mirror curvatures of the input mirror (Rc_i) and end mirror (Rc_e), we

have the beam spot sizes on the input mirror (IM) and the end mirror (EM) as

$$\omega_i(L, Rc_i, Rc_e) = \sqrt{\frac{\lambda L}{\pi}} \cdot \left[\frac{Rc_i^2(Rc_e - L)}{L(Rc_i - L)(Rc_i + Rc_e - L)}\right]^{\frac{1}{4}}, \tag{5.4}$$

$$\omega_e(L, Rc_i, Rc_e) = \sqrt{\frac{\lambda L}{\pi}} \cdot \left[\frac{Rc_e^2(Rc_i - L)}{L(Rc_e - L)(Rc_i + Rc_e - L)}\right]^{\frac{1}{4}}. \tag{5.5}$$

Or

$$w_i = \sqrt{\frac{\lambda L}{\pi}} \cdot \left[\frac{g_e}{g_i(1 - g_i g_e)}\right]^{\frac{1}{4}}, \qquad w_e = \sqrt{\frac{\lambda L}{\pi}} \cdot \left[\frac{g_i}{g_e(1 - g_i g_e)}\right]^{\frac{1}{4}}, \tag{5.6}$$

where the g factor is defined as $g = 1 - L/Rc$ and the stability criteria is given as

$$0 < g_i g_e < 1. \tag{5.7}$$

Combining this cavity stability requirement and Eq. (5.6), we know that the cavity configuration will be determined by the cavity mirror RoCs. Given the standard RoCs provided by common mirror manufacturers, three cavity configurations with feasible RoCs will give the largest beam spot on the cavity mirrors when the cavity maximum length is 2 m: (i) *concentric*, concave-concave cavity with $Rc_{i,e} = 1\,\mathrm{m}$, (ii) *hemispherical*, plane-concave cavity with $Rc_i = \infty$ and $Rc_e = 1\,\mathrm{m}$, and (iii) *hemispherical*, plane-concave cavity with $Rc_i = \infty$ and $Rc_e = 2\,\mathrm{m}$. The beam spot sizes over cavity length are shown in Fig. 5.1, where we assume there is a 0.001 m offset away from the unstable cavity position. For a concentric cavity, the beam waist is always at the centre of the symmetric cavity and the beam sizes on both mirrors are always identical. The beam sizes increase dramatically when the cavity is pushed towards an unstable position (when the cavity length approaches 2 m). However, for the hemispherical cavities, the beam waist is always sitting on the plane mirror (in our case, the IM) regardless of the cavity length. From Figs. 5.1(b) and 5.1(c), we notice that the beam size at the IM, does not vary much compared to the size change on the EM. Meanwhile, the beam sizes on the

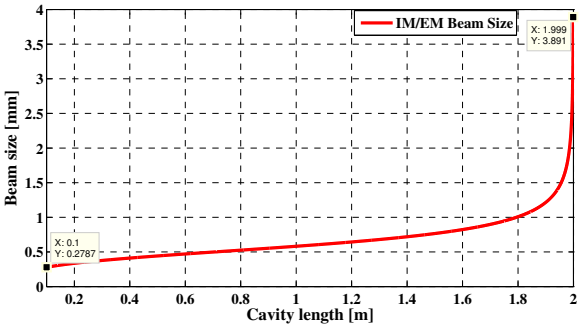

(a) Concentric concave-concave cavity with $R_{i,e} = 1\,\mathrm{m}$

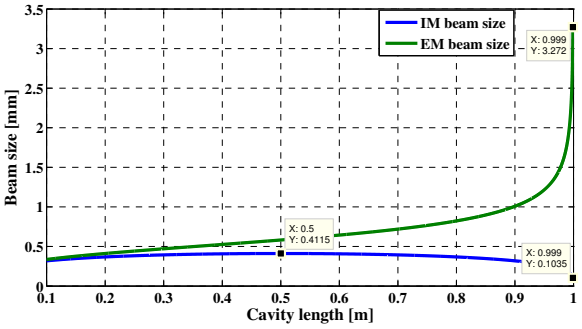

(b) Plane-concave cavity with $Rc_i = \infty$ and $Rc_e = 1\,\mathrm{m}$

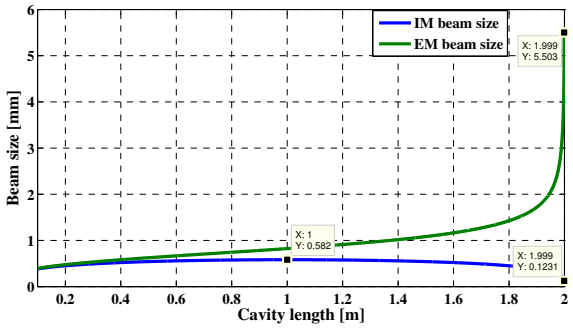

(c) Plane-concave cavity with $Rc_i = \infty$ and $Rc_e = 2\,\mathrm{m}$

Figure 5.1.: Diagrams showing the beam size changes on the cavity mirrors. (a) A concentric cavity with RoCs 1 m, (b) a hemispherical cavity with the IM being a plane mirror and the EM being a concave mirror with RoC 1 m, and (c) a hemispherical cavity which has a different EM with RoC=2 m. The laser wavelength is 1064 nm. The cavity length is varying up to its near-unstable position with an offset of 0.001 m.

EMs again will increase dramatically when the cavities are near-unstable. Given that the cavities are near unstable with only a 0.001 m offset, the hemispherical cavity with EM RoC=2 m is slightly better than the one with EM RoC=1 m in terms of achieving a larger beam spot. However, in view of the small difference between them (see the beam sizes in Figs. 5.1(b) (3.272 mm) and 5.1(c) (5.503 mm) when the cavity length is equal to 0.999 m and 1.999 m, respectively), in our experiment we will use mirrors with RoC=1 m for the time being.

5.2.2. Cavity Mirror Specifications

All the initial mirrors were ordered to have a reflectivity R of 0.9985, which corresponds to a design cavity finesse $\mathcal{F}_0 = 2093$. The reason for using an impedance matched cavity is simply because the same coatings can be applied to all mirrors at the same time. This will potentially reduce any surface differences induced by the coating procedure, and could also reduce costs. The mirror reflectivity is determined by the front surface coating. It is a high-reflection (HR) coating, using an ion-beam sputtering (IBS) process, for normal incidence with a wavelength of 1064 nm. The mirror rear surfaces (plane) are anti-reflection (AR) coated for 1064 nm.

Mirror substrates

In order to experimentally estimate the cavity finesse change as a function of cavity length, considering scattering losses due to mirror surface distortions, we perform the experiment applying mirror substrates with different qualities. In this section, we theoretically investigate their experimental realisation, which indicates measurable finesse differences.

Theoretical models predict that the losses are scaled to the beam spot size on the

Mirror	RoC [m]	Diameter × Thickness [inch]	Roughness [m]	Flatness
Plane-plane	∞	1" × 1/4"	< 1Å	$< \lambda/10$
Plane-concave CVI	1	1" × 1/4"	< 1Å	$< \lambda/10$
Plane-concave CO	1	1" × 1/4"	< 1Å	$< \lambda/10$

Table 5.1.: A table summarising the properties of the mirror substrates used in the measurement. Plane-plane substrates are manufactured at Coastline Optics (CO). Substrates with RoC=1 m are manufactured by two suppliers, CO and CVI. The flatness reference wavelength λ here is 633 nm.

cavity mirrors [92]. We therefore expect the optical losses due to the imperfect plane-plane mirror surface (IM) does not change significantly with increasing cavity length due to the very small change of beam size on the plane mirror (see Fig. 5.1). We investigate a hemispherical cavity for instance, using the same plane-plane mirror but with an EM of different surface qualities. The relevant properties of the plane-plane and plane-concave substrates are summarised in Table 5.1. Though they have the same property specification, the actual mirror surfaces are generally different from each other. For our experiment, we have initially ordered *four* mirror substrates: *one* plane-plane and *three* plane-concave (RoC=1 m). The plane-plane mirror and '1.0-FS' plane-concave mirror are from Coastline Optics [95] while the 'CVI1' and 'CVI2' are two plane-concave mirrors from CVI [96]. In the next section, we will represent the quality of these mirror substrates by using mirror surface maps.

Mirror maps of substrates before coating

We usually refer to a surface figure which gives the height of a surface as a *mirror map*. Mirror maps of the ordered mirror substrates before being coated are shown

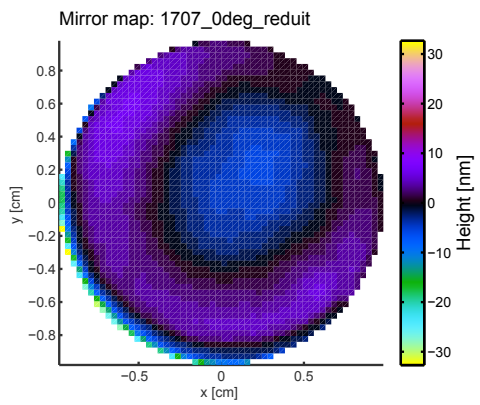

(a) Plane-plane mirror

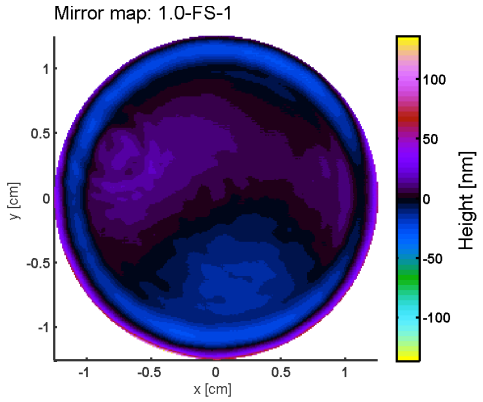

(b) Plane-concave mirror from Coastline Optics

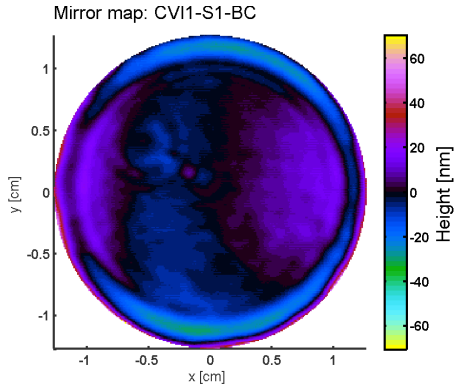

(c) Plan-concave mirror1 from CVI

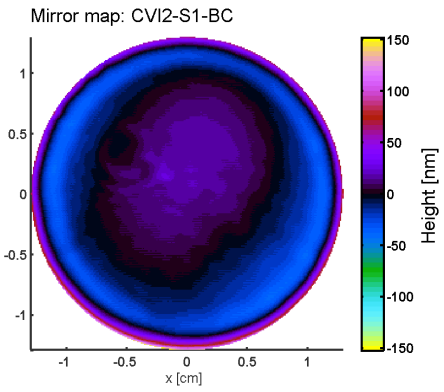

(d) Plan-concave mirror2 from CVI

Figure 5.2.: Diagrams showing the surface heights (mirror map) of different substrates before coating: (a) a plane- plane substrate, (b), (c) and (d) different plan-concave substrates with RoC of 1 m. (b) is from Coastline Optics, labelled as '1.0-FS'; (c) and (d) are from CVI, labelled as 'CVI1' and 'CVI2'. All the maps were produced using FINESSE guided by C. Bond.

in Fig. 5.2, which indicate the surface variations of different substrates. Note that the different scales shown in Fig. 5.2 does not directly associate with the surface quality since the scale could be determined by the high peaks at the edge which has negligible effects on the modes coupling [50]. These surface figures of different

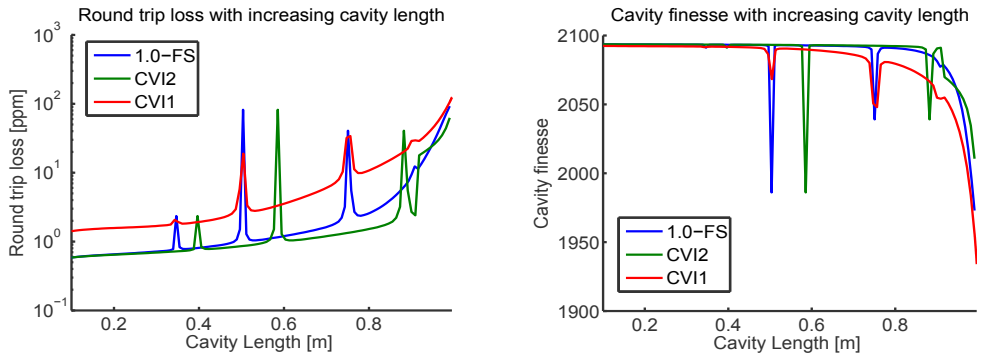

(a) (b)

Figure 5.3.: Plots showing a hemispherical cavity (a) round-trip loss and (b) finesse change over cavity length when realistic mirror maps are applied. The cavity IM has a surface distortion as described by Fig. 5.2 (a). The curves refer to the corresponding plane-concave mirror map ('1.0-FS', 'CVI1', and 'CVI2') shown in Fig. 5.2 (b), (c), and (d).

mirror substrates were measured using a Zygo interferometer by Coastline Optics. Mirror maps after coating are currently not available.

5.3. Simulation: Cavity Round-trip Loss

FINESSE [97, 98] is an advanced simulation tool for analysing higher-order modes in optical cavities with surface maps. Using FINESSE we are able to predict the cavity round-trip loss change as a function of cavity length when mirror surface distortions are considered.

We simulate a hemispherical cavity with the IM being a plane-plane mirror and the EM being a plane-concave mirror with RoC of 1 m. We consider that the IM has a surface figure as shown in Fig. 5.2(a) and apply the EM with three

different maps ('1.0-FS', 'CVI1', and 'CVI2') as shown in Figs. 5.2(b), 5.2(c) and 5.2(d) (note that the simulation result presented in [92] has a different focus.). The cavity round-trip loss can be defined by

$$\mathcal{E}_{\mathrm{rt}} = \frac{\mathcal{E}_{\mathrm{total}}}{\mathcal{F}_0/\pi}, \qquad \mathcal{F}_0 = 2093, \tag{5.8}$$

with $\mathcal{E}_{\mathrm{total}}$ being the total cavity losses which can be directly detected with the simulation and $\mathcal{F}_0$ being the design cavity finesse. Recalling Eq. (5.2), the change of the cavity finesse with increasing cavity length can be evaluated. Figure 5.3 shows the cavity round-trip loss and finesse change, respectively, as a function of the cavity length when different mirrors are used. Here, the peaks correspond to higher-order mode resonances when the cavity length fulfils their resonance condition.

The finesse changes in Fig. 5.3(b) indicate that the difference is quite small. For a cavity with a high-quality EM ('1.0-FS' or 'CVI2'), the finesse difference is smaller than 100. From the simulations, mirror CVI1 would provide the best chance to see the difference when the cavity is near-unstable, which gives a finesse variation of 160. Further investigation on a near-unstable cavity performance is required, but it is beyond the scope this thesis; this is a parallel project which has proposed in [92].

5.4. Proposed Experimental Setup

The existing infrastructure in the lab allows us to set up an experiment schematically shown in Fig. 5.4. The length-variable cavity is highlighted by the grey block and its length ranges from 2 cm to 2 m. We are using a solid-state laser (Innolight Mephisto Nd:YAG) which radiates a 1064 nm beam with very good mode purity and frequency stability. The Faraday isolator is used to prevent undesired

back scatters into the laser cavity. Wave plates, including quarter-wave plates ($\lambda/4$) and half-wave plates ($\lambda/2$) are applied to alter the polarisation of the light field as required. Lenses are used to modify the beam waist size and the position of a Gaussian beam to match the beam to the cavity eigenmode. An electro-optic modulator (EOM) phase modulates the light and provides radio-frequency sidebands to the laser beam. A triangular cavity, here referred to as a *mode cleaner* (MC), is used to improve the beam quality. Higher-order modes are not on resonance when the cavity is locked to the fundamental mode and thus will be significantly attenuated in transmission. The triangular mode-cleaner design is based on [99]. Two pairs of steering mirrors are placed before the mode-cleaner and the cavity of study to ensure proper mode matching and alignment.

For such a setup, the mode-cleaner has to be controlled and locked on resonance to the fundamental mode. The Pound-Drever-Hall (PDH) techniques [100] will be used for this purpose as shown in Fig. 5.5 (input part). The length-varying cavity is designed to provide longitudinal, tilt, and rotation motion controls. The former could be realised using the PDH technique, however the control of mirror tilt and rotation motion are more complicated: an auto-alignment control system will be implemented to adjust mirror tilt and rotation motions. This is based on a scheme called wavefront sensing technique, where two quadrant photodiodes (QPDs) monitor the exact beam pointing and extract output matrices [94, 101]. Three-axis piezo-electric transducers (or so called PZTs) are attached to the cavity mirrors to tune the mirror positions, tilts and rotations. All PZTs used in our experiment are from Physik Instrumente (PI) [102].

The experiment has been started from scratch, and the optical setup including all the electronic control loops are schematically shown in Fig. 5.5. The optical fields are detected by the photodiodes and converted into electronic signals. These auxiliary electronics boxes (Servo, High-voltage Amplifier (HV Amplifier), LO, and

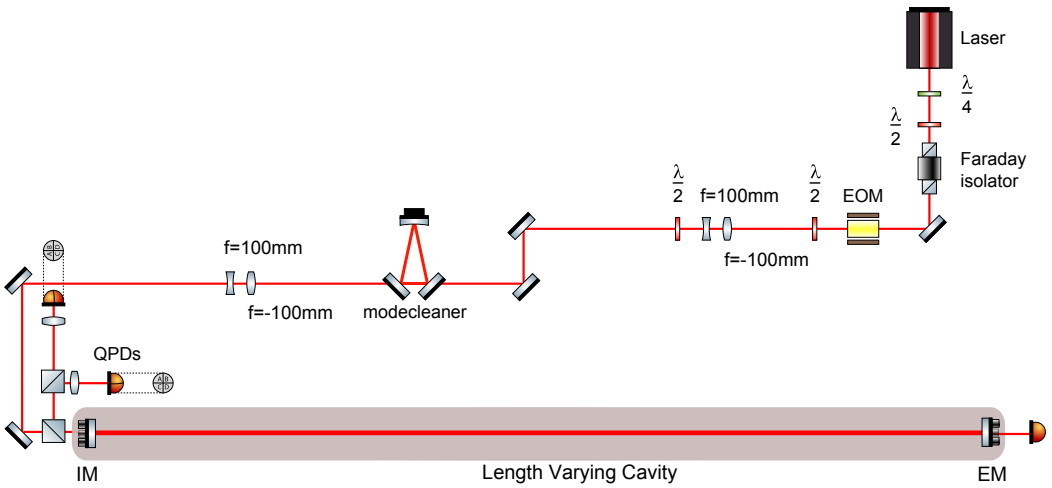

Figure 5.4.: A schematic showing a table-top setup to study optical losses of a length-varying cavity. A Nd:YAG laser radiates a 1064 nm beam. The Faraday isolator is used to prevent undesired back scatters into the laser cavity. $\lambda/4$ and $\lambda/2$ wave plates are applied to alter the polarisation of the light field as required. Lenses are used to modify the beam waist size and the position of the Gaussian beam. An electro-optic modulator (EOM) phase modulates and provides radio-frequency sidebands to the laser beam. A triangular cavity serves as a mode-cleaner to improve the beam quality.

Mixer) are used to perform the cavity control based on: the PDH technique and the auto-alignment technique. These boxes have been tested and characterised to support the followup experiment. For instance, the lowpass filters built in our lab are integrators (also referred to as 'Servo') with three cut-off frequencies and smooth variable gain options (see Fig.5.6).

The cavity with a finesse $\mathcal{F}_0 = 2093$ requires a laminar flow cabinet to prohibit contaminations (mainly dusts) on the mirrors as they will affect the cavity losses. The experimental setup is still under construction. In the following section, we will develop two methods for the cavity optical loss characterisation by using

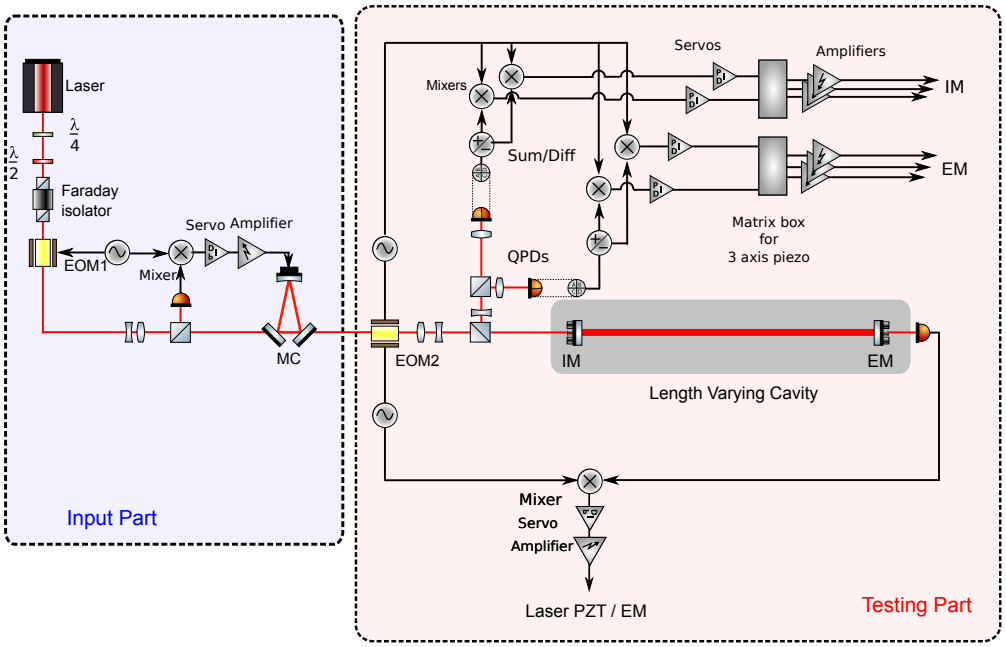

Figure 5.5.: A diagram showing cavity control of the setup illustrated in Fig. 5.4. The mode cleaner (MC) is a triangular cavity and locked to the laser by using PDH control, which includes a frequency mixer, a Servo—lowpass filtering, and a HV amplifier to drive a PZT attached to the MC. For the length-varying cavity, both longitudinal and angular control will be performed. The former will be based on the PDH technique whilst the latter is based on a wavefront sensing technique with two quadrant photodiodes (QPDs).

a rigid cavity, the MC as shown in the input part of Fig. 5.5, and show our preliminary results.

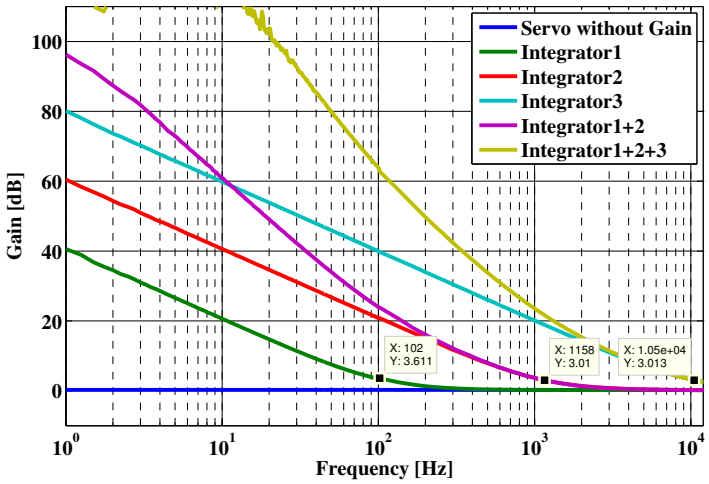

Figure 5.6.: A plot showing the measured TFs of our servo when integrators are on/off. The servo consists of three independent integrators with different cut-off frequencies (marked) and the gain of each integrator can be adjusted from -34 dB to 34 dB. These TFs are based on an original gain equal to 0.

5.5. Preliminary Results

Two optical loss estimation methods, (i) ring-down measurement and (ii) cavity pole measurement, have been carried out in the lab using the rigid triangular cavity (MC) shown in Fig. 5.5, to prepare the tools to perform the same cavity characterisations with the variable length cavity.

5.5.1. Ring-down Measurement

It has been demonstrated in [103] that the cavity finesse can be extracted by measuring the cavity reflection power (see Fig. A.1 field a_3) if the cavity is quickly scanned. The cavity power is excited when the cavity is on resonance and decays when one of the cavity mirrors moves away. It requires a cavity sweep in a time

of the order or less than the cavity storage time (see Eq. A.9).

We measured the reflection field by placing a photodiode at the reflection port when the MC is repeatedly scanned (see the input part in Fig. 5.5). Our measured data is captured by an oscilloscope (Agilent MSO7014B (7000 series)). In the following section, we will present the ring-down measurement in greater detail.

Analytical model

At an arbitrary time τ, the optical fields at different ports of a cavity (see Fig. A.1) are given by Eq. (A.3), and written as functions of time they become

$$
\begin{aligned}
&a_1(\tau) = a_1(0) = a_0, \qquad a_2(\tau) = \frac{r1 - (1 - r_1^2 - t_1^2) r_2 e^{-2ik(L_0+\tau c)}}{1 - r_1 r_2 e^{-2ik(L_0+\tau c)}} a_1(\tau),\\
&a_3(\tau) = \frac{it_1}{1 - r_1 r_2 e^{-2ik(L_0+\tau c)}} a_1(\tau), \quad a_4(\tau) = \frac{it_1 r_2 e^{-i2k(L_0+\tau c)}}{1 - r_1 r_2 e^{-2ik(L_0+\tau c)}} a_1(\tau),\\
&a_5(\tau) = \frac{it_1 e^{-ik(L_0+\tau c)}}{1 - r_1 r_2 e^{-2ik(L_0+\tau c)}} a_1(\tau), \quad a_6(\tau) = \frac{it_1 r_2 e^{-ik(L_0+\tau c)}}{1 - r_1 r_2 e^{-2ik(L_0+\tau c)}} a_1(\tau),\\
&a_7(\tau) = \frac{-t_1 t_2 e^{-ik(L_0+\tau c)}}{1 - r_1 r_2 e^{-2ik(L_0+\tau c)}} a_1(\tau),
\end{aligned} \tag{5.9}
$$

with L_0 being the original length of the cavity. Here an input a_1 is time-independent and we assume it is a constant a_0. These equations show optical fields in a steady state, from which we can deduce their changes in time series.

Assuming we start the cavity scan from its original position with cavity length L_0 and $\tau = 0$, this gives the initial values of each field as

$$
\begin{aligned}
&a_1(0) = a_1(\tau) = 1,\\
&a_2(0) = \frac{r1 - (1 - r_1^2 - t_1^2) r_2 e^{-2ikL_0}}{1 - r_1 r_2 e^{-2ikL_0}}, \qquad a_3(0) = \frac{it_1}{1 - r_1 r_2 e^{-2ikL_0}},\\
&a_4(0) = \frac{it_1 r_2 e^{-i2kL_0}}{1 - r_1 r_2 e^{-2ikL_0}}, \qquad a_5(0) = \frac{it_1 e^{-ikL_0}}{1 - r_1 r_2 e^{-2ikL_0}},\\
&a_6(0) = \frac{it_1 r_2 e^{-ikL_0}}{1 - r_1 r_2 e^{-2ikL_0}}, \qquad a_7(0) = \frac{-t_1 t_2 e^{-ikL_0}}{1 - r_1 r_2 e^{-2ikL_0}}.
\end{aligned} \tag{5.10}
$$

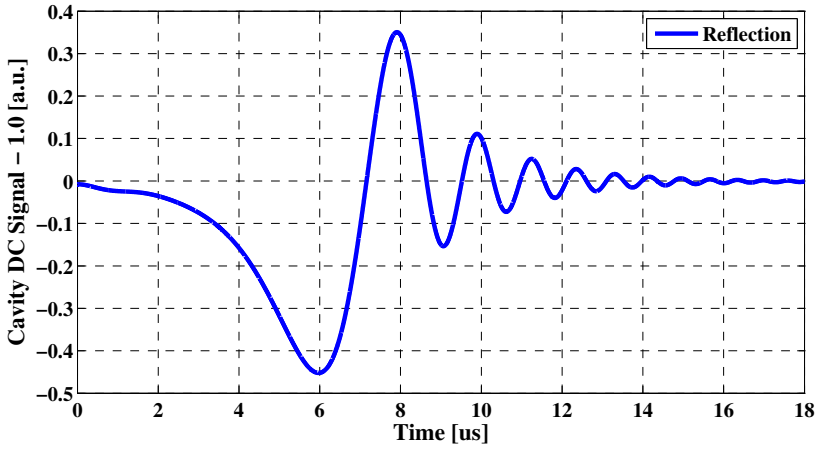

(a) Ring-down of power at reflection

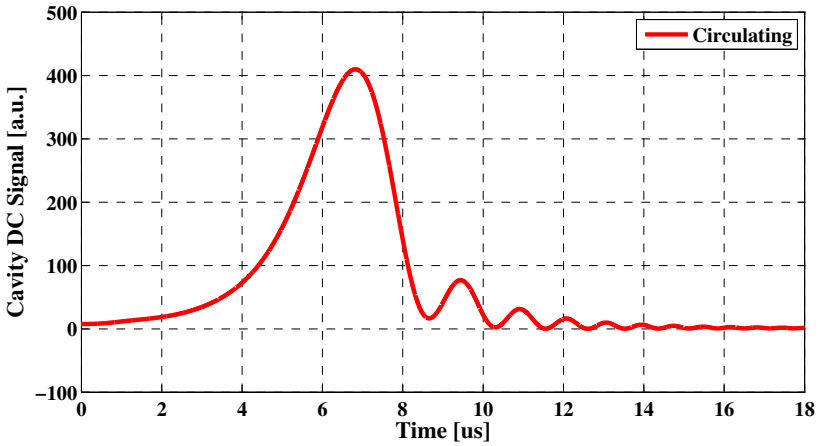

(b) Ring-down of power inside a cavity

Figure 5.7.: Plots showing analytical results of a ring-down power curve at (a) reflection and (b) inside a cavity. A constant input power 1 W is injected when the cavity is scanned with a speed around 250 um/s.

Consequently, at an arbitrary time $\tau = \tau_0 + n \cdot \tau_{\mathrm{rt}}$, we have (see Eq. (A.2))

$$a_1(n) = a_1(0) = a_0, \tag{5.11}$$

$$a_2(n) = a_4(n) i t_1 + a_1(n) r_1, \tag{5.12}$$

$$a_3(n) = a_1(n) r_1 + a_4(n) i t_1, \tag{5.13}$$

$$a_4(n) = a_3(n-1) r_2 e^{-ik(2L_0 + \tau_{\mathrm{rt}} \cdot v)}, \tag{5.14}$$

where the round-trip time $\tau_{\mathrm{rt}} = 2L_0/c$ is the time interval and v is the cavity scanning speed. Here, at a time $\tau = \tau_0 + n \cdot \tau_{\mathrm{rt}} (n \geq 1)$, $a_j(n), j = 1, ..., 7$ is used to represent the electric field $a_j(\tau)$, with $a_j(0)$ being the initial value.

Figure 5.7 shows the ringing shape of the reflection field a_2 and circulating field a_3, respectively, given a cavity is scanned at a speed of $v = 250\,\mathrm{um/s}$. We can see that our analytical results are in agreement with [104]. Since the cavity reflected power is much easier to obtain (placing a photodetector at the reflection port), we will measure and characterise the reflected power in our experiment only. By fitting the theoretical curve to the reflected power we recieve from the photodetector, we are able to extract the characteristic parameters of the cavity and in turn achieve the cavity finesse (including optical losses effects).

Results

We have used the MC to demonstrate the performance of this ring-down measurement (see the input part of Fig. 5.5). We measured the cavity ring-downs at the reflection port (a_2) for various scan speeds and two examples are shown in Fig. 5.8. A fitting function with variables: $v, T_1, T_2, \tau_{\mathrm{off}}$ and a_0 based on Eq. (5.14) was used to estimate the parameter set which gives a minimum variance between the measured reflection power (I_{data}) and the fitted analytical result (I_{fit}) as

$$f(v, T_1, T_2, \tau_{\mathrm{off}}, a_0) = \mathrm{Min}(I_{\mathrm{data}} - I_{\mathrm{fit}}), \tag{5.15}$$

with τ_{off} being the time offset from measurement.

We have repeated this ring-down measurement 100 times. A statistic error estimation can be achieved based on these measurements, and it shows that the cavity finesse standard deviation is around 1.36% and the measured finesse mean value is 6035. Extrapolating the characteristic result to a cavity with the desired finesse around 2000 implies the possibility to visualise the finesse change above

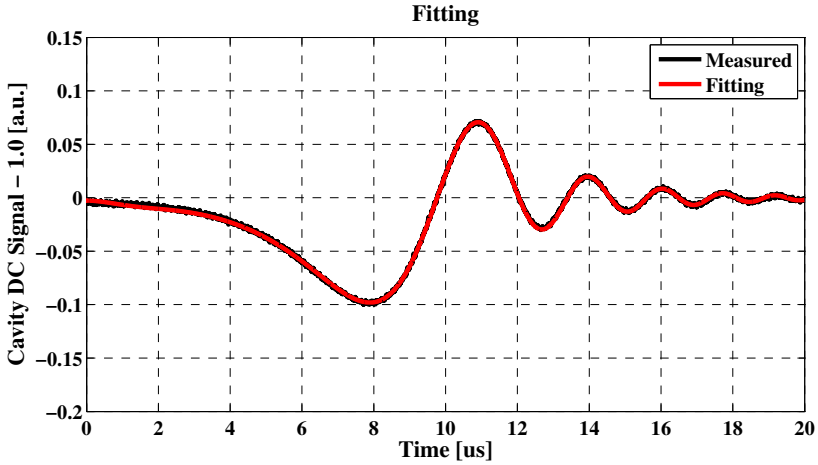

(a) Slow scan

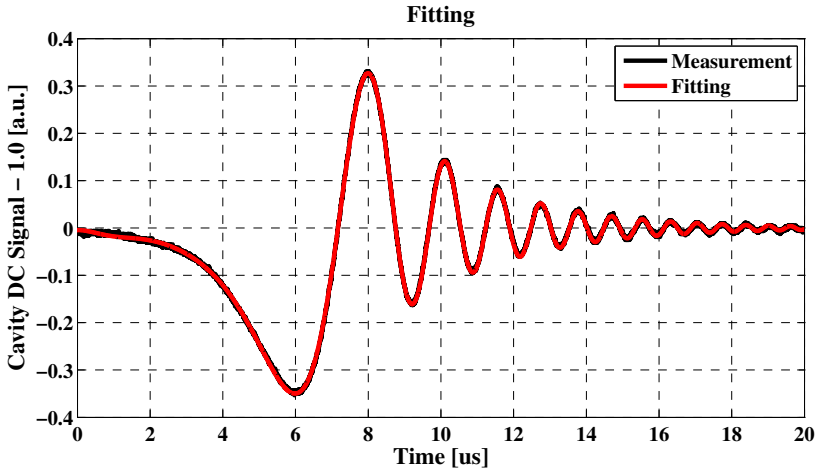

(b) Fast scan

Figure 5.8.: Plots showing the ring-down measurements and fitting data when a cavity is scanned at two different speeds: 100 um/s and 210 um/s. The fitting functions respectively give a cavity finesse of 5987 and 6138.

100. Combined with Fig. 5.3, we find that mirror 'CVI1' could provide a better chance to experimentally characterise the cavity finesse change.

It is worth mentioning that our cavity scan analysis is based on the assumption that a PZT applies linear displacement to the cavity mirror. However, in reality,

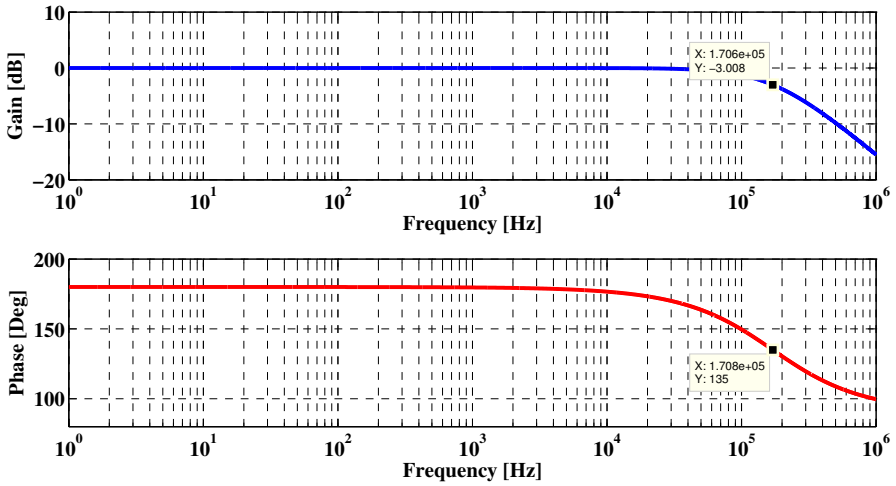

Figure 5.9.: Plots showing a cavity transfer function: (a) amplitude and (b) phase. The cavity length is 0.21 m and cavity finesse is 2093.

we found it is not the case. The nonlinear response of a PZT (observed in the lab and presented in [105]) will affect the absolute value of the finesse estimation. Future work will include the PZT calibration to improve the optical loss estimation precision but it is not the focus of this thesis.

5.5.2. Cavity Pole Measurement

A cavity has its own unique characteristic pole frequency which can be obtained from its frequency-dependent transfer function. Recalling Eq. (A.6), we know that the cavity pole frequency is defined as half of the cavity bandwidth. Therefore, it is possible to obtain the cavity finesse via a TF measurement.

Mathematical description

The transfer function G_c of a Fabry-Pérot cavity as shown in Fig. A.1 can be expressed by

$$G_c = \frac{a_7}{a_1} = \frac{-t_1 t_2 e^{-ikL}}{1 - r_1 r_2 e^{-2ikL}}, \tag{5.16}$$

and the phase is

$$P_c = \arg[G_c]. \tag{5.17}$$

We can plot G_c and P_c as functions of the laser frequency f as shown in Fig. 5.9. From the phase plot, we obtain the cavity pole frequency which is given by the value for which the phase has dropped by 45° from 180° to 135°. This also corresponds to a -3 dB gain reduction. Our simulation results confirm that the cavity pole frequency is one half of the cavity bandwidth (see Eq. (A.6)) and it can be determined by the cavity Finesse $\mathcal{F}$ and cavity length L as

$$f_{\text{pole}} = \frac{\text{FSR}}{2\mathcal{F}} = \frac{c/2L}{2\pi/2 \arcsin\left(\frac{1-r_1 r_2}{2\sqrt{r_1 r_2}}\right)}. \tag{5.18}$$

For instance, a 0.21 m cavity with finesse 2093 shall give a pole frequency of about 17.06 kHz. Therefore, using a cavity pole measurement, we are able to characterise the optical loss of a cavity.

Results

We performed a cavity transfer function measurement on the MC as shown in the input part in Fig. 5.5. We schematically illustrate it again in Fig. 5.10 to gain a better understanding of this measurement. A sinusoidal signal is applied to an EOM with sweep frequencies from 1 Hz to 1 MHz, which provides sidebands to the carrier field with a continuously changing frequency. Due to the fact that

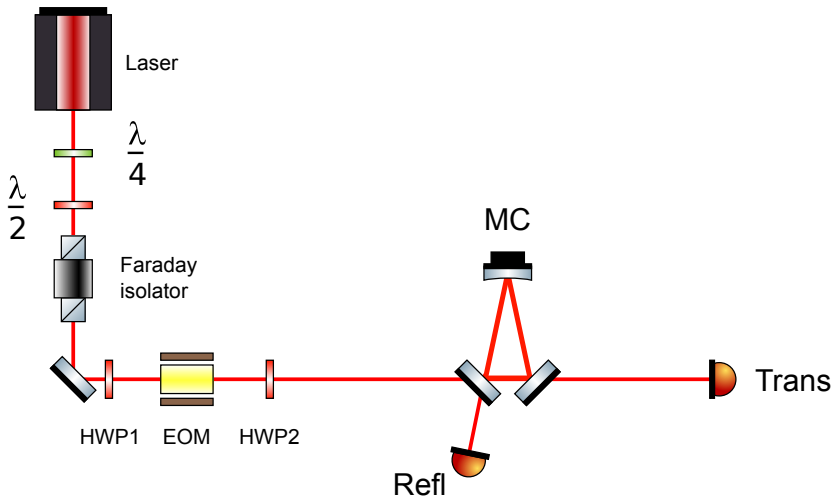

Figure 5.10.: A schematic showing the setup to measurement cavity transfer function via EOM, which creates phase modulated sidebands. Two half-wave plates are used to modify the phase modulation into amplitude modulation via polarisations.

an EOM only creates phase modulation, here two half wave plates (HWPs) are used before and after the EOM to rotate the polarisation angle, which introduces a polarisation modulation and in turn generates amplitude modulated sidebands to be detected by the transmitted photodiode.

Given a linearly polarised beam after the Faraday isolator, it then can be expressed by a Jones vector as

$$\mathbf{D}_0 = \begin{bmatrix} D_x \\ D_y \end{bmatrix} = e^{i\phi_0} \begin{bmatrix} \cos\theta \\ \sin\theta \end{bmatrix}. \tag{5.19}$$

An EOM applies a phase modulation to one unique linear polarisation and it is determined by the design and orientation of the EOM crystal. For simplicity, we assume only the D_x quadrature is phase-modulated and thus have

$$\mathbf{D}_0^{'} = e^{i\phi_0} \begin{bmatrix} \cos\theta e^{i\delta} \\ \sin\theta \end{bmatrix}, \tag{5.20}$$

where δ is a modulation input signal, i.e., $\cos(\Omega t)$. It is obvious that the power of this phase-modulated beam is a constant

$$I = D_x^2 + D_y^2, \tag{5.21}$$

which will not change over modulation frequency. This is the reason we use the polarisation modulation. Again we have a linearly polarised beam after the Faraday isolator. The first HWP rotates the polarisation angel by an angle of α_1

$$\mathbf{D}_1 = e^{i\phi_0} \begin{bmatrix} \cos 2\alpha_1 & \sin 2\alpha_1 \\ \sin 2\alpha_1 & -\cos 2\alpha_1 \end{bmatrix} \begin{bmatrix} \cos\theta \\ \sin\theta \end{bmatrix} = e^{i\phi_0} \begin{bmatrix} \cos(2\alpha_1 - \theta) \\ \sin(2\alpha_1 - \theta) \end{bmatrix}. \tag{5.22}$$

An EOM creates phase modulation to the D_x quadrature only and we have

$$\mathbf{D}_1^{'} = e^{i\phi_0} \begin{bmatrix} \cos(2\alpha_1 - \theta)e^{i\delta} \\ \sin(2\alpha_1 - \theta) \end{bmatrix} \tag{5.23}$$

immediately after the EOM. The phase modulated field enters the second HWP and ultimately turns into

$$\mathbf{D}_2 = \begin{bmatrix} \cos 2\alpha_2 & \sin 2\alpha_2 \\ \sin 2\alpha_2 & -\cos 2\alpha_2 \end{bmatrix} \mathbf{D}_1^{'} = e^{i\phi_0} \begin{bmatrix} \cos 2\alpha_2 \cos(2\alpha_1 - \theta)e^{i\delta} + \sin 2\alpha_2 \sin(2\alpha_1 - \theta) \\ \sin 2\alpha_2 \cos(2\alpha_1 - \theta)e^{i\delta} - \cos 2\alpha_2 \sin(2\alpha_1 - \theta) \end{bmatrix}. \tag{5.24}$$

If $2\alpha_1 - \theta = 2\alpha_2 = \pi/4$, we then obtain

$$\mathbf{D}_2 = e^{i\phi_0} \begin{bmatrix} \frac{1}{2}e^{i\delta} + \frac{1}{2} \\ \frac{1}{2}e^{i\delta} + \frac{1}{2} \end{bmatrix}, \tag{5.25}$$

which gives the output power

$$I = 1 + e^{i\delta}, \tag{5.26}$$

being a frequency-dependent value given δ is a frequency-dependent function.

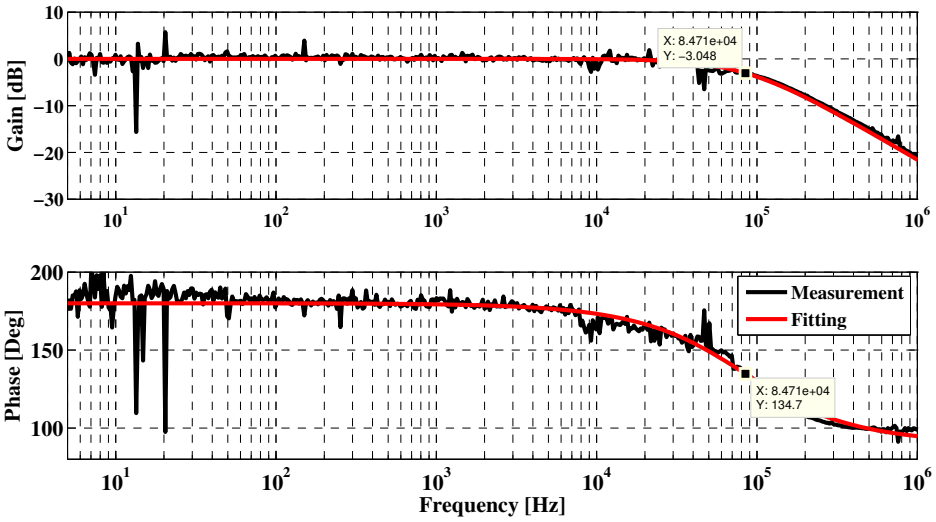

Figure 5.11.: Plots showing a cavity transfer function measured in the lab. The fitting results show the possibility to evaluate a cavity finesse, which is 4214 here, via the cavity pole frequency.

The transfer function is obtained by dividing the transmitted power by the reflection power (see Fig. 5.10). Using a network analyser (HP 8751A) to analyse the result, we obtained the cavity amplitude and phase TFs as shown in Fig. 5.11 (black). The fitted results (red) give the finesse estimation of the MC of 4214. This number is smaller than the finesse estimation from a ring-down measurement (6035). Our preliminary results show that the non-linear response of the PZT will result in a higher finesse number from the ring-down measurement, which means the actual finesse value will be closer to that from the cavity pole measurement. However, further investigation on the error is beyond the scope of this thesis, and will be developed in a follow-up study.

5.6. Summary

Realistic implementations of filter cavities in advanced GW detectors require minimal optical losses and a relatively short cavity length. It is generally believed that longer cavities are less susceptible to optical losses [55]. An optimal design will trade off the better quantum noise sensitivity against a longer filter cavity; the original proposals always favoured a longer filter cavity. However, this is only true given the cavity-round trip loss is independent of the cavity length (or has negligible influence). It is of great importance to examine experimentally this correlation.

We have designed a table-top experiment to estimate the optical losses of a cavity with a finesse of around 2000 for a variable cavity length (from 2 cm to 2 m). This experiment is still under construction. We have presented our first stage results, including (i) the experimental design of a length varying cavity, (ii) simulation results of cavity optical losses based on mirror maps of mirrors that will be used in the real experiment, and (iii) the demonstration of two practical optical loss estimation methods: ring-down measurement and cavity pole measurement.

5.7. Outlook

Based on the study presented in this chapter, the followup work will need to cover three parts: (1) finalising the setup construction, including (i) the laminar flow cabinet installation on the optical table, and (ii) the auto-alignment control implementation; (2) measuring the ring-down response and the cavity transfer function of the test cavity at different lengths using the methods provided in this thesis to extract the observed cavity finesse; (3) achieving the required results, for the cavity finesse change as a function of cavity length, including (i) non-linear

PZT calibration, and (ii) finesse error analysis.

Chapter 6.

Conclusion and Discussion

6.1. Summary

In the gravitational wave community, the reduction of the fundamental quantum noise is now one of the key challenges to improve advanced and future gravitational wave detectors. Currently, different schemes are considered for practical implementations.

I first explored the intra-cavity filtering schemes to reduce the low-frequency quantum noise. I substantiated that such a scheme in which the filter cavity is placed inside the signal recycling cavity could be a good alternative for a speed meter, with a small portion of the output signal representing a position response at low frequencies. Furthermore, I compared the intra-cavity filtering to an input filtering. A global optimisation result suggested that intra-filtering could provide a similar quantum noise reduction as the input-filtering based on the current Advanced LIGO infrastructure.

An alternative topology which is less sensitive to optical loss, a polarising Sagnac topology, has been analysed for low-frequency quantum noise reduction. I found

that the output could be dominated by its Sagnac response (speed meter) mixed with a fraction of a Michelson response (position meter) which is induced by the imperfection leakage from the polarising beam splitter. Due to their orthogonal polarisations, I could employ a polarising beam splitter to combine the Sagnac and Michelson response and use the Michelson response to provide a DC-readout local oscillator. I have presented a polarising Sagnac interferometer with reduced complexity and costs but with a comparable quantum noise sensitivity as a Michelson interferometer with filter cavities and the signal recycling mirror. By using realistic parameters based on the ET design, we show that such a topology could potentially be implemented for the low-frequency interferometer of the Einstein Telescope.

I have designed, set up and constructed a new experiment to estimate the cavity optical losses due to the cavity mirror scattering. I characterised the finesse of a rigid cavity using both the ring-down and cavity pole measurements. My preliminary results suggested the possibility to achieve the results we expected and followup experiments have been planned.

6.2. Conclusion and Discussion

Future gravitational wave detectors will be limited by quantum noise. The proposed schemes for reducing this noise pose technical challenges such as requirements for very low optical losses. My work contributes to the existing quantum noise reduction schemes by providing practical alternatives that are able to relieve originally stringent technical requirements, by being more robust to optical losses and lowering manufacturing requirements on optical components, while retaining a very good quantum noise performance. The generic quantum noise analysis method illustrated in this thesis may be applied to gravitational wave detectors

with diverse optical topologies and configurations.

The alternative optical filtering schemes I have presented in Chapter 3 assist in our understanding of the role of different optical filtering schemes for quantum noise reduction. We found that the intra-cavity filtering can reduce the quantum noise to a low level as the input filtering does. For Advanced LIGO, it will be a strong candidate to be implemented. Besides, its speed meter response remains to be investigated, representing an interesting experimental project in itself.

The research of a realistic polarising Sagnac topology presented in Chapter 4 makes an important contribution to future gravitational wave detectors, in particular the study of a practical readout scheme would add substantially to our understanding of the feasibility to use a speed meter. Since ET has been envisaged as an infrastructure that could host different implementations of GW detectors over a long time, I believe a polarising Sagnac interferometer is highly attractive alternative to the current baseline design.

In Chapter 5, I presented the setup and characterisation of an experiment to investigate optical cavity losses. In the future this experiment will also be used to characterise near-unstable cavity and to investigate the accuracy of using measured mirror surface maps for the estimation of optical losses. This work will support the commissioning of advanced detectors indirectly and will provide essential input for the design of future detectors relying on improved mirror surface figures.

My research has substantiated feasible alternative schemes for gravitational wave detectors, and it also raises several interesting questions in need of further investigation. It is shown that the intra-cavity filtering working as a speed meter gives a sensitivity curve mixing the position meter response at low frequencies and the speed meter response at the intermediate frequencies. This output is similar to

the response of the imperfect polarising Sagnac. Further studies are required to investigate the feasibility to use the low-frequency position response signal as a local oscillator for the homodyne detection.

Appendix A.

Fabry-Pérot Cavity

We detail the properties of a linear Fabry-P'erot cavity here. A Fabry-Pérot cavity consists of two mirrors, separated by a distance of L, and is schematically shown in Fig. A.1. Cavity mirrors are defined by mirror reflection coefficients $r_{1,2}$, transmission coefficients $t_{1,2}$ and loss coefficients $\epsilon_{1,2}$ or mirror reflectivity $R_{1,2}$, transmissivity $T_{1,2}$ and loss $\mathcal{E}_{1,2}$. They satisfy

$$R_{1,2} + T_{1,2} + \mathcal{E}_{1,2} = 1, \qquad R_{1,2} = r_{1,2}^2, \qquad T_{1,2} = t_{1,2}^2, \qquad \mathcal{E}_{1,2} = \epsilon_{1,2}^2, \quad \text{(A.1)}$$

The electric fields (a_j) at different ports follow relations

$$\begin{aligned} &a_2 = r_1 a_1 + i t_1 a_4, \qquad a_3 = i t_1 a_1 + r_1 a_4, \qquad a_4 = e^{-i\omega L/c} a_6, \\ &a_5 = e^{-i\omega L/c} a_3, \qquad a_6 = r_2 a_5, \qquad a_7 = i t_2 a_5. \end{aligned} \quad \text{(A.2)}$$

Assuming a_1 is the only input field, solving the above equations, we can express each field as a function of a_1 as

$$\begin{aligned} a_2 &= \frac{r1 - (1 - r_1^2 - t_1^2) r_2 e^{-2i\omega L/c}}{1 - r_1 r_2 e^{-2i\omega L/c}} a_1, & a_3 &= \frac{i t_1}{1 - r_1 r_2 e^{-2i\omega L/c}} a_1, \\ a_4 &= \frac{i t_1 r_2 e^{-i2\omega L/c}}{1 - r_1 r_2 e^{-2i\omega L/c}} a_1, & a_5 &= \frac{i t_1 e^{-i\omega L/c}}{1 - r_1 r_2 e^{-2i\omega L/c}} a_1, \\ a_6 &= \frac{i t_1 r_2 e^{-i\omega L/c}}{1 - r_1 r_2 e^{-2i\omega L/c}} a_1, & a_7 &= \frac{-t_1 t_2 e^{-i\omega L/c}}{1 - r_1 r_2 e^{-2i\omega L/c}} a_1. \end{aligned} \quad \text{(A.3)}$$

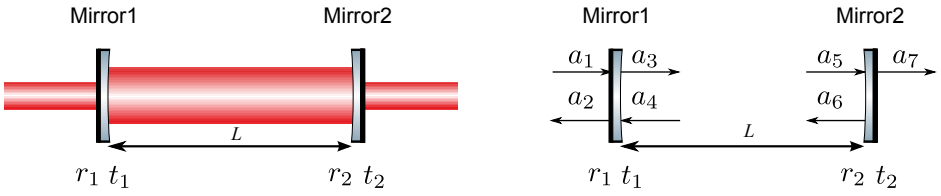

Figure A.1.: Schematics of a linear Fabry-Pérot cavity with a length L. Righthand plot illustrates incoming and outgoing light fields $a_j, j = 1, ..., 7$ at different ports. $r_{1,2}$ and $t_{1,2}$ are the reflectivity and transmissivity coefficients of Mirror1 and Mirror2 respectively.

Laser power circulating inside the cavity is therefore given by

$$I_c = a_3 \cdot a_3^* = \frac{T_1}{1 + R_1 R_2 - 2r_1 r_2 \cos(2\omega L/c)} |a_0|^2. \tag{A.4}$$

The power reaches its maximum value when cavity parameters satisfy $2\omega L/c = N \cdot 2\pi$, and the cavity is called a *resonant* cavity. When a cavity is *anti-resonant*, it has the minimum power with $2\omega L/c = N \cdot (2\pi + 1/2\pi)$. Assuming an input power of $|a_0|^2 = 1\,\mathrm{W}$, the circulating power I_c changing as a function of laser frequency is shown in Fig. A.2. The frequency difference between the two peaks (or valleys) is called the free spectral range (FSR), defined by

$$\mathrm{FSR} = \frac{c}{2L}. \tag{A.5}$$

Cavity *bandwidth* γ (also referred to as *linewidth*) is another important parameter of a cavity and is determined by the full width at half maximum value, which can be expressed as

$$\gamma = \frac{2\mathrm{FSR}}{\pi} \arcsin\left(\frac{1 - r_1 r_2}{2\sqrt{r_1 r_2}}\right). \tag{A.6}$$

Associated with this is the cavity *pole frequency* f_p, and it is defined as half of the linewidth $f_{\mathrm{pole}} = \gamma/2$.

Cavity *finesse* is defined by the ratio of the cavity FSR and bandwidth:

$$\mathcal{F} = \frac{\mathrm{FSR}}{\gamma} = \frac{\pi}{2\arcsin\left(\frac{1-r_1 r_2}{2\sqrt{r_1 r_2}}\right)} \approx \frac{\pi}{1 - r_1 r_2}. \tag{A.7}$$

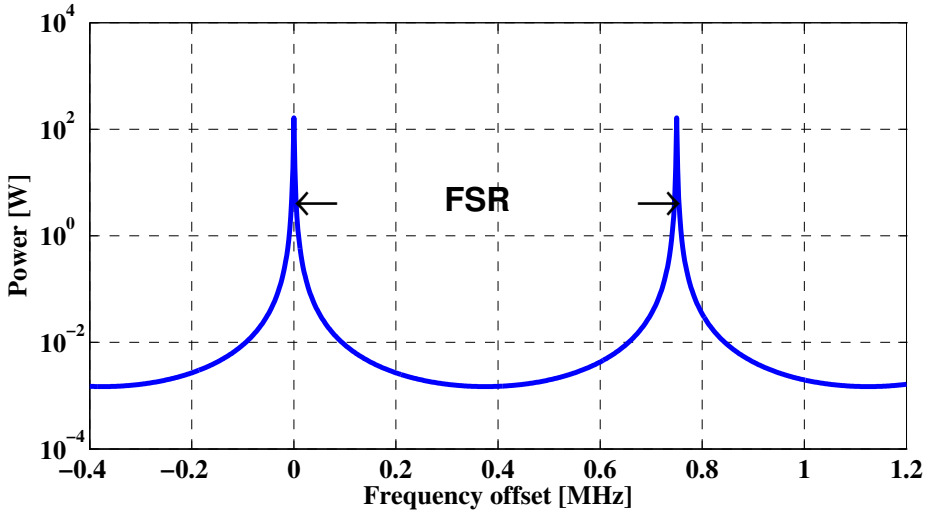

Figure A.2.: A plot showing the circulating power inside a linear Fabry-Pérot cavity. The cavity is on resonance when the power reaches its maximum value. The frequency difference between the two peak is called the free-spectral-range (FSR).

We notice that the power circulating inside a cavity will be built up at its resonance position and it is associated to the cavity finesse as

$$I_c^{\max} = I_0 \cdot \mathcal{F}/\pi, \tag{A.8}$$

with I_0 being the input power. This is the basic idea for using a power recycling cavity to lower the requirement for the input laser power. Cavities have been extensively investigated for GW detection: the arm cavities and a signal recycling cavity to increase signal storage time, a power recycling cavity to ease the input laser power requirement, as well as filter cavities which help to introduce a frequency-dependent rotation angle.

A cavity traps the light field inside the resonator, which effectively increases the light field travelling time and solves the issue of an impractically long arm installation for GW detectors. The storage time is given by

$$\tau_s \approx \frac{L}{c}\frac{\mathcal{F}}{\pi}, \tag{A.9}$$

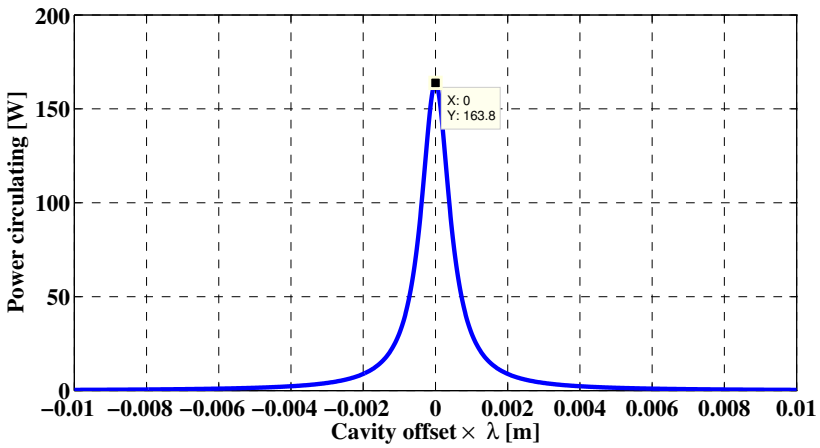

Figure A.3.: Plot showing circulating power inside a symmetric Fabry-Pérot cavity with finesse 500, assuming a monochromatic incident power of 1 W.

where $\mathcal{F}$ is by Eq. (A.7).

The fields in Eq (A.3) confirm that the cavity response, either in reflection or transmission, is determined by the mirror parameters r, t, and ϵ. They are also functions associated with the cavity length L and the input laser frequency ω. For example, we consider a symmetric cavity with finesse 500, where $r_1 = r_2 = 0.997$ and $\mathcal{E} = 75$ ppm. Figures A.4 and A.5 show the transmitted and reflected power when the cavity length and input laser frequency is changing. It is clearly shown in Fig. A.4(a) and Fig. A.4(b) that with a monochromatic input field, the power of the transmitted and reflected fields alter as a function of cavity length and at its resonance position the transmitted power is maximum while the reflection power is almost zero. Since the cavity offset change is typically in the order of 1 um (one wavelength), we can convert the cavity offset distance into a detuning phase, which means that a displacement of one wavelength λ corresponds to a 2π phase change. Meanwhile, the cavity response differs for different input laser frequencies as shown in Figs. A.5(a) and A.5(b). This frequency-dependent feature

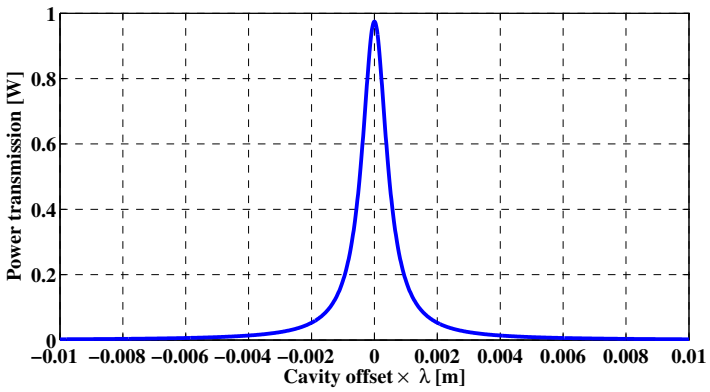

(a)

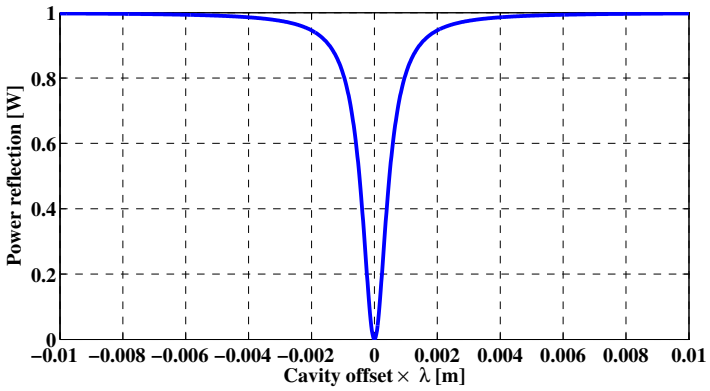

(b)

Figure A.4.: Plots showing the change in the transmitted and reflected power as a function of cavity length by a symmetric Fabry-Pérot Cavity. The Finesse is around 500 ($r_1 = r_2 = 0.997$) and each mirror has loss $\mathcal{E} = 75\,\text{ppm}$.

enables the use of Fabry-Pérot cavities as filter cavities and will be significant in Chapters 3 and 5.

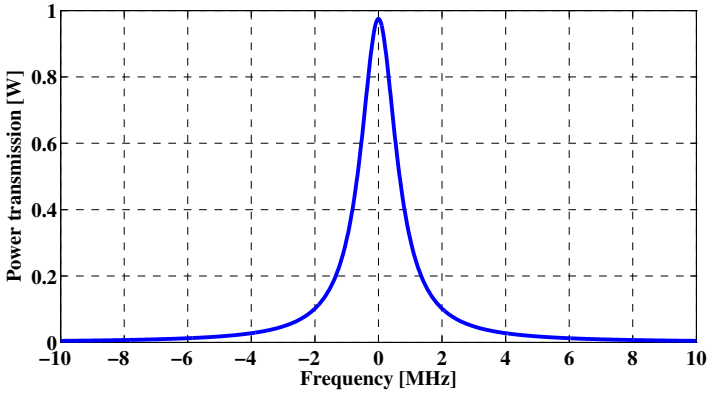

(a)

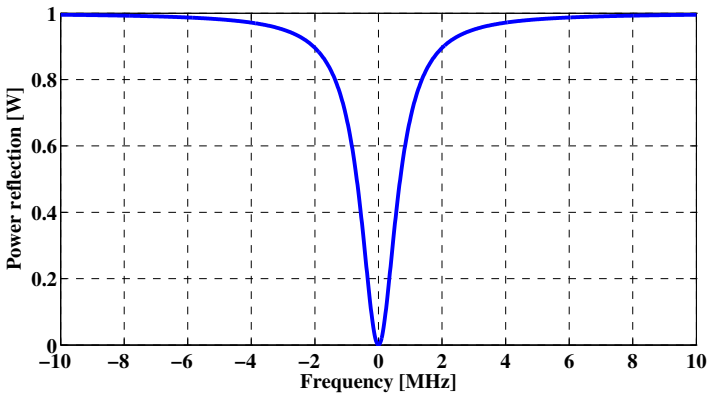

(b)

Figure A.5.: Plots showing the change in the transmitted and reflected power as a function of laser frequency by a symmetric Fabry-Pérot Cavity, with a Finesse around 500 ($r_1 = r_2 = 0.997$) and each mirror has loss $\mathcal{E} = 75\,\text{ppm}$.

Appendix B.

Input-output relation for the three-port junction in the intra-cavity filtering scheme

Here we show the details for the input-output relation of the three-port vortex (one input and one output for each port) formed by the ITM, the sloshing mirror, and the SRM in the intra-cavity filtering scheme. We define the characteristic frequencies of the intra-cavity filtering used in the Hamiltonian in Section 3.2.2.

In Fig. B.1, we show the reflectivity for each optic and its convention of sign. By using the junction condition on each optic, we obtain

$$\boldsymbol{v}^{\mathrm{ref}} = \mathbf{M}_t \, \boldsymbol{v}^{\mathrm{in}} \tag{B.1}$$

with $\boldsymbol{v}^{\mathrm{ref}} = [c_a^{\mathrm{ref}}, c_b^{\mathrm{ref}}, d^{\mathrm{ref}}]^{\mathrm{T}}$ and $\boldsymbol{v}^{\mathrm{in}} = [c_a^{\mathrm{in}}, c_b^{\mathrm{in}}, d^{\mathrm{in}}]^{\mathrm{T}}$ (the superscript T denotes the transpose) and $\mathbf{M}_t$ being the transfer matrix. The transfer matrix has the following property:

$$\mathbf{M}_t = \mathbf{M}_t^{\mathrm{T}}, \quad \mathbf{M}_t \, \mathbf{M}_t^{\dagger} = \mathbf{I}, \tag{B.2}$$

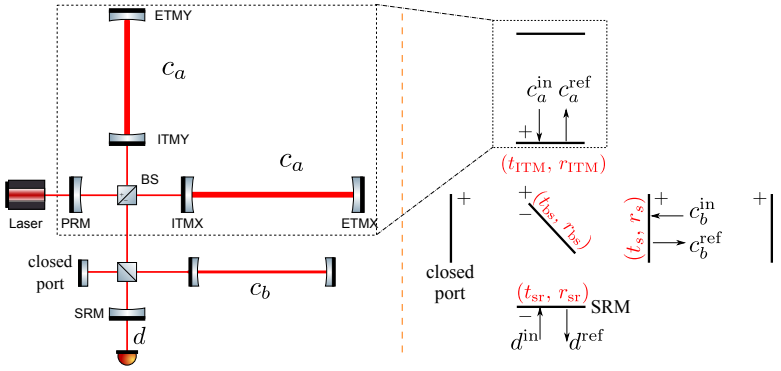

Figure B.1.: Figure illustrating the three-port vortex that we are interested in. We map the two arm cavities into a single cavity (denoted by the dashed box), following [65]. Here, r_i (complex) and t_i (real) are the amplitude reflectivity and transmissivity of the optics. The sign of convention for the reflectivity are indicated by $\pm$, where the amplitude reflectivity on the positive side is r and the minus side is $-r^*$ (complex conjugate).

which means that $\mathbf{M}_t$ is a *symmetric unitary* matrix. This gives the Stokes relation for such three-port linear optics. More specifically, the elements of $\mathbf{M}_t$ in terms of the reflectivity and transmissivity of each optic are given by

$$\begin{aligned}
\mathbf{M}_{11} =& \mathcal{D}^{-1}[r_{\rm ITM} - r_s^* r_{\rm bs}^2 - r_{\rm ITM} r_{\rm sr} r_{\rm bs}^{*2} \\
&+ (r_{\rm sr} + r_{\rm ITM} r_s^*) t_{\rm bs}^2 + r_s^* r_{\rm sr}] \,, && \text{(B.3)} \\
\mathbf{M}_{12} =& \mathcal{D}^{-1}(r_{\rm bs} - r_{\rm sr} r_{\rm bs}^*) t_{\rm ITM}\, t_s \,, && \text{(B.4)} \\
\mathbf{M}_{13} =& \mathcal{D}^{-1}(1 + r_s^*) t_{\rm ITM} t_{\rm sr} t_{\rm bs} \,, && \text{(B.5)} \\
\mathbf{M}_{22} =& \mathcal{D}^{-1}[r_s - r_{\rm ITM}^* r_{\rm bs}^2 - r_s r_{\rm sr} r_{\rm bs}^{*2} \\
&+ (1 + r_{\rm ITM}^* r_s r_{\rm sr}) t_{\rm bs}^2 + r_{\rm ITM}^* r_{\rm sr}] \,, && \text{(B.6)} \\
\mathbf{M}_{23} =& \mathcal{D}^{-1}(-r_{\rm bs}^* - r_{\rm ITM}^* r_{\rm bs}) t_s t_{\rm sr} t_{\rm bs} \,, && \text{(B.7)} \\
\mathbf{M}_{33} =& \mathcal{D}^{-1}[-r_{\rm sr}^* + r_{\rm bs}^{*2} + r_{\rm ITM}^* r_s^* r_{\rm sr}^* r_{\rm bs}^2 \\
&- (r_{\rm ITM}^* + r_s^* r_{\rm sr}^*) t_{\rm bs}^2 - r_{\rm ITM}^* r_s^*] \,, && \text{(B.8)}
\end{aligned}$$

where the denominator $\mathcal{D}$ reads

$$\mathcal{D} = 1 - r^*_{\rm ITM} r^*_s r^2_{\rm bs} - r_{\rm sr} r^{*2}_{\rm bs} + (r^*_{\rm ITM} r_{\rm sr} + r^*_s) t^2_{\rm bs} + r^*_{\rm ITM} r^*_s r_{\rm sr} \,.$$

From the above input-output relation, we can define the effective coupling among three optical modes c_a, c_b and the external continuum d. Specifically, we introduce the sloshing frequency between c_a and c_b:

$$\omega_s \equiv \frac{c|\mathbf{M}_{12}|}{2\sqrt{L_{\rm arm} L_s}}, \tag{B.9}$$

and two decay rates for each mode:

$$\gamma_a \equiv \frac{c|\mathbf{M}_{13}|^2}{4L_{\rm arm}} \,, \qquad \gamma_b \equiv \frac{c|\mathbf{M}_{23}|^2}{4L_s} \,. \tag{B.10}$$

In addition, the resonant frequencies for each modes can also be defined, and we have

$$\omega_a \equiv \frac{c \, \arg(\mathbf{M}_{11})}{2L_{\rm arm}} \,, \qquad \omega_b \equiv \frac{c \, \arg(\mathbf{M}_{22})}{2L_s}, \tag{B.11}$$

with 'arg' being the phase angle.

Appendix C.

Complete output equations

Here we present the complete equations of the two polarised output fields from a Sagnac interferometer with an imperfect PBS (see Eqs. (4.13) and (4.14)).

$$\begin{aligned}
\begin{bmatrix} q_{p1}(\Omega) \\ q_{p2}(\Omega) \end{bmatrix} &= \left[-\sqrt{\eta_p}\mathbf{I} + (1-\eta_p)\sqrt{1-\eta_s}\mathbf{M}_{\mathrm{CLG}}\mathbf{M}_{\mathrm{sag}}\right] \begin{bmatrix} g_{p1}(\Omega) \\ g_{p2}(\Omega) \end{bmatrix} \\
&\quad + \sqrt{1-\eta_p}\sqrt{\eta_s}\mathbf{M}_{\mathrm{CLG}}\mathbf{M}_{\mathrm{arm}} \begin{bmatrix} g_{s1}(\Omega) \\ g_{s2}(\Omega) \end{bmatrix} \\
&\quad + \sqrt{1-\eta_p}\sqrt{1-\eta_s}\mathbf{M}_{\mathrm{CLG}}\mathbf{H}_{\mathrm{sag}}h(\Omega) \\
&\quad + \sqrt{1-\eta_p}\sqrt{1-\eta_s}\mathbf{M}_{\mathrm{CLG}}\mathbf{N}_{\mathrm{sag}} \begin{bmatrix} n_1(\Omega) \\ n_2(\Omega) \end{bmatrix}, \qquad \text{(C.1)}
\end{aligned}$$

$$\begin{aligned}
\begin{bmatrix} q_{s1}(\Omega) \\ q_{s2}(\Omega) \end{bmatrix} &= -\left[-\sqrt{1-\eta_s}\mathbf{I} + \eta_s\sqrt{\eta_p}\mathbf{M}_{\mathrm{CLG}}\mathbf{M}_{\mathrm{sag}}\right] \begin{bmatrix} g_{s1}(\Omega) \\ g_{s2}(\Omega) \end{bmatrix} \\
&\quad + \sqrt{\eta_s}\sqrt{1-\eta_p}\mathbf{M}_{\mathrm{CLG}}\mathbf{M}_{\mathrm{arm}} \begin{bmatrix} g_{p1}(\Omega) \\ g_{p2}(\Omega) \end{bmatrix} \\
&\quad + \sqrt{\eta_s}\mathbf{M}_{\mathrm{CLG}}\mathbf{H}_{\mathrm{arm}}h(\Omega) \\
&\quad + \sqrt{\eta_s}\mathbf{M}_{\mathrm{CLG}}\mathbf{N}_{\mathrm{arm}} \begin{bmatrix} n_1(\Omega) \\ n_2(\Omega) \end{bmatrix}. \qquad \text{(C.2)}
\end{aligned}$$

Bibliography

[1] M Wang, H Miao, A Freise, and Y Chen. Sensitivity of intra-cavity filtering scheme for detecting gravitational waves. *Phys. Rev. D*, 2013 submitted.

[2] M Wang, C Bond, D Brown, F Brückner, L Carbone, R Palmer, and A Freise. Realistic polarizing sagnac topology with dc readout for the einstein telescope. *Phys. Rev. D*, 87:096008, May 2013.

[3] A.Einstein. On gravitational waves. *Sitzungsber. Preuss. Akad. Wiss.Berlin*, 1:154, 1918.

[4] P Aufmuth and K Danzmann. Gravitational wave detectors. *New Journal of Physics*, 7:202, 2005.

[5] Laser interferometer gravitational-wave observatory. http://www.ligo.org.

[6] D Sigg and the LIGO Scientific Collaboration. Status of the ligo detectors. *Classical and Quantum Gravity*, 25(11):114041, 2008.

[7] G. M Harry and the LIGO Scientific Collaboration. Advanced ligo: the next generation of gravitational wave detectors. *Classical and Quantum Gravity*, 27(8):084006, 2010.

[8] R Lawrence, M Zucker, P Fritschel, P Marfuta, and D Shoemaker. Adaptive

thermal compensation of test masses in advanced LIGO. *Classical and Quantum Gravity*, 19:1803–1812, Apr. 2002.

[9] J Degallaix, C Zhao, L Ju, and D Blair. Thermal lensing compensation for AIGO high optical power test facility. *Classical and Quantum Gravity*, 21:903–+, Mar. 2004.

[10] L Carbone, S. M Aston, R. M Cutler, A Freise, J Greenhalgh, et al. Sensors and actuators for the advanced ligo mirror suspensions. *Class. Quantum Grav.*, 29:115005, 2012.

[11] A. V Cumming, A. S Bell, L Barsotti, M. A Barton, G Cagnoli, et al. Design and development of the advanced LIGO monolithic fused silica suspension. *Classical and Quantum Gravity*, 29(3):035003, Feb. 2012.

[12] B Schutz. *Gravity from the Ground Up: An Introductory Guide to Gravity and General Relativity*. Cambridge University Press, 2003.

[13] B Sathyaprakash and B. F Schutz. Physics, astrophysics and cosmology with gravitational waves. *Living Reviews in Relativity*, 12(2), 2009.

[14] J. D Creighton and W. G Anderson. *Gravitational-Wave Physics and Astronomy*. Wiley Series in Coomology, 2011.

[15] L Blanchet. Gravitational radiation from post-newtonian sources and inspiralling compact binaries. *Living Reviews in Relativity*, 9(4), 2006.

[16] K. S Thorne. Gravitational Radiation – A New Window Onto the Universe. *ArXiv General Relativity and Quantum Cosmology e-prints*, Apr. 1997.

[17] The LIGO Scientific Collaboration, the Virgo Collaboration, J Abadie, B. P Abbott, R Abbott, et al. Sensitivity to Gravitational Waves from Compact Binary Coalescences Achieved during LIGO's Fifth and Virgo's First Science Run. *ArXiv e-prints*, Mar. 2010.

[18] J Lobo. *The Detection of Gravitational Waves*, volume 617 of *Lecture Notes in Physics*. Springer Berlin Heidelberg, 2003.

[19] R Weiss. Progress report of delay lines in a michelson interferometer for the detection of gravitational radiation. Technical report, MIT, Research Laboratory of Electronics, 1972.

[20] W Winkler. Gravitational wave detectors. In D Blair, editor, *The detection of gravitational waves*, pages 269–305. Cambridge University Press, 1991.

[21] R Drever and et al. In P Meystre and M Scully, editors, *Quantum Optics, Experimental Gravitation and Measurement Theory*, pages 503–514. Plenum Press, New York, 1983.

[22] P Saulson. Thermal noise in mechanical experiments. *Phys. Rev. D*, 42:2437–2445, Oct. 1990.

[23] G Heinzel, K. A Strain, J Mizuno, K. D Skeldon, B Willke, et al. Experimental demonstration of a suspended dual recycling interferometer for gravitational wave detection. *Phys. Rev. Lett.*, 81(25):5493–5496, Dec 1998.

[24] B. J Meers. Recycling in laser-interferometric gravitational-wave detectors. *Phys. Rev. D*, 38:2317–2326, Oct. 1988.

[25] A Freise, G Heinzel, K. A Strain, J Mizuno, K. D Skeldon, et al. Demonstration of detuned dual recycling at the Garching 30 m laser interferometer. *Physics Letters A*, 277:135–142, Nov. 2000.

[26] A Freise. Dual recycling for geo600. *arXiv:gr-qc/0306053*, 2003.

[27] Gravitational wave interferometer noise calculator. http://ilog.ligo-wa.caltech.edu:7285/advligo/GWINC.

[28] M Beccaria. Relevance of newtonian seismic noise for the virgo interferometer sensitivity. *Classical and Quantum Gravity*, 15(11):3339–3362, 1998.

[29] S. A Hughes and K. S Thorne. Seismic gravity-gradient noise in interferometric gravitational-wave detectors. *Phys. Rev. D*, 58(12):122002, Nov 1998.

[30] S Braccini, C Bradaschia, R. D Fabbro, A. D Virgilio, I Ferrante, et al. Seismic vibrations mechanical filters for the gravitational waves detector virgo. *Review of Scientific Instruments*, 67(8):2899–2902, 1996.

[31] P Saulson. *Fundamentals of Interferometric Gravitational Wave Detectors*. World Scientific, 1994.

[32] M Abernathy, F Acernese, P Ajith, B Allen, P Amaro-Seoane, et al. Einstein gravitational wave telescope conceptual design study. page 451, 2011.

[33] M. G Beker, J. F. J van den Brand, E Hennes, and D. S Rabeling. Newtonian noise and ambient ground motion for gravitational wave detectors. *Journal of Physics: Conference Series*, 363(1):012004, 2012.

[34] J. C Driggers, J Harms, and R. X Adhikari. Subtraction of newtonian noise using optimized sensor arrays. *Phys. Rev. D*, 86:102001, Nov 2012.

[35] P. W K. Pepper, R. Adhikari. Newtonian noise simulation and suppression for gravitational-wave interferometers. Technical report, LIGO, 2007.

[36] J.-Y Vinet. On special optical modes and thermal issues in advanced gravitational wave interferometric detectors. *Living Reviews in Relativity*, 12(5), 2009.

[37] S Rowan, J Hough, and D Crooks. Thermal noise and material issues for gravitational wave detectors. *Physics Letters A*, 347(1-3):25 – 32, 2005.

Einstein Special Issue - Special Issue in celebration of this year's World of Physics and the centenary of Einstein's annus mirabilis.

[38] H. B Callen and T. A Welton. Irreversibility and Generalized Noise. *Physical Review*, 83:34–40, July 1951.

[39] G. M Harry, A. M Gretarsson, P. R Saulson, S. E Kittelberger, S. D Penn, et al. Thermal noise in interferometric gravitational wave detectors due to dielectric optical coatings. *Classical and Quantum Gravity*, 19:897–917, Mar. 2002.

[40] D. R. M Crooks, P Sneddon, G Cagnoli, J Hough, S Rowan, et al. Excess mechanical loss associated with dielectric mirror coatings on test masses in interferometric gravitational wave detectors. *Classical and Quantum Gravity*, 19(5):883, 2002.

[41] S. D Penn, P. H Sneddon, H Armandula, J. C Betzwieser, G Cagnoli, et al. Mechanical loss in tantala/silica dielectric mirror coatings. *Classical and Quantum Gravity*, 20(13):2917, 2003.

[42] D. R. M Crooks, G Cagnoli, M. M Fejer, A Gretarsson, G Harry, et al. Experimental measurements of coating mechanical loss factors. *Classical and Quantum Gravity*, 21(5):S1059, 2004.

[43] J Franc, N Morgado, R Flaminio, R Nawrodt, I Martin, et al. Mirror thermal noise in laser interferometer gravitational wave detectors operating at room and cryogenic temperature. *ArXiv e-prints*, Dec. 2009.

[44] K Somiya. Detector configuration of kagra-the japanese cryogenic gravitational-wave detector. *Classical and Quantum Gravity*, 29(12):124007, 2012.

[45] I Martin, H Armandula, C Comtet, M. M Fejer, A Gretarsson, et al. Mea-

surements of a low-temperature mechanical dissipation peak in a single layer of ta2o5 doped with tio2. *Classical and Quantum Gravity*, 25(5):055005 (8pp), 2008.

[46] B Mours, E Tournefier, and J.-Y Vinet. Thermal noise reduction in interferometric gravitational wave antennas: using high order TEM modes. *Classical and Quantum Gravity*, 23:5777–5784, Oct. 2006.

[47] J.-Y Vinet. Reducing thermal effects in mirrors of advanced gravitational wave interferometric detectors. *Classical and Quantum Gravity*, 24(15):3897–3910, 2007.

[48] E D'Ambrosio. Nonspherical mirrors to reduce thermoelastic noise in advanced gravitational wave interferometers. *Physical Review D*, 67(10):102004–+, May 2003.

[49] M Bondarescu, O Kogan, and Y Chen. Optimal light beams and mirror shapes for future LIGO interferometers. *Phys. Rev. D*, 78(8):082002–+, Oct. 2008.

[50] C Bond, P Fulda, L Carbone, K Kokeyama, and A Freise. The effect of mirror surface distortions on higher order laguerre-gauss modes. *Journal of Physics: Conference Series*, 363:012005, 2012.

[51] V. B Braginskiĭ. Classical and Quantum Restrictions on the Detection of Weak Disturbances of a Macroscopic Oscillator. *Soviet Journal of Experimental and Theoretical Physics*, 26:831, Apr. 1968.

[52] V Braginsky and F Khalilli. *Quantum Measurements*. Cambridge University Press, 1992.

[53] A Buonanno and Y Chen. Signal recycled laser-interferometer gravitational-

wave detectors as optical springs. *Physical Review D*, 65(4):042001–+, Feb. 2002.

[54] H. J Kimble, Y Levin, A. B Matsko, K. S Thorne, and S. P Vyatchanin. Conversion of conventional gravitational-wave interferometers into quantum nondemolition interferometers by modifying their input and/or output optics. *Physical Review D*, 65(2):022002–+, Jan. 2002.

[55] F. Y Khalili. Optimal configurations of filter cavity in future gravitational-wave detectors. *Phys. Rev. D*, 81(12):122002–+, June 2010.

[56] F. Y Khalili and Y Levin. Speed meter as a quantum nondemolition measuring device for force. *Physical Review D*, 54:4735–4737, Oct. 1996.

[57] P Purdue and Y Chen. Practical speed meter designs for quantum nondemolition gravitational-wave interferometers. *Physical Review D*, 66(12):122004–+, Dec. 2002.

[58] Y Chen. Sagnac interferometer as a speed-meter-type, quantum-nondemolition gravitational-wave detector. *Phys. Rev. D*, 67(12):122004–+, June 2003.

[59] C. M Caves and B. L Schumaker. New formalism for two-photon quantum optics. I - Quadrature phases and squeezed states. II - Mathematical foundation and compact notation. *Physical Review A*, 31:3068–3111, May 1985.

[60] A Messiah. *Quantum mechanics*, volume one of *Quantum Mechanics*. North-Holland Pub. Co., 1962.

[61] M Scully and S Zubairy. *Quantum Optics*. Cambridge University Press, 1997.

[62] A Buonanno and Y Chen. Quantum noise in second generation, signal-

recycled laser interferometric gravitational-wave detectors. *Phys. Rev. D*, 64(4):042006–+, Aug. 2001.

[63] H Miao. *Exploring Macroscopic Quantum Mechanics in Optomechanical Devices*. PhD thesis, The University of Western Australia, 2010.

[64] P Purdue. Analysis of a quantum nondemolition speed-meter interferometer. *Physical Review D*, 66(2):022001–+, June 2002.

[65] A Buonanno and Y Chen. Scaling law in signal recycled laser-interferometer gravitational-wave detectors. *Physical Review D*, 67(6):062002–+, Mar. 2003.

[66] M Xiao, L.-A Wu, and H. J Kimble. Precision measurement beyond the shot-noise limit. *Phys. Rev. Lett.*, 59:278–281, Jul 1987.

[67] P Grangier, R. E Slusher, B Yurke, and A Laporta. Squeezed-light-enhanced polarization interferometer. *Physical Review Letters*, 59:2153–2156, Nov. 1987.

[68] H.-A Bachor and T. C Ralph. *A guide to experiments in quantum optics*. Wiley-VCH Weinheim ; Chichester, 2nd, rev. and enlarged ed. edition, 2004.

[69] T. R Corbitt. *Quantum Noise and Radiation Pressure Effects in High Power Optical Interferometers*. PhD thesis, MASSACHUSETTS INSTITUTE OF TECHNOLOGY, 2008.

[70] J Mizuno, K Strain, P Nelson, J Chen, R Schilling, et al. Resonant sideband extraction: a new configuration for interferometric gravitational wave detectors. *Physics Letters A*, 175(5):273 – 276, 1993.

[71] H Miao, H Yang, R. X Adhikari, and Y Chen. Quantum limits of interferometer topologies for gravitational radiation detection. *arXiv: 1305.3957*, 2013.

[72] LIGO Scientific Collaboration, Virgo Collaboration, J Aasi, J Abadie, B. P Abbott, et al. Prospects for localization of gravitational wave transients by the advanced ligo and advanced virgo observatories. page 18, Apr. 2013.

[73] B Sathyaprakash, M Abernathy, F Acernese, P Ajith, B Allen, et al. Scientific objectives of einstein telescope. *Classical and Quantum Gravity*, 29(12):124013, 2012.

[74] T Accadia, F Acernese, F Antonucci, P Astone, and et al. Status of the virgo project. *Classical and Quantum Gravity*, 28(11):114002, 2011.

[75] D Shoemaker. Future limits to sensitivity. presentation given at the Aspen Workshop, 2001.

[76] S Hild, S Chelkowski, A Freise, J Franc, N Morgado, R Flaminio, and R DeSalvo. A xylophone configuration for a third-generation gravitational wave detector. *Classical and Quantum Gravity*, 27:015003 (8pp), 2010.

[77] G Sagnac. The demonstration of the luminiferous aether by an interferometer in uniform rotation. *Comptes Rendus*, 157:708 – 710, 1913.

[78] K.-X Sun, M. M Fejer, E Gustafson, and R. L Byer. Sagnac interferometer for gravitational-wave detection. *Phys. Rev. Lett.*, 76(17):3053–3056, Apr 1996.

[79] S. L Danilishin. Sensitivity limitations in optical speed meter topology of gravitational-wave antennas. *Phys. Rev. D*, 69:102003, May 2004.

[80] Y Chen, S Danilishin, F Khalili, and H Müller-Ebhardt. Qnd measurements for future gravitational-wave detectors. *General Relativity and Gravitation*, 43:671–694, 2011.

[81] S. L Danilishin and F. Y Khalili. Quantum measurement theory in gravitational-wave detectors. *Living Reviews in Relativity*, 15(5), 2012.

[82] T Eberle, S Steinlechner, J Bauchrowitz, V Händchen, H Vahlbruch, et al. Quantum enhancement of the zero-area sagnac interferometer topology for gravitational wave detection. *Phys. Rev. Lett.*, 104(25):251102, Jun 2010.

[83] Thorlabs webpage. http://www.thorlabs.com/newgrouppage9.cfm?objectgroup_id=6004.

[84] Wave plate from cvi optics. https://www.cvimellesgriot.com/Products/Waveplate.aspx.

[85] Advanced ligo reference design. LIGO Technical report M060056, 2007.

[86] S Hild, H Grote, J Degallaix, S Chelkowski, K Danzmann, et al. Dc-readout of a signal-recycled gravitational wave detector. *Classical and Quantum Gravity*, 26(5):055012 (10pp), 2009.

[87] R Abbott, R Adhikari, S Ballmer, L Barsotti, M Evans, et al. Advanced ligo length sensing and control final design. *Advanced LIGO note*, (T1000298), 2010.

[88] B Abbott, R Adhikari, D Busby, J Heefner, K Kawabe, et al. Proposal for a homodyne (dc) detection experiment at the ligo caltech 40-meter laboratory. *Advanced LIGO note*, (LIGO-T050086-00-R), 2005.

[89] M Evans, L Barsotti, J Harms, P Kwee, and H Miao. Realistic Filter Cavities for Advanced Gravitational Wave Detectors. *ArXiv e-prints*, May 2013.

[90] A Krywonos, J. E Harvey, and N Choi. Linear systems formulation of scattering theory for rough surfaces with arbitrary incident and scattering angles. *J. Opt. Soc. Am. A*, 28(6):1121–1138, Jun 2011.

[91] C Bond, P Fulda, L Carbone, K Kokeyama, and A Freise. Higher order

laguerre-gauss mode degeneracy in realistic, high finesse cavities. *Phys. Rev. D*, 84:102002, Nov 2011.

[92] D Brown. Modelling mirror surface distortion effects in low-loss, near-unstable fabry-perot cavities. Technical Report G01300687, 2013.

[93] A Freise and K Strain. Interferometer Techniques for Gravitational-Wave Detection. *Living Reviews in Relativity*, 13:1–+, Feb. 2010.

[94] E Morrison, D. I Robertson, H Ward, and B. J Meers. Automatic alignment of optical interferometers. *Appl. Opt.*, 33:5041–5049, Aug. 1994.

[95] Coastline webpage. http://www.coastlineoptics.com.

[96] Cvi webpage. https://www.cvimellesgriot.com.

[97] A Freise. Finesse webpage. http://www.gwoptics.org/finesse.

[98] A Freise, G Heinzel, H Lück, R Schilling, B Willke, and K Danzmann. Frequency-domain interferometer simulation with higher-order spatial modes. *Classical and Quantum Gravity*, 21(5):S1067–S1074, 2004.

[99] N Uehara. Ring mode cleaner for the initial ligo 10 watt laser - internal report. See also UeharaSPIE, 1997.

[100] R. W. P Drever, J. L Hall, F. V Kowalski, J Hough, G. M Ford, A. J Munley, and H Ward. Laser phase and frequency stabilization using an optical resonator. *Applied Physics B: Lasers and Optics*, 31:97–105, June 1983.

[101] E Morrison, D. I Robertson, H Ward, and B. J Meers. Experimental demonstration of an automatic alignment system for optical interferometers. *Appl. Opt.*, 33:5037–5040, Aug. 1994.

[102] Physik instrumente webpage. http://www.physikinstrumente.com/en/index.php.

[103] K An, C Yang, R. R Dasari, and M. S Feld. Cavity ring-down technique and its application to the measurement of ultraslow velocities. *Opt. Lett.*, 20(9):1068–1070, May 1995.

[104] J Poirson, F Bretenaker, M Vallet, and A. L Floch. Analytical and experimental study of ringing effects in a fabry–perot cavity. application to the measurement of high finesses. *J. Opt. Soc. Am. B*, 14(11):2811–2817, Nov 1997.

[105] P Fulda. *Precision Interferometry in a New Shape: Higher-order Laguerre-Gauss Modes for Gravitational Wave Detection*. PhD thesis, University of Birmingham, 2012.